M.Sc. Thesis
Master of Science

A comparison of dynamic stall models and their effect on instabilities

Mark Faber

Aarhus 2018

DTU Wind Energy
Department of Wind Energy
Technical University of Denmark
DTU Risø Campus
Frederiksborgvej 399
4000 Roskilde, Denmark
Phone +45 4677 5085
info@vindenergi.dtu.dk
www.vindenergi.dtu.dk

Wind Energy Research Group
Faculty of Aerospace Engineering
Delft University of Technology
Kluyverweg 1
2629HS Delft, The Netherlands
Phone +31 1527 85170
windenergy-ae@tudelft.nl
www.windenergy.lr.tudelft.nl

Tools & Technologies Department
Vestas Technology R&D
Vestas Wind Systems A/S
Hedeager 42
8200 Aarhus N, Denmark
Phone +45 97 30 00 00
vestas@vestas.com
www.vestas.com

Summary

Aeroelastic codes are fundamental for the design of wind turbines and the prediction of instabilities. Such codes rely on engineering models which limit their accuracy. With wind turbine blades becoming more slender to lower the costs, it is important to reduce these uncertainties to maintain a safe and stable turbine design. The dynamic stall model is one of these engineering models which simplifies the physics involved and so an improvement in accuracy might be possible. Various dynamic stall models have been published over the last 50 years. However, dynamic stall has proven to be a complex phenomenon to model accurately over a wide range of conditions and is an ongoing topic of research.

Here four semi-empirical dynamic stall models, the Øye, Risø, Snel and ONERA models, are compared first in 2D against wind tunnel data to understand their accuracy and limitations. The experimental data for this comparison uses the NACA0015, NACA0030 and NACA4415 airfoils over a variety of cases relevant to wind turbines. Hereafter the models are compared within an aeroelastic code as a part of complete horizontal axis wind turbine simulations for an extreme load case (IEC design load case 1.4), standstill instabilities (IEC design load case 6.2) and the flutter speed to understand the effect of the different dynamic stall models. For the standstill cases the aerodynamic damping provided by each model is compared by reducing the structural damping of the blades to find the point where the blades become unstable. Next the Øye and Risø models are tuned to the wind tunnel data.

The results from the 2D comparison are inconclusive with each model showing different strengths and weaknesses. In general the attached flow physics in the Risø and ONERA models improves the fit for the 15% thick airfoils. The ONERA model captures the lift peak the best, although it usually has the largest least squares error to the data due to the drop in lift after this peak being too early and too sharp. Once in the aeroelastic code the ONERA model started to show unphysical behaviour by reducing the deflection in the extreme load case and adding negative damping to the standstill cases. Snel's model, on the other hand, adds so much damping that the blades remains stable even when the blades have only a small amount of structural damping, which is likely not physical. The Øye and Risø models show similar damping levels and reduce the required structural damping to prevent the standstill instabilities by at least a factor two with respect to no dynamic stall model being used. For the classical flutter analysis the Risø model shows an increase in flutter speed as expected from the implementation of Theodorsen's theory, while the ONERA model decreases the flutter limit.

Overall the Risø model is seen as the best for in an aeroelastic code due to showing better behaviour in the full turbine cases than the ONERA and Snel models. Furthermore, it is superior to the Øye model due to correctly modeling the attached flow physics and improving the drag and moment coefficients.

Preface

This thesis was prepared for obtaining the degree of Master of Science in Engineering Wind Energy at Technical University of Denmark and in Aerospace Engineering at Delft University of Technology.

Supervisors

Carlos Simão Ferreira	-	Delft University of Technology
Mac Gaunaa	-	Technical University of Denmark
Stefan Wolff	-	Vestas Wind Systems A/S

Master of Science Thesis
European Wind Energy Master
Aarhus, July 31, 2018

Mark John Faber (4294157/s163173)

Acknowledgements

This thesis wouldn't have be possible without the help and support of others. First I would like to thank my daily supervisor at Vestas, Stefan Wolff, for his humor, experience and endless patience. My university supervisors Mac Gaunaa and Carlos Simão Ferreira were also instrumental to the successful completion of my thesis and their detailed knowledge of dynamic stall, in-depth answers to my questions and critical thinking during the process have greatly improved the final product of my work.
Additionally I would like to thank Pieter Segers and Mario Luigi Miglionico for helping set the collaboration with Vestas up and keeping it on the rails even through all the bumps. Furthermore, James Alexander Nichols deserves recognition for his help in guiding the scope for the instability cases.
Finally, of course I can not forget my family and friends for their support and help throughout the entirety of this thesis.

Contents

CHAPTER 1

Introduction

1.1 Motivation for the research

Dynamic stall is a research topic that has been researched since the 1930's (e.g. Kramer [1]). Up to the 90's the research was mostly focused on helicopter blades [2] with most notably the Beddoes-Leishmann model [3] and the ONERA model [4] being developed in the 80's. More recently, the interest in wind turbines has grown and with it research into dynamic stall in wind turbines. The result is several basic and computationally fast dynamic stall models such as those by Snel [5] or Øye [6] and some tailored specifically for wind turbines, such as the Risø model [7] and that of Larsen et al. [8].
All modern Horizontal Axis Wind Turbines (HAWT) aeroelastic codes use a dynamic stall model to model at least the dynamic lift coefficient. This is necessary as the unsteady behaviour is often large enough that the steady airfoil polar no longer represents the aerodynamic forces accurately, which is due to these forces now having a dependency on the time history. Physically there are a variety of phenomena that can cause this such as the effect of circulation in the wake, the acceleration of the flow, a leading edge vortex being created and shed, a time delay in boundary layer growth or a time delay in the location of the separation point for trailing edge stall. For a HAWT the local relative wind speed and angle of attack are highly dynamic due to the presence of, for example, turbulence, wind shear, yaw angle, tower shadow and the deflections, movements and accelerations of the blades themselves [2].

As modern HAWT's are pitch regulated, they ideally do not enter the stalled regime. However, stall could still for example occur before the rated wind speed when the blades have not started to pitch out and the rotational speed is at the maximum value. This causes the blades to rotate at a tip speed ratio smaller than the optimum and then the airfoil will see an angle of attack higher than the design value. Here the blade is more vulnerable to a gust or yaw error pushing it into stall. This stalled flow, and in particular the onset of stall, is one of the most important phenomena for the aeroelastic stability of a wind turbine blade [9].
This unsteady external loading will excite the modes of the blade. Over each cycle of the oscillations the direction and magnitude of the forces will change due to the deflections and changing angle of attack and inflow velocities. Normally these oscillations are positively aerodynamically damped. However, if over each cycle the net work done adds energy into the structure, then the aerodynamic damping is negative and energy extracted from the flow. This energy is added to the oscillation in the blade and if this is larger than what the structural damping can dissipate, then the oscillation will grow in amplitude resulting in an instability. The end result will either be failure or a limit cycle oscillation where an equilibrium is reached due to the non-linear nature of the system [10]. Even though failure may not occur immediately in limit cycle oscillations, it will still reduce the fatigue life of the blades.

Therefore, dynamic stall is an important phenomenon to accurately model the aerodynamic forces and estimate the extreme and fatigue loads. However, there is a surprisingly large

uncertainty of about 30% on the dynamic loads between the predicted values and the field measurements [11][1]. This uncertainty could maybe be reduced by using a different, more accurate, dynamic stall model. From other 2D comparisons between dynamic stall models, such as in [8], [12], [13] or [14], the variability between different dynamic stall models is clear. Unfortunately, there is not much research into how much these different polars for sinusoidal motions translate into different outputs from the aeroelastic code as a whole using a turbulent flow input and full turbine. Furthermore, these comparisons are only into the lift coefficient, while the drag and moment coefficients are also important for some instabilities.

This Thesis will attempt to address these shortcomings by first conducting various 2D comparisons to experimental data for the lift, drag and moment coefficients followed by a comparison for several full turbine response cases in an aeroelastic code. The models evaluated are the Øye, Risø, Snel and ONERA models.
The 2D comparisons are conducted for sinusoidal pitching oscillations over a range of angles of attack and reduced frequencies relevant to HAWT's. The airfoils used are the NACA0015, NACA0030 and NACA4415 airfoils. Furthermore, various deep stall, high reduced frequency and ramp cases are investigated to test the boundaries of the models.
The full turbine cases are based on two International Electrotechnical Commission (IEC) Design Load Cases (DLC), namely DLC 1.4 and DLC 6.2. The DLC 1.4 is an extreme load case where a wind gust is combined with a large direction change. DLC 6.2 is an instability load case which states that a turbine must be able to survive any yaw misalignment when parked in a 50 year worst case storm. For these standstill cases the aerodynamic damping provided by each model is compared by reducing the structural damping of the blades to find the point where the blades become unstable. In addition to these IEC cases the effect of the dynamic stall models on the flutter speed is investigated.

1.2 Research questions

In order to reach this aim, various research questions are set up of which the main research question is:

- What is the effect of different dynamic stall models on aerodynamic instabilities in an aeroelastic code that uses BEM?

Before the effect of dynamic stall on the instabilities can be investigated, dynamic stall and the dynamic stall models themselves must first be understood. Therefore, the dynamic stall models are first compared to each other and to analytical and experimental data to answer the following:

- How well do the dynamic stall models perform for different angle of attack regimes?
  - How well do the dynamic stall models perform over the length of attached flow hysteresis loops?
    - How well do the hysteresis loops match the theoretical results?
    - How well do the hysteresis loops match the experimental data?

[1] It should be noted that this value is from 2007 and improvements have been made since.

    - What are the assumptions and reasons behind the differences?
  - How well do the dynamic stall models perform over the length of dynamic stall hysteresis loops?
    - How well do the polars match the measurements?
    - Is there any unphysical behaviour in the hysteresis loop?
    - What are the assumptions and reasons behind the differences?
    - What are the differences in torsional work done over each cycle (the area within the moment coefficient hysteresis loop)?

With the dynamic stall models implemented their effect on the chosen instability cases can be investigated by trying to answer the following for each dynamic stall model.

- What is the effect of the different dynamic stall models on the response of a full turbine?
  - How do the responses vary in the extreme load case (IEC design load case 1.4)?
    - What do the lift responses look like?
    - What are the differences in tip deflection?
  - How do the responses vary in the standstill cases (IEC design load case 6.2)?
    - How do the models behave under turbulent inflow?
    - What are the loads with the different models?
    - What are the damping levels of each model?
    - What are the blade modes excited when using each model?
  - How do the models affect the flutter limit?

1.3 Outline

This Thesis is organized as follows:

- In Chapter 2 the phenomenon of dynamic stall will be explained followed by the descriptions of the four dynamic stall models, the Øye, Risø, Snel and ONERA models. Afterwards follows a discussion on the modifications made to the models and some general limitations.
- In Chapter 3 the attached flow physics of the Risø and ONERA models is verified using both theory and experiments. Furthermore, the experimental methods for the dynamic stall measurement data are detailed.
- In Chapter 4 the model responses to the sinusoidal angle of attack inputs are compared against each other and to the experimental data for various cases.
- In Chapter 5 first aeroelastic codes and BEM are briefly covered, including the modifications made to the models to get them into the code, before comparing the models in an extreme load case, standstill instability cases and for the flutter limit. It additionally contains a sensitivity analysis into the results of the standstill instability cases to changes in the time constants in the Øye and Risø models.
- In Chapter 6 some basic tuning is done for the Øye and Risø models.
- In Chapter 7 the Thesis is then finalized with a conclusion.

CHAPTER 2

Dynamic Stall

Dynamic stall is an unsteady aerodynamic phenomenon that occurs when the angle of attack of an airfoil passes through the normal static stall angle [15]. Dynamic stall can cause hysteresis loops with significant deviations from the static polar as shown in Figure 2.1.

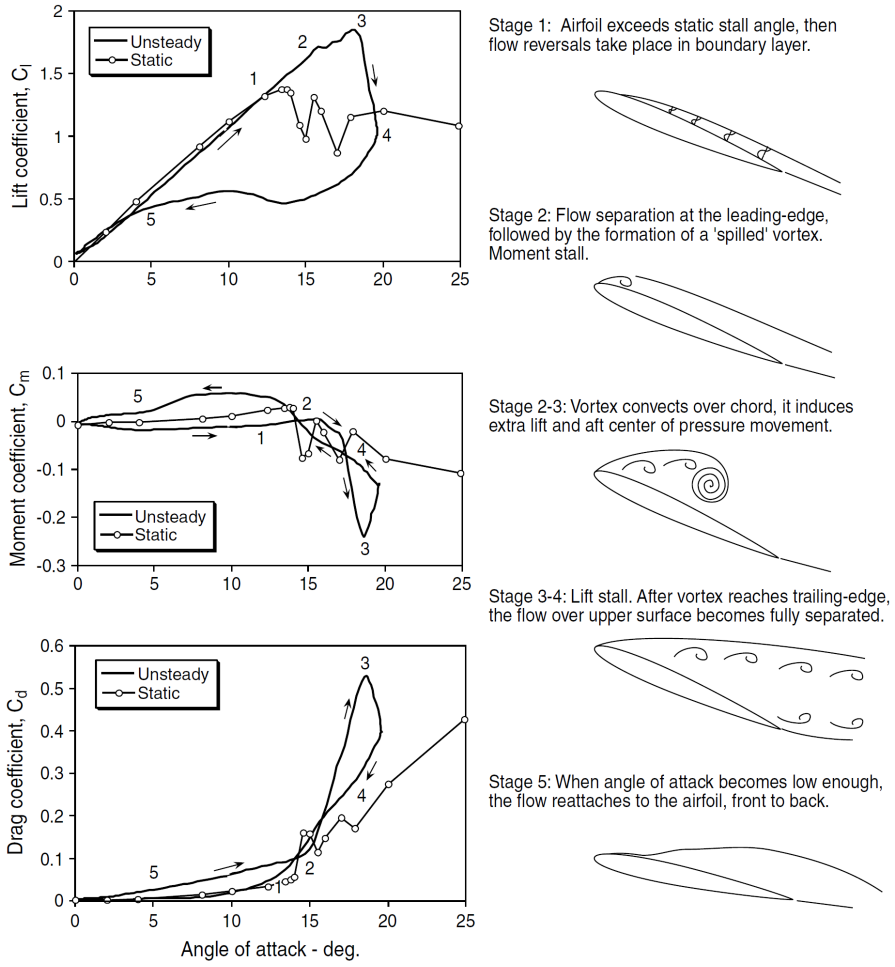

Figure 2.1: Example of the stages of a dynamic stall hysteresis loop for a sinusoidally changing angle of attack [15]

This figure also shows an example of the different steps of dynamic stall. After the airfoil surpasses the static stall angle, flow reversal starts to take place on the upper surface of the airfoil. If the airfoil is thin, so with a thickness to chord ratio smaller than 0.15, then in general the flow reversal will start at the leading edge causing leading edge stall. On the other hand, if $t/c > 0.15$, then trailing edge stall is usually predominant resulting in the flow reversal starting

at the trailing edge [16]. In either case, if the angle of attack is large enough, a spilled vortex is generated at the leading edge which convects over the airfoil surface at a speed of slightly less than half the inflow velocity [17].
Up to stage 3 the lift is still increasing and so will peak at a significantly larger value than the maximum static value. The movement of the leading edge vortex along the airfoil causes an aft movement of the center of pressure which results in a sharp drop in the moment coefficient and has an important effect on the stability of the motion. Once the vortex has convected behind the airfoil, the airfoil is fully stalled as usual which results in a sharp drop in the lift coefficient. Then once the angle of attack has decreased enough again, the flow will reattach from fore to aft.
It should be noted that these stages do not necessarily all occur for every dynamic stall occurence. Furthermore the dynamic curves do not necessarily contain the static curves due to the presence of phenomena which do not occur in the steady case. This is in particular the case for the drag coefficient as seen in Figure 2.1.

The size and shape of the dynamic stall hysteresis loop is affected by several parameters. The mean value and amplitude of the angle of attack during the loop are some of the most important parameters as they will determine the stall regimes that the airfoil will pass though in a cycle. These regimes are referred to as attached flow, light stall and deep stall regimes.
Another important parameter is the speed that the cycle is passed through indicated by the reduced frequency, $k = \frac{c\omega}{2U}$, which will cause the dynamic stall curve to vary more away from the static curve as it increases. If the inflow velocity is simplified to the rotational velocity of the blade, then k is only dependent on the blade slenderness as shown in Equation 2.1, which is only valid for 1P changes in the angle of attack.

$$k = \frac{c\omega}{2U} \approx \frac{c\omega}{2\omega r} \approx \frac{c}{2r} \tag{2.1}$$

For the NREL 5MW turbine [18] this gives k values of 0.12, 0.06, 0.03 and 0.02 for the radial locations, $\frac{r}{R}$, 30%, 50%, 70% and 90% respectively. It should be noted that in particular for the lower radii this method will overestimate the value of k as here the free stream wind speed is relatively more important.
Other parameters that have an affect dynamic stall are the Mach number, the airfoil shape, the Reynolds number and the type of motion [17]. The specific effect of some of these other parameters is detailed in Section 2.6 after the models have been introduced.

Due to the complexity of dynamic stall all engineering dynamic stall models are semi-empirical [15]. In particular the times of vortex creation and the reattachment are difficult to predict. Next the four models chosen to be implemented in this thesis are explained in more detail.

2.1 Øye

This is a simple dynamic stall model was developed by Stig Øye in the 1990's [6]. It uses a simple first order Ordinary Differential Equation (ODE) to simulate the time lag delay of the lift response to the changes in the angle of attack. This is achieved by using two separate lift curves, the fully attached flow curve and a fully separated curve. It then interpolates between

these two curves based on a variable called the interpolation factor f. This f indicates the relative importance of these two lift curves and is given a time lag using the ODE.
C_L^{att} is the attached flow lift curve and is a linear function with a slope of $\frac{dC_L^{st}}{d\alpha}\big|_{\alpha_0}$ (roughly 2π) and zero lift angle of attack, α_0, defined by the static lift curve of the used airfoil.
C_L^{sep} is the fully separated lift and will be estimated as in Larsen et al. [8]. This method sets the fully separated flow curve to be equal to the static curve after a certain angle of attack. This angle of attack is called α_{sep} for which a value of 32° is suggested [8]. For angles of attack smaller than α_{sep} a polynomial is set up using Hermite Interpolation as explained in Appendix A. The constraints for this polynomial are that it is equal to the steady value of the normal lift curve at α_0 and α_{sep} and that the derivatives here are $\frac{1}{2}\frac{dC_L^{st}}{d\alpha}\big|_{\alpha_0}$ and $\frac{1}{12}\frac{dC_L^{st}}{d\alpha}\big|_{\alpha_0}$ respectively [8]. In Øye's original paper [6] it is suggested to use a parabola with similar constraints although without the derivative constraint at α_{sep}. As this extra constraint increases the robustness to different static polars, the Hermite Interpolation method is seen as superior.
The ODE is defined in Equation 2.2, where T_f is a time constant proportional to c/U, so $T_f = \tau\frac{c}{2U}$ with τ a constant around 8 [9]. f^{st} is based on the interpolation factor of the steady lift curve between the attached and separated curves as shown in Equation 2.3. If the α_{sep} is exceeded, then Equation 2.3 is not needed as f^{st} is simply 0. The dot indicates the real time derivative: $\dot{} = d/dt$.

$$\dot{f}^{dyn} = \frac{f^{st} - f^{dyn}}{T_f} \tag{2.2}$$

$$f^{st} = \frac{C_L^{st}(\alpha) - C_L^{sep}(\alpha)}{C_L^{att}(\alpha) - C_L^{sep}(\alpha)} \tag{2.3}$$

The ODE in Equation 2.2 causes f^{dyn} to lag behind f^{st} which will generate the hysterises loops. This equation is then solved to obtain f^{dyn}, which is then used to do the interpolation between the attached and separated lift curves as in Equation 2.4.

$$C_L = f^{dyn}C_L^{att}(\alpha) + (1 - f^{dyn})C_L^{sep}(\alpha) \tag{2.4}$$

The method is summarized in a flowchart in Appendix B.
Overall this is a simple model that only needs the angle of attack and inflow velocity from the new time step together with the f from the previous time step as inputs. It does only output the dynamic lift coefficient and leaves the static drag and moment coefficients unmodified. Furthermore, it simply gives the steady lift value when the flow is attached or fully separated.

2.2 Risø

The Risø model [7] is significantly more complex than the Øye model using a total of four ODE's. It is a modified Beddoes-Leishman model so it uses the same building blocks as the Beddoes-Leishman model [3], which are:

1. Unsteady attached flow module
2. Leading edge flow separation module
3. Non-linear trailing edge separation module

4. Vortex shedding module

The Beddoes-Leishman model is a model that tries to follow the physics behind dynamic stall as accurately as possible. This does lead to the model becoming complex and dependent on more constants that require tuning. The Risø model adds some assumptions that are applicable to wind turbines to simplify the model and reduce the number of inputs. These assumptions are that the flow is assumed to be incompressible as the maximum tip speed is generally around 70-90 m/s (Mach 0.2-0.3) and, due to the relatively thick airfoils in turbine blades, the leading-edge flow separation and vortex shedding modules are removed as trailing edge stall will be predominant [16].
In the first module, the attached flow module, the geometrical angle of attack, α, is replaced with the effective angle of attack, α_E, which includes two time-lag terms and so accounts for circulatory effects. The time lags terms are based on the downwash ($w = \alpha U$) instead of the angle of attack as used in the Risø paper [7] to remove the $\dot{U}$ term which could make the exponent positive after the discretization in Appendix C. The use of either the downwash equations or $\dot{U}$ in the angle of attack equations is necessary to correctly account for the changes in relative velocity over time in the conservation of circulation.

$$\alpha_E = \alpha_{3/4}(1 - A_1 - A_2) + \left(w_1^{lag} + w_2^{lag}\right)/U \tag{2.5}$$

These time-lag terms follow from approximating the circulatory part of Duhamel's integral formulation using two time-lag terms. This will result in an indicial function as per Equation 2.6 where s is the non-dimensional time.

$$\phi(s) = 1 - A_1 e^{-b_1 s} - A_2 e^{-b_2 s} \tag{2.6}$$

This can be used as $\alpha_E = \alpha_{old} + (\alpha_{new} - \alpha_{old})\phi(s)$ for a step in α and so gives the build up over time to the new angle of attack. Instead of using this indicial notation, ODE's can be used to calculate the time-lag in the angle of attack. Doing so yields Equations 2.7 and 2.8 for the two lagged downwash velocity terms.

$$\dot{w_1^{lag}} + T_u^{-1} b_1 w_1^{lag} = b_1 A_1 T_u^{-1} \alpha_{3/4} U \tag{2.7}$$

$$\dot{w_2^{lag}} + T_u^{-1} b_2 w_2^{lag} = b_2 A_2 T_u^{-1} \alpha_{3/4} U \tag{2.8}$$

Here $T_u = \frac{c}{2U(t)}$, which is the time it takes for the flow to travel a half chord distance.
In the next module, the trailing edge stall module, several analytical functions are defined to predict the steady stall characteristics. For both the lift and drag the flat plate steady solution of the potential Kirchhoff flow is used. For the lift coefficient this flat plate solution is inverted to obtain Equation 2.9 for the steady flow separation point.

$$f^{st} = \left(2\sqrt{\frac{C_L^{st}(\alpha)}{C_L^{att}(\alpha)}} - 1\right)^2 \tag{2.9}$$

Where C_L^{att} is the same as in the Øye model f^{st} is then used to linearly interpolate between the fully attached and fully separated flow lift curves similar to Equation 2.4 in the Øye model, albeit for steady flow conditions here. This interpolation function is rewritten to move C_L^{sep} to the left hand side resulting in Equation 2.10.

$$C_L^{sep} = \frac{C_L^{st} - f^{st} C_L^{att}}{1 - f^{st}} \tag{2.10}$$

Using these equations all static curves are shown for the NACA64618 airfoil in Figure 2.2 together with those from Øye's model for comparison. For an airfoil with a more sudden stall, f^{st} will show a drop at stall for the Risø and Øye models.

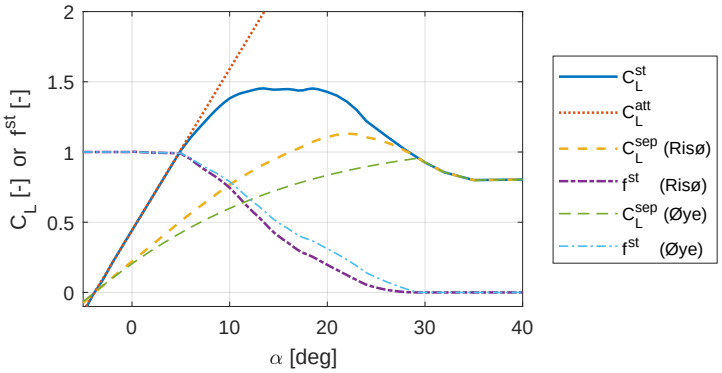

Figure 2.2: Example static curves used in the Risø and Øye models

A relatively large discrepancy is seen between the fully separated lift curves for the Risø method and the Hermite interpolation. Unfortunately, which of these two C_L^{sep} curves is more physical is hard to judge due to this static fully separated flow lift coefficient being mainly a theoretical concept.

The steady stall equations are now given a time delay using two more ODE's. Equation 2.11 accounts for the delay between the pressure around the airfoil and the lift generation, while Equation 2.12 simulates the dynamic effect of the development of the boundary layer over time.

$$\dot{C}_L^{att,lag} + T_p^{-1} C_L^{att,lag} = T_p^{-1} \left(C_L^{att}(\alpha_E) + \pi T_u \dot{\alpha} \right) \tag{2.11}$$

$$\dot{f}^{dyn} + T_f^{-1} f^{dyn} = T_f^{-1} f^{lag} \tag{2.12}$$

Where f^{lag} is the equivalent quasi-steady separation point for $C_L^{att,lag}$, $f^{lag} = f^{st}\left(\frac{C_L^{att,lag}}{C_{L_\alpha}} + \alpha_0\right)$, and f^{dyn} is the separation point with all delay effects taken into account. $C_L^{att,lag}$ is never used directly as a lift coefficient. It is only used in f^{lag} where it can be seen an extra delay effect on the effective angle of attack with regards to the separation point.

After solving the ODE's the dynamic lift, drag and moment coefficients can be calculated with Equations 2.13, 2.14 and 2.15 respectively.

$$C_L = f^{dyn} C_L^{att}(\alpha_E) + (1 - f^{dyn}) C_L^{sep}(\alpha_E) + \pi T_u \dot{\alpha} \tag{2.13}$$

$$C_D = C_D^{st}(\alpha_E) + (\alpha - \alpha_E) C_L + \left(C_D^{st}(\alpha_E) - C_{D,0}^{st} \right) \left(\frac{\sqrt{f^{st}(\alpha_E)} - \sqrt{f^{dyn}}}{2} - \frac{f^{st}(\alpha_E) - f^{dyn}}{4} \right) \tag{2.14}$$

$$C_M = C_M^{st}(\alpha_E) + \left(a^{st}\left(f^{dyn}\right) - a^{st}\left(f^{st}(\alpha_E)\right) \right) C_L - \pi T_u \dot{\alpha}/2 \tag{2.15}$$

The lift equation is similar to that of the Øye model, although f^{dyn} and C_L^{sep} are calculated differently and the leading added-mass term from potential flow theory has been included.
The dynamic drag is assumed to be the steady drag adapted with two unsteady correction terms. The first correction term is due to the unsteady lift coefficient changing the induced drag and the second correction is to account for the viscous drag differences between the steady and dynamic cases. The viscous drag is estimated using Kirchhof's potential flow approximation for a flat plate.
For the moment coefficient, again the steady curve is used as the base of the dynamic curve and then corrected. The first correction seen in Equation 2.15 is for the difference in moment arm (a^{st}) due to the dynamic separation point differing from the static value. The second term is an added-mass contribution from the motion. a^{st} is the arm between the quarter chord and the equivalent center of pressure. It is obtained empirically as a function of the separation point f^{st} where a^{st} is calculated using Equation 2.16 and then interpolated based on f.

$$a^{st} = \frac{C_M^{st} - C_{M,0}^{st}}{C_L^{st}} \tag{2.16}$$

There are six coefficients required in the Risø model, four airfoil dependent time lag constants and two flow dependent time constants. For the time constants, $T_p = \tau_p T_u$ and $T_f = \tau_f T_u$, the HAWC2 defaults are used which are $\tau_p = 1.5$ and $\tau_f = 6$ [19]. For the time lag parameters from Equation 2.6 either the flat plate solutions can be used, or values tailored to the airfoil. The values for the flat plate and a 24% thick Risø airfoil can be found in Table 2.1. For the Risø airfoil these results were obtained using an incompressible, inviscid panel code [7]. It is seen that the values vary significantly between the flat plate and 24% thick airfoil. Empirical approximations of these time lag constants exist for wind turbine airfoils such as [20]; however, the effect of using such airfoil specific constants in full turbine simulations is less than 2.5% for both ultimate and fatigue loads and additionally the effects on the flutter limit are minimal [20]. Therefore, the flat plate values are used.

Table 2.1: Different values for the time lag constants in the Risø model

Constant	Flat plate (Wagner) [21]	Risø A1-24 [7]
A_1	0.165	0.294
b_1	0.0455	0.0664
A_2	0.335	0.331
b_2	0.3	0.3266

The flowchart of this model can be found in Appendix B.

2.3 Snel

The Snel model [5] is unique compared to the other models here in that it uses different equations for the outgoing and returning loop of the hysteresis loop. Furthermore it tries to model the higher frequency component of the lift due to periodic vortex shedding and so can give oscillations within each cycle even for a smooth sinusoidal input. This model does not apply a correction to the angle of attack, but rather models the dynamic lift as the steady lift with two correction factors applied, $\Delta C_{L,1}$ and $\Delta C_{L,2}$ as in Equation 2.17.

$$C_L = C_L^{st} + \Delta C_{L,1} + \Delta C_{L,2} \tag{2.17}$$

The first correction term is to account for the forcing frequency response and the second correction term is added to estimate the higher frequency dynamics such as periodic vortex shedding. Using the dynamic stall measurements on the NACA4415 and NREL S809 airfoils from the Ohio State University, OSU, database [22], the coefficients and forcing terms have been tuned by Snel [5] to match reasonably without requiring any airfoil specific inputs. It should be noted that only hysteresis loops with an average angle of attack of 14° and an amplitude of 10° are used over three reduced frequencies: low ($k \approx 0.02$), medium ($k \approx 0.04$) and high ($k \approx 0.06$) and a single Reynolds number of 1.2 million.
The ODE for the first lift correction term is found in Equation 2.18.

$$\Delta \dot{C}_{L,1} + T_u^{-1} c_{10} \Delta C_{L,1} = \Delta \dot{C}_L^{pot} \tag{2.18}$$

T_u here is the same as in the Risø model being equal to $\frac{c}{2U}$. On the right hand side of the equal sign is the forcing term due to the occurrence of stall, where the ΔC_L^{pot} is defined in Equation 2.19 as the difference between the potential flow lift and the steady lift.

$$\Delta C_L^{pot} = \left.\frac{dC_L^{st}}{d\alpha}\right|_{\alpha_0} \sin(\alpha - \alpha_0) - C_L^{st} \tag{2.19}$$

This ΔC_L^{pot} can be seen as a switch between the attached flow and stalled flow regime as it will be close to zero before stall and then start affecting the system of equations after stall.
The coefficient c_{10} is shown in Equation 2.20 [12]. It can be seen as the spring stiffness for the ODE and so the dynamic lift coefficient will pull stronger back towards the static curve when ΔC_L^{pot} is large, when $|\dot{\alpha}|$ is small on an outgoing loop and when $|\dot{\alpha}|$ is large on a returning loop. The inverse of c_{10} can be seen as the time constant of the system, so Snel's model has, in effect, a variable time constant.

$$c_{10} = \begin{cases} \frac{1+0.5\Delta C_L^{pot}}{8+640 T_u |\dot{\alpha}|} & \text{if } \dot{\alpha} C_L^{pot} > 0 \\ \frac{1+0.5\Delta C_L^{pot}}{8-480 T_u |\dot{\alpha}|} & \text{if } \dot{\alpha} C_L^{pot} \leq 0 \end{cases} \tag{2.20}$$

Next, Equation 2.21 shows the ODE for the second correction term from Equation 2.17. This ODE must be at least second order to be able to model the higher frequency components of the lift response.

$$T_u^2 \Delta \ddot{C}_{L,2} + c_{21} \Delta \dot{C}_{L,2} + c_{20} \Delta C_{L,2} = 0.015 \left(-0.15 \Delta C_L^{pot} + 0.05 \Delta \dot{C}_L^{pot} \right) \tag{2.21}$$

The constants are again obtained by matching to the OSU experimental data and are calculated as

$$c_{20} = k_s^2(1 + 3\Delta C_{L,2}^2)(1 + 3\dot{\alpha}^2) \tag{2.22}$$

$$c_{21} = \begin{cases} 60T_u k_s \left(-0.01(\Delta C_L^{pot} - 0.5) + 2\Delta C_{L,2}^2\right) & \text{if } \dot{\alpha} C_L^{pot} > 0 \\ 2T_u k_s & \text{if } \dot{\alpha} C_L^{pot} \leq 0 \end{cases} \tag{2.23}$$

The k_s is the Strouhal vortex shedding frequency, equal to 0.2. It is noted that the state variable $\Delta C_{L,2}$ is used to determine c_{20} and also c_{21} when $\dot{\alpha} > 0$. This makes the ODE non-linear and so makes solving exactly problematic as multiple mathematical solutions for the new $\Delta C_{L,2}$ could exist. This is avoided by using the state variable $\Delta C_{L,2}$ from the previous time step in Equations 2.22 and 2.23 and so making the ODE in Equation 2.21 linear again. The set of equations in this model is summarized into a flowchart in Appendix B.

2.4 ONERA

The last model is the ONERA model which is at its heart based on the assumption that the forces and moments acting on the airfoil can be determined by a system of equations with as only variables the force and moment coefficients, the angle of attack, the pitch and the inflow velocity together with their derivatives and time histories [4]. The choice of which of these derivatives can be neglected is made through assumptions and identification using experimental data. The most important assumptions are that pitching velocity is small either by having a limited amplitude or frequency of oscillation and that the deviations from the static force curves are small. This allows for many of the higher derivatives to be neglected and for the equations to be linearised. Then the model is further simplified by using a small angle approximation and empirically by identification through comparing to experimental data at various wind speeds, angles of attack and reduced frequencies.
Here the extended version of the ONERA model is implemented [23]. This extended equation implements some changes suggested by Peters [24] to differentiate between pitch and plunge, prevent the model from becoming unstable in deep stall and also gives the model a more theoretical base by making the model reduce to Greenberg's equations [25] in the attached flow region. Greenberg's equations are derived off Theodorsen's equations and account for a sinusoidally varying inflow velocity.
The differentiation between pitch and plunge is done by using two downwash terms instead of the angle of attack. W_0 is the non-dimensional downwash at the quarter chord point and W_1 is the difference in downwash between the three-quarter chord point and the quarter chord, so is indicative of the rotational motion. This is why θ is used instead of α, as θ is the angle of attack component due to the pitch angle with respect to the incoming airflow only. W_0 and W_1 can be found in Equations 2.24 and 2.25 respectively. The apostrophe in Equation 2.25 indicates differentiation to the non-dimensional time, s.

$$W_0 = \sin(\alpha) \tag{2.24}$$

$$W_1 = \theta' \tag{2.25}$$

The main equation for the lift is in Equation 2.26.

$$C_L = s_L W_0' + k_L W_1' + C_{L,1} + C_{L,2} \tag{2.26}$$

This equation is similar to Snel's model with the difference that the steady lift is contained inside the state variables as in steady flow W_0' and W_1' will go to zero, $C_{L,1}$ will tend to C_L^{pot} and $C_{L,2}$ will end up as -ΔC_L^{pot}. Their sum will then simply become the steady lift coefficient.

Equation 2.27 contains the ODE for the first lift component which, with the exception of the d_L term, models the attached flow behavior.

$$C_{L,1}' + \lambda C_{L,1} = \lambda \left(C_L^{pot} + \sigma_L W_1 \right) + \left(m_L \left. \frac{dC_L}{d\alpha} \right|_{\alpha_0} + d_L \right) W_0' + \sigma_L m_L W_1' \tag{2.27}$$

The second ODE is in Equation 2.28 and models the post-stall behavior.

$$C_{L,2}'' + a_L C_{L,2}' + r_L C_{L,2} = -r_L \Delta C_L^{pot} - e_L W_0' \tag{2.28}$$

The coefficients in the above equations are obtained from the Equations 2.29 to 2.34 using the values displayed in Table 2.2.

$$C_L^{pot} = \left. \frac{dC_L^{st}}{d\alpha} \right|_{\alpha_0} \sin\left(\alpha - \alpha_0\right) \tag{2.29}$$

$$\Delta C_L^{pot} = C_L^{pot} - C_L^{st} \tag{2.30}$$

$$d_L = d_1 \left| \Delta C_L^{pot} \right| \tag{2.31}$$

$$r_L = \left(r_0 + r_2 \left(\Delta C_L^{pot} \right)^2 \right)^2 \tag{2.32}$$

$$a_L = a_0 + a_2 \left(\Delta C_L^{pot} \right)^2 \tag{2.33}$$

$$e_L = e_2 \left(\Delta C_L^{pot} \right)^2 \tag{2.34}$$

The ΔC_L^{pot} gives an indication on how deep into stall the airfoil is similarly to in Snel's model. Due to this property it is used to modify some of the airfoil coefficients based on the level of stall such as in Equations 2.31 to 2.34.

A similar equation is used for the drag shown in Equation 2.35.

$$C_D = C_{D,0}^{st} + \sigma_D W_0' + C_{D,1} \tag{2.35}$$

Where σ_D is calculated using $\sigma_D = \sigma_0 W_0 + \sigma_1 \left| \Delta C_L^{pot} \right|$ and $C_{D,1}$ using Equation 2.36.

$$C_{D,1}'' + a_D C_{D,1}' + r_D C_{D,1} = -r_D \Delta C_D - e_D W_0' \tag{2.36}$$

Where $\Delta C_D = C_D^{st} - C_{D,0}^{st}$.

For the moment again a similar method is used as in Equation 2.37.

$$C_M = C_M^{lin} + \bar{\sigma}_M W_0' + \sigma_M W_1 + s_M W_1' + C_{M,1} \tag{2.37}$$

Where C_M^{lin} is first order Taylor expansion around $\alpha = 0$ of the steady moment curve, $C_M^{lin} = C_M^{st}|_{\alpha=0} + \alpha \left.\frac{dC_M^{st}}{d\alpha}\right|_{\alpha=0}$, and $C_{M,1}$ is obtained using the ODE in Equation 2.38.

$$C''_{M,1} + a_M C'_{M,1} + r_M C_{M,1} = -r_M \Delta C_M - e_M W'_0 \tag{2.38}$$

Here $\Delta C_M = C_M^{st} - C_M^{lin}$,

The values of the coefficients in Equations 2.31 to 2.34 can be found in Table 2.2 and the rest of the coefficients are [23]: $\lambda = 0.17$, $\Delta\tau = 8$, $m_L = 0.53$, $s_L = 2\pi$, $k_L = \pi/2$, $\sigma_L = 2\pi$, $\sigma_0 = 9.8484$, $\sigma_1 = -2.2918$, $\sigma_M = -\pi/2$, $\bar{\sigma}_M = -\pi/4$, $s_M = -0.5879$. λ is the inverse of the non-dimensional time constant for the attached flow physics and $\Delta\tau$ which gives the time delay of stall in non-dimensional time. Despite $\Delta\tau$ not being used in any of the equations, it will affect the dynamic coefficients by forcing ΔC_L^{pot} to stay small until a certain non-dimensional time has passed. Hereafter ΔC_L^{pot} instantly goes back to its normal value as calculated in Equation 2.30. To achieve this a second C_L^{st} curve is used during $\Delta\tau$ where the lift continues to increase after stall instead of decreasing. A suitable post-stall delayed lift slope is found to be one fifth the attached flow lift slope.

Table 2.2: Flat plane and mean airfoil values for the constants in the ONERA model using $M = 0$ [23]

Constant	Lift value	Moment value	Drag value
a_0	0.3	0.25	0.25
a_2	0.2	0.1	0
e_2	-2.8648	0.5730	-0.8594
r_0	0.2	0.2	0.2
r_2	0.2	0.2	0.2

The ONERA model is the model that uses the most coefficients by far. A flowchart of the ONERA method is shown in Appendix B.

One of the main limitations of the ONERA model is that small deviations between the dynamic and static force and moment coefficients are assumed which reduces the accuracy when the reduced frequency is large. The small angle approximation made by the original ONERA model also limits the applicability. The result of both these assumptions is that there will be significant error when the reduced frequency and amplitude are high as shown by water tunnel measurements [26]. Although this has somewhat been improved in this implementation by making the coefficients d_L, r_L, a_L and e_L indirectly amplitude dependent through ΔC_L^{pot}.

The assumption of incompressible flow is not made in the ONERA model and the Mach number is used for some of the coefficients. As the Mach numbers as seen by a wind turbine are small these Mach number effects on the coefficients are ignored to save computational time. Now, similar to the other dynamic stall models, this model should only be used in the incompressible regime.

2.5 Modifications

To make the models robust and work over the full 360° several modifications are required. These modifications are detailed in Sections 2.5.1 to 2.5.7 and the resulting hysteresis loops over the range 0° to 180° shown in Appendix D.

2.5.1 Potential flow curve

The potential flow curve, or attached flow curve, is modified such as that the actual lift slope is used instead of 2π. This true lift slope is found using curve fitting around the zero lift point. The upside down lift slope is found in a simplified way where the lift slope is assumed to be the steepest slope between the zero lift point and any of the points on the lift curve. This is a robust way of finding the lift slope as the lift curve can never exceed the potential flow curve meaning that the f in the Øye and Risø models can never go above 1.
For all models this curve is further modified to allow for the model to be used over the full 360°. For the Øye, Risø and Snel models this is done by making C_L^{pot} discontinuous at the angle of attacks close to 90° and -90° where $C_L^{st} = 0$. Here the C_L^{pot} jumps from the value for the upright airfoil to that for the upside down airfoil. In the Risø and Snel models this requires the C_L^{pot} value stored from the previous time step to be shifted to the new curve. For the ONERA model this was found to not completely fix the behaviour when passing through these jumps in C_L^{pot}. Furthermore the lift coefficient hysteresis loops were seen to be rotating in the wrong direction (counter-clockwise) in deep stall when compared to what one would one would expect from implementing a time lag. Therefore C_L^{pot} is transitioned smoothly in the ONERA model between the two C_L^{pot} curves by limiting C_L^{pot} to be a maximum of 4 times C_L^{st}. This factor of 4 is taken from the Risø model where $f^{st} = 0$ when $\frac{C_L^{pot}}{C_L^{st}} \geq 4$.

2.5.2 Phasing out at large α

Because dynamic stall is a phenomenon seen when passing in and out of stall the models should not have much effect when oscillating when the flow is already fully separated. Here bluff body aerodynamics with phenomenon such as periodic vortex shedding should become more relevant. The Øye and Risø model already phase out when $\frac{C_L^{pot}}{C_L^{st}} \geq 4$ is reached. For the Snel and ONERA models modifications are required to phase out the model behaviour. This is achieved by multiplying the time derivatives in the forcing terms by $|\cos(\alpha)|$. The specific forcing terms where this is applied are $\dot{C}_L^{pot}$ for Snel's model and for the ONERA model W_1 and W_0'.
Another issue far into stall is what to do with the attached flow terms from Theodorsen's theory in the Risø and ONERA models. The circulatory terms are left unchanged as these are from the conservation of circulation which should not be broken. For the added-mass terms in Theodorsen's theory, on the other hand, it makes less sense to have these active a high angles of attack, therefore a projection of the relative velocity on to the chord is made to prevent the velocity component perpendicular to the chord from affecting these added-mass terms. This results in these terms also being phased out with $|\cos(\alpha)|$. This is not a perfect fix as the added-mass terms will still be slightly active when the flow is fully stalled while Theodorsen's theory assumes attached flow. Another option looked into is the use of f^{dyn} to phase out these

terms in the Risø model. This does, however, affect the shape of the dynamic stall hysteresis loops which is undesirable.

2.5.3 Reverse flow

In the case that the airfoil is operating upside down, so in reverse flow, several simplifications are made to simplify the code. First the stall delay for the lift in the ONERA model is ignored and the right-side-up value for C_M^{lin} is used. For the Risø model the moment is simplified as the difference in moment arm, a^{st}, between the steady and dynamic cases is ignored. These assumptions do affect the shape of the moment hysteresis loop when upside down, although the same general behaviour is maintained. There are arguably much more severe issues with the use of these models in reverse flow as the airfoil shape will be unconventional and the sharp leading edge with upside down camber could produce a large laminar reverse flow bubble at the higher angles of attack in attached flow. In any case it will cause leading edge stall which none of the models predict well.
When passing through the $\alpha = \pm 180°$ points care should be taken to shift the stored α values from the previous time step by $\pm 360°$ to prevent the models from seeing a large α time derivative. This shift is also required for the lagged downwash terms in the Risø model.

2.5.4 Integration

The ODE's will be solved using exact integration from $-\Delta t$ to the current time step with the assumption of constant coefficients. The equations can be found in Appendix C. To increase the accuracy the midpoint rule is used to obtain the ODE coefficients. This is achieved for the Øye, Risø and ONERA models by averaging all the time dependent variables individually between the current and previous time step. For Snel's model this is not possible due to different equations being used depending if the angle of attack is outgoing or returning. Therefore for Snel's model the final coefficients for the ODE are averaged and not the inputs to these coefficients.

2.5.5 Øye and Risø models

For the Øye and Risø models only minor further modifications are required. The first of which is that limits are imposed on f^{st} such that it can never become negative which prevents the possibility of the separation point leaving the leading edge. This could occur if $|C_L^{sep}| > |C_L^{st}|$ which is not physical as the fully separated curve should the worst case possible for the lift. Therefore if this occurs then the fully separated curve is set to the static curve: $C_L^{sep} = C_L^{st}$. In attached flow it is possible for f^{st} to go higher than 1 if the static lift is larger than the potential lift which could happen if the linear part of the static curve is not completely linear, due to for example measurement noise or the curve fitting giving a slightly too low lift slope. Then the separation point could leave the trailing edge which is also unphysical. This separation point is only used as an interpolation factor, however, and so still functions outside of the range 0 to 1. Furthermore, to apply an upper limit to f^{st} either C_L^{st} or C_L^{pot} must be modified and neither is desirable.
A compromise is made in that f^{st} is limited to a maximum of 1.2, which allows for some

flexibility before having to make C_L^{pot} locally deviate from being linear. C_L^{st} is left unchanged.

In rare cases when the angle of attack was seen to rapidly change from attached flow to 90° at the inboard sections where the relative velocity is low and the chord is large, f^{dyn} is seen to decrease so slowly to 0 that it is still non-zero when passing through the $C_L^{st} = 0$ points close to 90° and -90° where C_L^{pot} is discontinuous. If this occurs the models will give unphysical results due to the potential flow curve being discontinuous and the potential flow reversing direction over the airfoil in the models. Therefore, f^{dyn} is set to zero when passing through these $C_L^{st} = 0$ points close to 90° and -90°.

The α_{sep} for the Hermite interpolation in Øye's model is calculated automatically as the location where the ratio of C_L^{pot} and C_L^{st} is equal to 4 as in the Risø model. This additionally allows for different α_{sep} values to be used for both positive and negative stall when both right-side-up and upside down.

Finally the moment arm, a^{st}, in the Risø model is rather arbitrarily truncated at the edges where $f^{st} = 0$ and $f^{st} = 1$ such that the slope $\Delta a^{st}/\Delta f^{st} < 1$. This is necessary to prevent sudden jumps in C_M near the edges of f^{st}; however, means that the a^{st} vs f^{st} curve may not cover all f^{st}'s. When interpolating, if f^{st} or f^{dyn} are outside the range of a^{st}, then the edge value of a^{st} is used instead of extrapolating to turn the correction off.

2.5.6 ONERA model

Changes required for the ONERA model other than that in C_L^{pot} are that the sign of W_0 must be flipped when $|\alpha| > 90°$ due to the trailing and leading edges now having swapped positions. When passing through $|\alpha| = 90°$ the sign of the W_0 from the previous time step must also be multiplied with -1 to prevent a large time derivative.
Furthermore the terms affected by $\ddot{\alpha}$ in the ONERA model, the W_1' terms, are removed as these terms have a minimal effect on the polars and are found to be susceptible to noise as any noise in α will be amplified each time the derivative is taken. This was noted by Snel when looking at the measument data [5] and is shown in Appendix E where the impact of this term in the ONERA model is compared for an angle of attack input both with and without noise.
Finally, in the pure pitching case the added-mass terms from Theodorsen for the pitch and plunge are both included for the moment coefficient. Therefore the added-mass term for the plunging motion is subtracted from that of the pitching motion, so σ_M is changed from $-\pi/2$ to $-\pi/4$. Now good agreement is found between Theodorsen's theory and the ONERA model for C_M in Section 3.1.

2.5.7 Snel's model

The equations for Snel's model as used in Section 2.3 are slightly different than those in Snel's original paper as it was found that the equations gave results that did not match the plots shown in the paper. Therefore the equations for c_{10} as used by Holierhoek et al. [12] are used. This increases the relative importance of the first order correction term with respect to the second order term by a factor 8. Therefore this factor 8 is compensated for in the second order correction term by dividing the forcing term by 8. This results in very similar hysteresis loops

to those in Snel's original paper. The small differences that are present may be due to slight differences in the steady lift curve or the integration method.
In the end this is not important as the whole second order correction term will be neglected based on three reasons: First it results in a steady state error due to the presence of ΔC_L^{pot} in the forcing term which does not decay to zero when steady. Secondly there are two real time derivatives that are not multiplied with the time constant and so are still dimensional which results in different equations for the same k depending on the wind speed or chord length. Finally it introduced rather severe high frequency oscillations in deep stall exclusively on the outgoing part of the loop. A short comparison of the full Snel's model with Snel's model with the second order correction term neglected can be found in Appendix F.
A smaller issue is corrected in the first order correction term as on the returning part of a hysteresis loop ($\dot{\alpha} C_L^{pot} \leq 0$) as with increasing $|\dot{\alpha}|$ the denominator of c_{10} first goes to zero and then negative. As c_{10} can be seen as the spring stiffness of the first order ODE, a negative value will cause unstable results and a too high value of c_{10} will cause the hysteresis loop to tightly hug the steady curve which is seen as unphysical. Large enough $|\dot{\alpha}|$ values for this to occur are found to only occur for k>0.1 in the pure sinusoidal oscillation case and so only occur in the most extreme cases. To prevent these issues the denominator of Equation 2.20 is limited to a minimum value of 2. This value is relatively arbitrary and is only based on the rough preservation of the shape of the hysteresis loop between the k values the model is tuned to and the range $k = 0.08$ to 0.12. This limit has no effect on the hysteresis loops in the range of k's the model is designed for and only prevents unphysical behaviour for higher k's. The same limit is applied on $|\dot{\alpha}|$ for the outgoing part of the loop to prevent the dynamic lift coefficient straying too far from the static curve, although even with this cap Snel's model still shows rather high peak C_L's for large k's as shown in Appendix D.2.

2.6 General limitations

There are some limitations that are shared by all of the aforementioned models. These are detailed in this section starting with incompressibility.
The incompressibility assumption is reliant on the Mach number, M, being much lower than 1. Generally the tip speed of a turbine is limited to the range of 70 - 90 m/s due to noise constraints. Using the sea level speed of sound of 343 m/s this equates to a maximum M between 0.204 and 0.262. If a 2D slender airfoil is assumed then the Prandtl–Glauert transformation can be used to transform the potential flow coefficients to compressible coefficients as long as no transonic phenomena are present. This is done using Equation 2.39 for the lift coefficient and the same correction applies to the drag and moment coefficients [2].

$$C_L = \frac{1}{\sqrt{1 - M^2}} \, C_L|_{M=0} \tag{2.39}$$

Using $M = 0.204$ and $M = 0.262$ gives an increase in coefficient of 2.1% and 3.6% respectively which falls into the uncertainty margins of the dynamic stall models as shown in Chapter 4. These numbers are only rough estimates of the effect of compressibility as the flow for wind turbines is highly three dimensional and has high Reynolds numbers. Both of which violate the assumptions made in the Prandtl–Glauert transformation. It will give the correct order of magnitude of the effect of compressibility, though. Of course it would be better to account for compressibility in the dynamic stall model. This is done in the Beddoes-Leishman

model [3] and the original implementation of the ONERA model [4]; however, will increase the computational time. On top of this, the complexity is increased due to having Mach number dependent input parameters. Therefore, this is not recommended for such a small accuracy increase.
Additionally, experiments have shown that there is very little variation in the shape of dynamic stall hysteresis loops for Mach numbers below 0.2 [27].
It should be noted that for compressibility not only the Mach number is important, but also the reduced frequency of the oscillation. This gives another criteria for the incompressible flow assumption to hold. Namely that the frequency of the unsteady effects sould be such that $kM \ll 1$ [15]. For most cases in a wind turbine k will be much smaller than 1 and in particular near the outboard section where most of the power is generated, therefore this criteria will also be met.

More errors will be introduced by the models that don't use airfoil specific parameters or when generalized airfoil inputs are used as the hysteresis loops are airfoil dependant [15]. In a wind turbine this is of importance due to the large changes in airfoil shape and thickness along the span. Airfoils with a sharp leading edge, so in general thin airfoils, will experience leading edge stall which is much more abrupt than the more gradual trailing edge stall. Additionally for trailing edge stall, the unsteady effects will help suppress separation. Therefore, there will be less chance of negative damping based on how gradual the trailing edge stall is [27].

The pitch and plunge are combined into the angle of attack without distinguishing between them for the dynamic stall behaviour which also adds modelling errors. Experiments have shown that the dynamic stall behaviour between pitching and plunging is slightly different even when the effective angle of attack is the same [28]. This is due to the leading edge pressure gradient being decreased by the pitch rate which delays the onset of stall.

All models additionally assume a 2D situation while the flow over wind turbine blades is highly three-dimensional. One important part of this 3 dimensionality are the tip and root vortices which cause finite span effects. These are generally modelled using Prandtl's tip correction or another similar correction that simply multiplies the lift by a factor based on the location along the span. When dynamic stall occurs inside the region affected by this tip vortex this is a too simple approximation as the tip vortex will deform the shape of the dynamic stall curve [15]. Another 3D effect is that the rotation of the blade will result in centrifugal and Coriolis forces in the boundary layer flow. The Coriolis acceleration terms in particular can delay the onset of stall by reducing the adverse pressure gradients over the chord length [15]. In general the rotation will cause stall delay on the inboard sections for which corrections exist for the static curves such as [29]. The dynamic stall behaviour along the span will additionally be distorted as shown by Schreck and Robinson [30].
Furthermore there is the effect of the local sweep angle. This sweep angle can be present due to the design of the blade shape or due to operating in yawed conditions and causes spanwise flow. This spanwise flow can cause interactions between the different radial locations which is a violation of the 2D assumption made by all dynamic stall models and so will result in changes to the local hysteresis loops. Measurements have shown that positive sweep will delay stall until a higher angle of attack and can also change the mean value of the hysteresis loop [31].

None of the models take the Reynolds number into account for the dynamic loop. The only

place where the Reynolds number will affect the results is in the static polars which can be seen as the backbone for the dynamic loops.
A final limitation is that none of the models have been verified for deep stall. Neither do the measurement campaigns used here, which is possibly due to wind tunnel limitations and blockage effects. Therefore the behaviour here is guess work at best. The Risø model is possibly the most physical model in deep stall as it reduces to the steady forces together with the terms for the conservation of circulation. However, the conservation of circulation equations are based on potential flow theory and there are other effects present in deep stall which none of the models capture.

CHAPTER 3

Verification

For verification both analytical equations and experimental data will be used for the attached flow, while for the separated flow cases only experimental data will be used.

3.1 Theodorsen

For the models that show attached flow hysteresis loops the cycles will be verified using Theodorsen's theory [32]. This theory uses a linearised potential flow model using a 1D sheet of vortices starting at the leading edge and continuing to infinity. Other assumptions are potential flow, harmonic oscillations in pitch and heave, zero perturbation velocity in far-field, flow tangency on airfoil surface, the Kutta condition (no pressure jump at the trailing edge between the upper and lower airfoil surface), Kelvin's Theorem (total circulation is constant) and an uncambered airfoil.

This results in the lift and moment equations in Equations 3.1 and 3.2 which are dependent on the pitching and plunging of the airfoil with respect to the incoming airflow. The equations are built up out of two physically distinct parts: the circulatory and non-circulatory components. The circulatory terms are from the generation of circulation in the wake due to the changing lift combined with Kelvin's theorem. The non-circulatory terms are from the acceleration of the air due to the (relative) movement of the airfoil and are called added-mass terms. The moment equation assumes that the aerodynamic center is at the quarter chord.

$$C_L = \pi \left(\frac{c\dot{\theta}}{2U} + \frac{c\ddot{h}}{2U^2} - a\frac{c^2\ddot{\theta}}{4U^2} + 2C(k) \left[\theta + \frac{\dot{h}}{U} + \left(\frac{1}{2} - a \right) \frac{c\dot{\theta}}{2U} \right] \right) \tag{3.1}$$

$$C_M = -\frac{\pi}{2} \left(\left(\frac{1}{2} - a \right) \frac{c\dot{\theta}}{2U} + \left(\frac{1}{8} + a^2 \right) \frac{c^2\ddot{\theta}}{4U^2} - a\frac{c\ddot{h}}{2U^2} \right) + \pi C(k) \left(a + \frac{1}{2} \right) \left(\theta + \frac{\dot{h}}{U} + \left(\frac{1}{2} - a \right) \frac{c\dot{\theta}}{2U} \right) \tag{3.2}$$

Here a is positive towards the trailing edge and is both the axis to which C_M is defined and the location of the center of rotation of the airfoil with respect to the mid-chord. Therefore, as the rotation (and C_M) is about the quarter chord, $a = -0.5$. Theodorsen's function, $C(k)$, is approximated using the rational function in Equation 3.3 to avoid the use of Bessel functions.

$$C(k) = 1 - \frac{0.165}{1 - j0.0455/k} - \frac{0.335}{1 - j0.3/k} \tag{3.3}$$

Here j is $\sqrt{-1}$. Then first a pure pitching motion is looked into where θ is set to be sinusoidal, $\theta = \bar{\theta} e^{j\omega t}$. This is then inserted into Equations 3.1 and 3.2 together with $a = -0.5$ to obtain Equations 3.4 and 3.5.

$$C_L = 2\pi\theta \left(\frac{1}{2}jk - \frac{1}{4}k^2 + (1 + jk)\, C(k) \right) \tag{3.4}$$

$$C_M = \frac{\pi}{2}\theta k\left(\frac{3}{8}k - j\right) \tag{3.5}$$

This gives a complex number for the coefficients as it not only contains information on the magnitude, but also on the phase of the coefficients. To make the plots, the real part of the coefficients are taken. If the airfoil is cambered, then $C_{L,0}$ must be added to the lift component to obtain the correct lift and for the moment the steady values are added to Theodorsen's result. The results for C_L and C_M can be seen in Figure 3.1. α_m stands for the mean angle of attack and α_a for the amplitude. The experimental data is from the University of Glasgow [33] and is detailed more in Section 3.3.

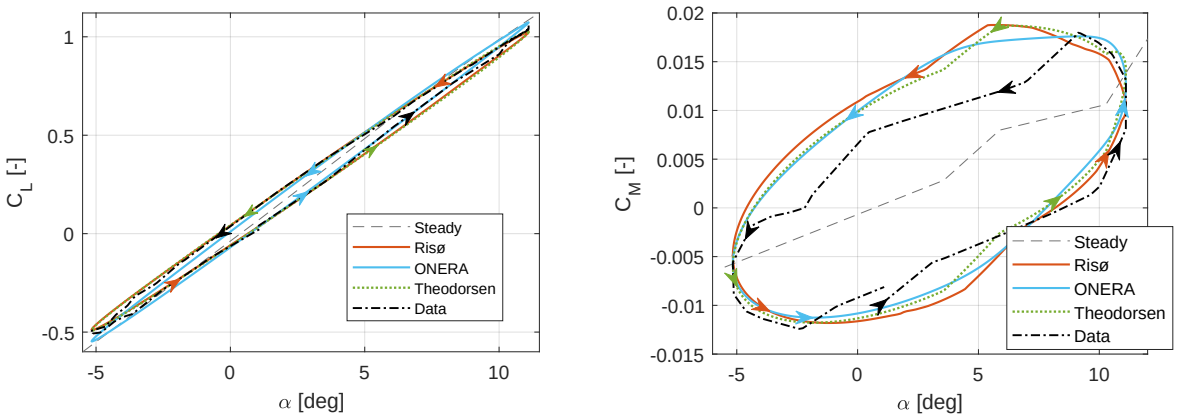

(a) C_L vs α (b) C_m vs α

Figure 3.1: Comparison between Theodorsen's function, the Risø and ONERA dynamic stall models and experimental data of the NACA0015 airfoil where $k = 0.051$, $\alpha_m = 3°$, $\alpha_a = 8°$ where the data is obtained at $Re = 1.48$ million and $M = 0.119$

For the lift coefficient a close match with Theodorsen's theory is seen for the Risø model. The ONERA model hysteresis loop is similar, although slightly underrotated from the static lift curve. This rotation of the hysteresis loop is harder for the ONERA model to capture as it uses the angle of attack without wake effects for these steady coefficients. The Risø model, on the other hand, uses the time-delayed angle of attack based on two ODE's for the steady coefficients. The ONERA model then uses only one ODE to add the time delay, the phase difference, to the steady C_L. As it is the lift coefficient that is delayed the resulting phase delay will be additionally dependent on the lift slope.
The experimental data shows good alignment with Theodorsen's theory and the dynamic stall models, with the exception of the highest angles of attack. Here the flow start to separate ever so slightly which causes the data, and to a lesser extent the models, to deviate from the theory. For the moment coefficient the models both perform equally well as the dominant term is the first added-mass term which both models contain. The slight difference between the models is largely due to the delay in effective angle of attack imposed by the Risø model.

Next a pure plunging motion is considered where the plunge is defined as positive downwards and is non-dimensionalized using the half chord, $\tilde{h} = \frac{2h}{c}$. Again a sinusoidal motion is used which gives $\tilde{h} = \bar{\tilde{h}}e^{j\omega t}$ resulting in Equation 3.6.

$$C_L = 2\pi\tilde{h}k\left(jC(k) - \frac{1}{2}k\right) \tag{3.6}$$

$$C_M = -\frac{\pi}{2}ak^2\tilde{h} \tag{3.7}$$

The only changes made to the models in order to account for this different motion type are that $\alpha_{3/4} = \alpha$ for the Risø model and $W_1 = 0$ for the ONERA model. For the steady curve this time a simple 2π slope is used for the lift and 0 is used for the moment.

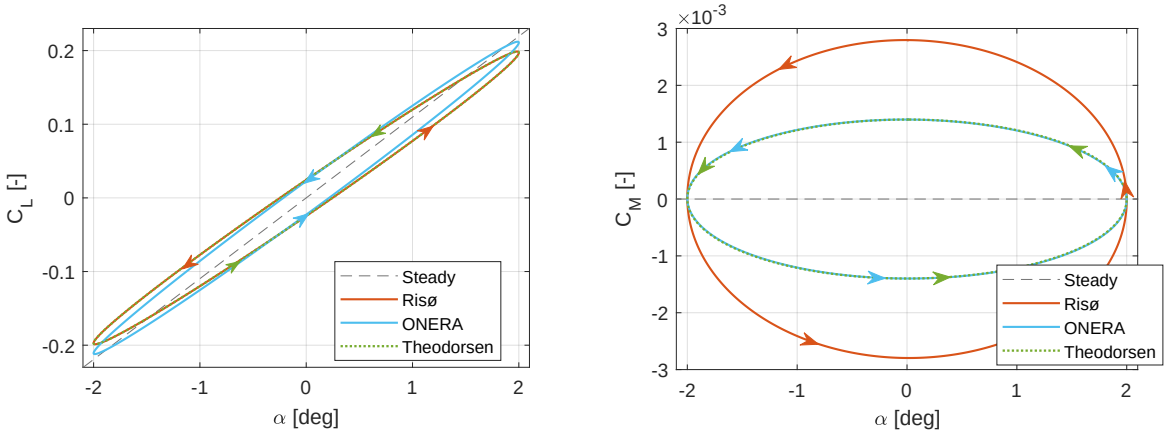

(a) C_L vs α (b) C_M vs α

Figure 3.2: Comparison between Theodorsen's function, the Risø and ONERA dynamic stall models where $k = 0.051$ and $\tilde{\tilde{h}} = 0.684$

The lift hysteresis loops are now slightly thicker due to the plunging motion generating a larger phase shift than the pitching motion. Again it is the Risø model that matches Theodorsen the best for the lift coefficient. The ONERA model still has roughly the right thickness, although is underrrotated with respect to the steady curve. This similarity with the pure pitching motion is partly due to the first added-mass term being equivalent between the two motions as $\alpha = \dot{h}/U$ in pure plunging for the small angles of attack used here. For the moment now only the ONERA model matches well, while the Risø model has too much hysteresis. This is due to the Risø model still using the pitching motion added-mass term in the C_M equation ($\pi T_u \dot{\alpha}/2$), while the first plunging added-mass term is half the size ($\pi T_u \dot{\alpha}/4$). The ONERA model correctly accounts for this difference by having added-mass contributions from both W_0' and W_1 and this could be relatively simply applied to the Risø added-mass terms too. This is not done here as the magnitudes of deviations seen for the moment are minimal.

3.2 Wagner

The second theoretical method used to verify the models is Wagner's function [34]. It is in effect the circulatory terms from Theodorsen's theory in the time domain and so assumes incompressible, attached flow. This function (approximated in Equation 3.8 [21]) gives the indicial response for the downwash, so the lift build up to the new steady value after a step

change in the angle of attack. The change is downwash is uniform over the chord, so can be seen as a sudden heaving motion.

$$\phi(s) = 1 - 0.165e^{-0.041s} - 0.335e^{-0.32s} \tag{3.8}$$

Where s is the non-dimensional time and ϕ can be used as

$$C_L^{dyn} = C_L^{st}\Big|_{\alpha_{old}} + \phi(s)\left(C_L^{st}\Big|_{\alpha_{new}} - C_L^{st}\Big|_{\alpha_{old}}\right) \tag{3.9}$$

The results for the two dynamic stall models with attached flow behaviour can be seen in Figure 3.3 for a 1° step in α (due to heaving) using a time step of $ds = \frac{2U}{c}dt = 0.2$ on a lift curve with a slope of 2π.

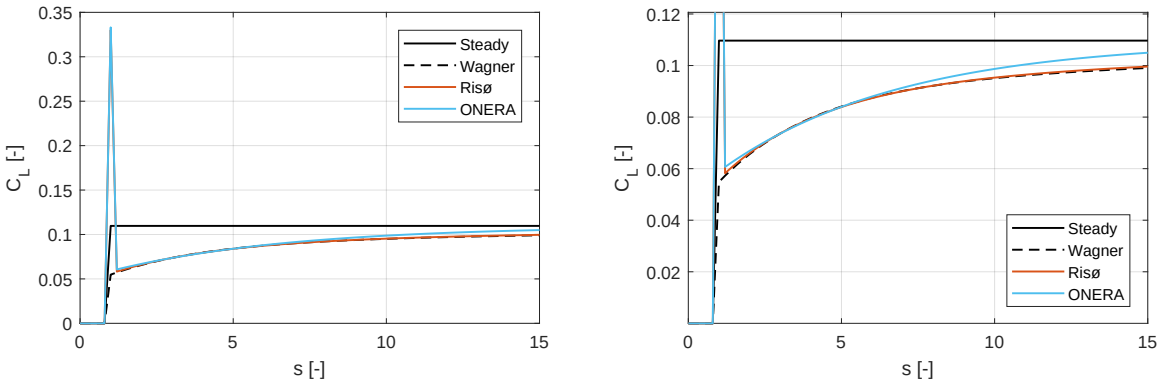

Figure 3.3: Comparison between the approximation of Wagner's function and the dynamic stall models with $ds = 0.2$

A large overshoot in the first time step is seen which is due to the presence of the added-mass terms in the dynamic stall models, while Wagner's function is circulatory terms only. At the next time step α' is back to zero again and then both models show almost identical behaviour to Wagner's function until $s \approx 7$ where the ONERA model starts to deviate. It is not expected that the ONERA model can completely match the theory as it only uses one ODE to simulate the circulatory effects, while there are two exponentials in the approximation of Wagner's theory in Equation 3.8.

The value of the overshoot depends on the size of the time step, so a second case is set up to analyse the dynamic stall models with a smooth angle of attack input. This input is chosen to have the shape of a hyperbolic tangent as seen in Figure 3.4. Here Equation 3.8 is applied to every increment of $2\pi\alpha$ individually.

Now the sharp spike from the added-mass term is smooth and both models follow the 'Wagner + $\pi\alpha'$' curve with the first added mass term from Theodorsen's theory[1]. The deviation of the ONERA model from the theory now occurs slightly later.

[1]It should be noted that Theodorsen's theory is for a sinusoidally oscillating airfoil and not a step

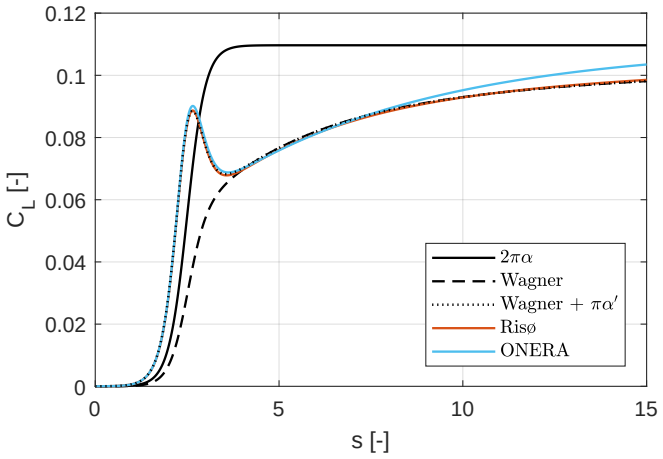

Figure 3.4: Comparison between the approximation of Wagner's function and the dynamic stall models using a hyperbolic tangent input

Next Figure 3.4 is repeated in Figure 3.5 with the difference that the models are subjected to a pitching motion about the quarter chord instead of a heaving motion. This does mean that the comparison to Wagner's theory is no longer valid. It does, however, highlight various differences between the models.

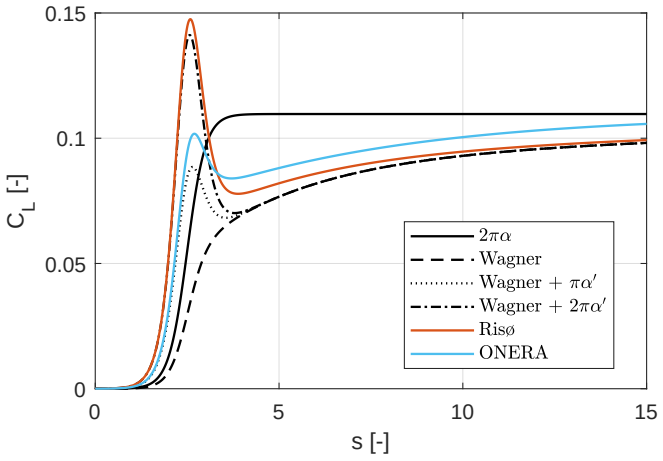

Figure 3.5: Comparison between the approximation of Wagner's function and the dynamic stall models using a hyperbolic tangent input

Now the Risø added-mass term is roughly double the size of that of the ONERA model. The Risø model has the $\pi\alpha'$ term as a direct contribution to the lift coefficient, while the ONERA models uses $2\pi\sin(\alpha)'$ in a pitching motion. However, the Risø model uses the angle of attack at three-quarter as the input for the effective angle of attack, while the ONERA model uses the angle of attack at the quarter chord. This means that if the ODE's gave the steady values, then the Risø model would output $2\pi\alpha + 3\pi\alpha'$ and the ONERA model $2\pi\alpha + 2\pi\alpha'$. It should be noted that the ONERA model has a $\pi\alpha'$ term in the forcing term for $C_{L,1}$ which helps bridge the gap between the models.

3.3 Experimental data

For the experimental data, wind tunnel measurement data from two different wind tunnels are used. Data from the University of Glasgow is used for the NACA0015 [33] and NACA0030 [35] airfoils, while data for the NACA4415 airfoil is used from NREL data measured at the Ohio State University, OSU [36]. These airfoils are chosen based on their thickness and relevance to wind turbines. It is important to note that measurements from this OSU database including measurements on the NACA4415 airfoil airfoil were used to tune Snel's model.

In terms of wind tunnel conditions the Reynolds number is chosen to be 1.5 million as this is the highest Reynolds number that is available across the board. The Mach number is generally between 0.1 and 0.12 for the Glasgow data and between 0.13 and 0.14 for the OSU data.
The Glasgow data is measured in the closed circuit Handley-Page wind tunnel at Glasgow University [33]. This wind tunnel has a 1.61 by 2.13 m working section and uses a model with a chord length of 0.55 m and span of 1.61 m. The forces and moment are measured using 30 pressure transducers on the airfoil surface and the angle of attack is measured using an angular displacement transducer on the main pitch axis. This measured angle of attack is used as feedback for the hydraulic pitching system. The wind speed was measured using a pitot tube 1.2 m in front of the leading edge.
The OSU wind tunnel OSU/AARL 3 x 5 [36] is, unlike the Handley-Page tunnel, is an open circuit tunnel and has a 1 x 1.41 m cross-section. The model chord length is 0.457 m with a span of 1 m. Again pressure transducers along the airfoil cross-section are used to measure the loading, although now with 60 sensors. To reduce the settling time before each pressure measurement the measurement unit is placed inside the airfoil to keep the tube lengths short. Similarly to the Glasgow measurements, the pressures along the surface are measured sequentially. The speed of the measurements is chosen so that the total angle travelled by the airfoil is less than 0.5° before a full sweep of the transducers is completed. The frequency of these sweeps is chosen so that 30 to 40 complete measurements are taken per cycle. The sinusoidal oscillations are obtained using a shaker system with an accuracy of 0.25°.
For both wind tunnels the model is pitched about the quarter chord and, as the measurement sets are obtained using pressure transducers, the drag coefficient contains the pressure drag contribution only (so no friction drag). This results in negative drag coefficients at very small angles of attack. Furthermore, it should be kept in mind when looking at the drag data that the drag coefficient is easily affected by a small error in the measured angle of attack. As the drag is much smaller than the lift, a small change in direction of the resultant force with affect the drag relatively more.
Both measurement sets use averaging where for the Glasgow data the unsteady cycles are averaged over 10 oscillations, while for the OSU data only 3 loops are used. Especially in reattachement there can be significant variations between cycles, which is lost when averaged [33]. The general trend is still captured.

The OSU wind tunnel has a larger airfoil chord to wind tunnel height ratio of 0.324 against 0.258 for the Handley-Page tunnel. This could result in more blockage effects especially at larger angles of attack. Furthermore, the wind tunnel corrections applied are a function of this airfoil chord to wind tunnel height ratio so the OSU wind tunnel will have larger correction factors. Unfortunately, there is no overlap in the airfoils analysed in each wind tunnel, so the wind tunnel results can not be compared directly.

For the models a sin wave input will be used instead of the angle of attack as measured during the measurement. This will give a discrepancy between the models and the data and, at the same phase, the model could see a different angle of attack than the data. The sin wave for the models is set up to fit that of the data as best a possible. The peak values are matched and the phase is then chosen to minimize the least squares error between the two angle of attack curves. Figure 3.6a shows the best match between the data and model inputs for the angle of attack, while the worst match is in Figure 3.6b.

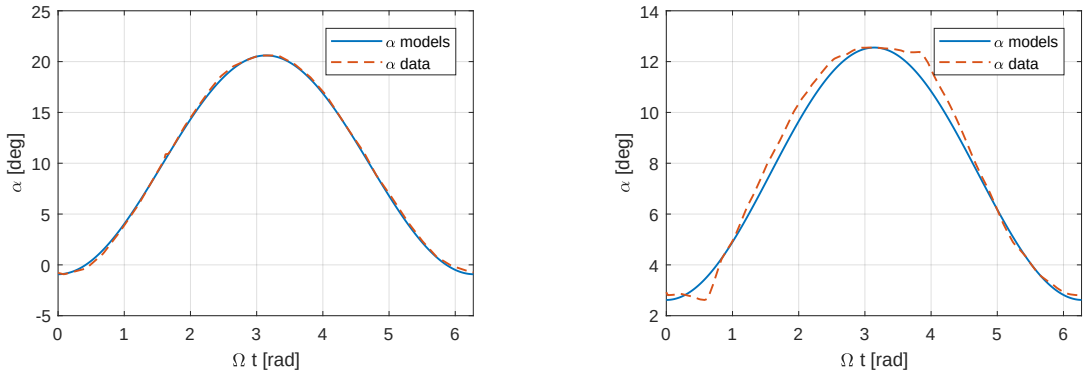

(a) NACA0030 for $k = 0.051$, $\alpha_m = 10$ and $\alpha_a = 10$ (b) NACA4415 for $k = 0.038$, $\alpha_m = 8$ and $\alpha_a = 5$

Figure 3.6: Comparison between the angle of attack input from the data and that used for the models for the best and worst fit

The discrepancy between the data α and the sinusoidal wave is significantly more than 0.25° indicating that the claim that the shaker system in the OSU wind tunnel can achieve this accuracy [36] may not always be realized.
The angle of attack from the data is not used for the models as it does not always match up at the start and end phase of the data. This results in discrete jumps in the angle of attack when running several rotations, which is required to remove the transients from the model behaviours.

CHAPTER 4

2D Comparison

For the comparison the cases are divided into different stall levels based on the amount of the hysteresis loop in stall: attached flow, light stall, moderate stall and deep stall which are in Sections 4.1, 4.2, 4.3 and 4.4 respectively. Here deep stall is used to indicate that the vast majority of the hysteresis loop is in stall. The k's are divided into three groups: low at around $k = 0.02$, medium at $k = 0.04$ and high at roughly $k = 0.06$. Additionally two more extreme cases with even larger k values are looked into in Section 4.5 and finally a ramp case is looked into in Section 4.6. In all plots and tables Snel's model is referred to as 'Snel (1st)' as the second order correction term has been neglected as explained in Section 2.5. Before the comparisons are made, the various parameters used to compare the models and data are listed:

- **l^2-norm**: This is the Euclidean norm of the difference between the model and the data, in a vector called v, over the whole loop normalized to the number of points in the loop, N. In equation form this is $l^2\text{-norm} = \sqrt{\frac{1}{N}\sum_{k=1}^{N} v_k^2}$. The l^2-norm is calculated for all three coefficients using the outputs from the models. As the models are used at a constant time step the edges of the C_L vs α plot where $\dot{\alpha}$ is small will be weighed more than the middle. When looking at a C_L vs Phase plot the weighting will be even along the x-axis.
- **Lift hyst.**: The lift hysteresis parameter gives an indication of the size of the hysteresis loop and so the severity of the unsteady effects. It is the lift in the upper part of the loop subtracted by that in the return part, $C_L^{Upper} - C_L^{Lower}$, at the angle of attack of the lift peak, $\alpha\Big|_{C_{L,max}}$
- $\boldsymbol{\Delta C_{L,max}}$: This parameters indicates how well the extreme load in the loop is predicted by the models compared to the data and is calculated using $C_{L,max}^{Model} - C_{L,max}^{Data}$
- $\boldsymbol{\Delta\alpha\Big|_{C_{L,max}}}$: This parameter gives an indication on if the drop is stall is predicted early or late as it is the difference between the angles of attack of the peaks of the lift hysteresis loops of the models and the data. The equation is: $\alpha^{Model}\Big|_{C_{L,max}^{Model}} - \alpha^{Data}\Big|_{C_{L,max}^{Data}}$
- $\boldsymbol{\zeta_P}$: The pitch damping parameter gives the work done over each cycle by the moment coefficient and so is an important parameter for stall flutter. If is calculated as the area within the hysteresis loop using Equation 4.1 [17].

$$\zeta_p = -\frac{1}{4\alpha_a^2}\oint C_M d\alpha \tag{4.1}$$

All models are solved using a time step such that there are 400 steps per rotation and two total loops are completed to remove any transients. The input sin wave angle of attack, $\alpha = \alpha_m + \alpha_a \sin(\omega t - \pi/2)$, for the models is adapted slightly from the mean, α_m, and the amplitude, α_a, mentioned in the captions. This is done to match the extreme angles of attack in the data.

The Reynolds numbers may differ slightly between the steady and unsteady data, although all measurements were conducted in the Reynolds number range of 1.48 to 1.53 million. Furthermore, in general experimental data has a lower accuracy in stall than when the flow is attached and this accuracy will be reduced further when the sinusoidal motions are included which increases the complexity of the set up and so introduces more error terms. Therefore, the experimental data used should not be seen as perfect. Finally it should be noted that only pure pitching motions are used here which does not give the complete picture of the model behaviour as would be seen on a full turbine.

4.1 Attached flow

For the attached flow the models that deviate from the steady coefficients have already been looked into in the Verification in Section 3.1 for the lift and moment figures. The drag coefficient is shown in Figure 4.2.

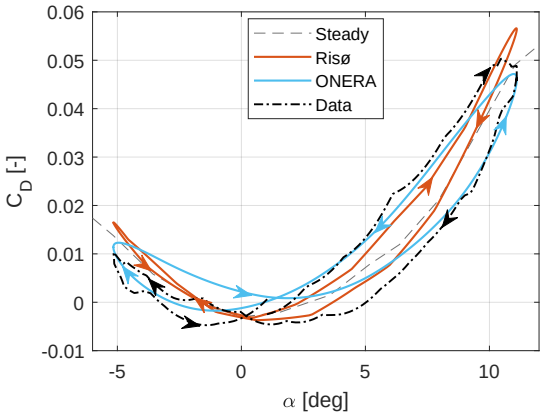

Figure 4.1: C_D vs α

Figure 4.2: Model responses for the NACA0015 airfoil where $k = 0.051$, $\alpha_m = 3°$ and $\alpha_a = 8°$

Here it is seen that the Risø model predicts the drag the best, although it does underpredict the thickness of the hysteresis loop. The ONERA model on the other hand gives rotation in the opposite direction which results in a decrease in accuracy with respect to the steady curve. It should be noted that the dynamic drag in the ONERA model is not well verified as stated in the original paper [23] and additionally is designed such that the equations have a similar form to the lift and moment equations. This may be a good choice for ease of use and tuning of the model; however, the dynamic lift and drag coefficients are significantly different from each other. The unsteady drag coefficient generally leads the steady forces (in the Risø model due to the $(\alpha - \alpha_E)C_L$ term), whereas the lift lags behind its steady value in the attached flow case due to the circulatory terms.
The l^2-norm of the drag is equal to 0.0061 for the steady curve, 0.0095 for the ONERA model and 0.0054 for the Risø model. So the ONERA model does indeed give a decrease in accuracy for the drag in this particular case.

4.2 Light stall

For light stall two identical cases are looked into using two different airfoils, the NACA0015 and the NACA0030, followed by a loop with a small α_a which should be more representative of what could be encountered in an operational turbine. A relatively high k value is used to obtain a sufficient level of deviation from the static curve to be able to compare the models. First the plots for the NACA0015 airfoil are shown in Figure 4.3.

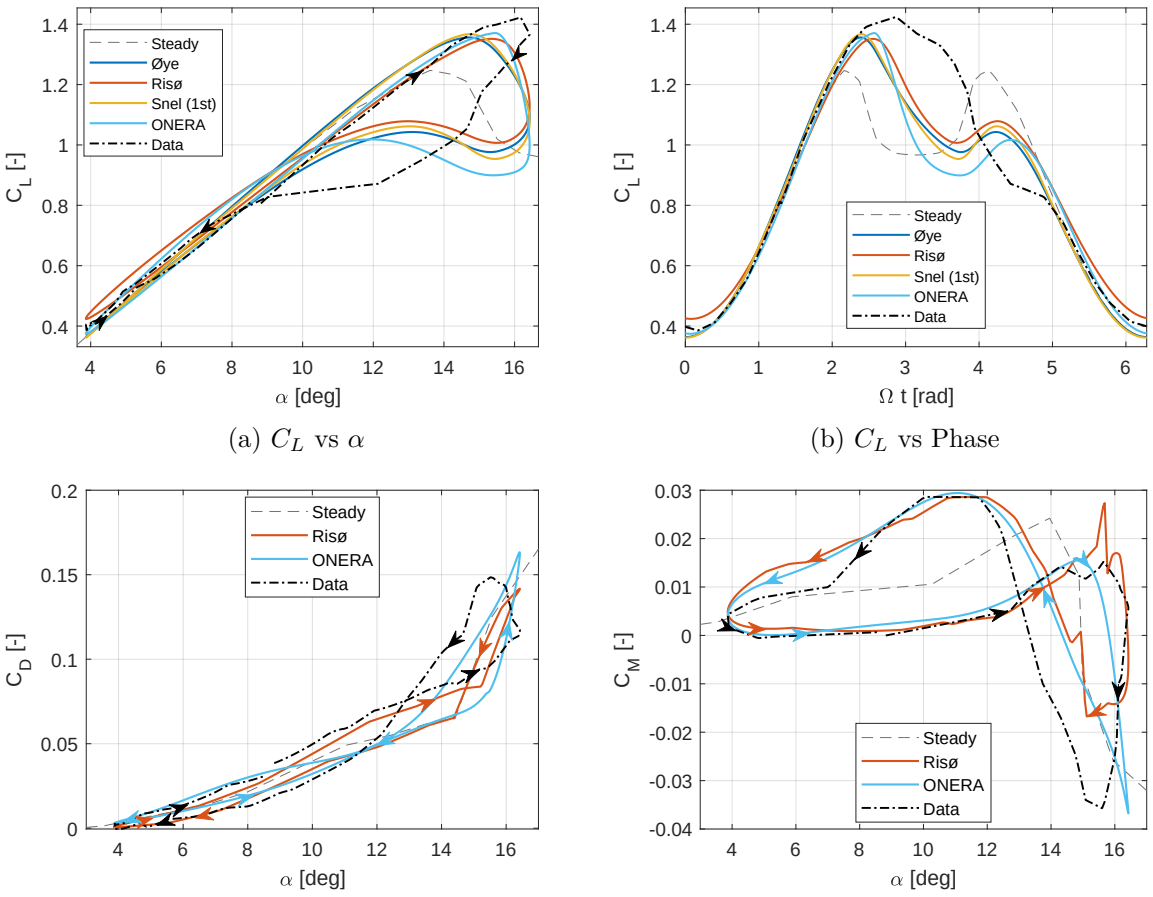

(a) C_L vs α

(b) C_L vs Phase

(c) C_D vs α

(d) C_M vs α

Figure 4.3: Model responses for the NACA0015 airfoil where $k = 0.051$, $\alpha_m = 10°$ and $\alpha_a = 6°$

When looking at the lift it can be seen that all models predict the drop in lift near the largest angle of attack when $\dot{\alpha}$ is small. This is in general the location when the lift drops in the other cases in this chapter. The case here is an exception in that the lift remains high even as the angle of attack starts to drop again and then the reattachment occurs much later than the models predict (seen best in the C_L vs Phase plot). The result is that the models not only quantitatively differ from the data, but also qualitatively. When looking at the statistics for the lift in Table 4.1 the Risø model has the lowest l^2-norm for the lift, Snel's model matches the peak lift value the best and both the ONERA and Risø models come the closest for $\Delta\alpha\big|_{C_{L,max}}$. The models with attached flow behaviour (Risø and ONERA) correctly show

figure-8 behaviour, although do overestimate the size of the attached flow loop. The ONERA model overpredicts the drop in lift at stall and so underpredicts the lift coefficient on the return loop which contributes to this model having the largest Euclidean norm. Overall there is no clear winner or loser when looking at the lift.
When looking at C_D only the Risø model captures the figure-8 shape. However, the ONERA model captures the C_D shape best after the static stall peak. In the end the Risø model has the lowest C_D Euclidean norm and additionally has the lowest l^2-norm for the moment coefficient. For C_M both models correctly capture the reverse loop in stall. The Risø model captures the area within the loop best as seen when comparing ζ_P while the ONERA model matches the extreme C_M values the best. Both models overpredict the pitch damping which is unconservative in the prediction of stall flutter. The roughness seen in the C_M loop for the Risø model is due to $C_M(\alpha_E)$ and the moment arm correction both reaching the drop in C_M^{st} due to stall at slightly different angles of attack. It is further exaggerated by the discreteness of the static moment and lift curves. Therefore, if more points had been used in these static curves, then the roughness of the dynamic C_M would be reduced.

Table 4.1: Results for the NACA0015 airfoil where $k = 0.051$, $\alpha_m = 10°$ and $\alpha_a = 6°$

	Unit	Øye	Risø	Snel (1st)	ONERA	Data
l^2-norm C_L	[-]	0.125	0.117	0.133	0.155	-
l^2-norm C_D	[-]	-	0.0154	-	0.0183	-
l^2-norm C_M	[-]	-	0.0083	-	0.0135	-
$\Delta C_{L,max}$	[-]	-0.068	-0.073	-0.057	-0.053	-
$\Delta\alpha\big\vert_{C_{L,max}}$	$[deg]$	-1.46°	-0.84°	-1.46°	-0.73°	-
ζ_P	$[1/rad]$	-	0.048	-	0.047	0.018

For the thicker airfoil, the NACA0030, significantly different characteristics are seen in Figure 4.4.

First, looking at C_L no figure-8 shape is seen due to the large airfoil thickness, very slow reattachment and gradual post stall drop-off in the static curve. This causes the Risø model in particular to have a larger error norm in Table 4.2 and the models without attached flow behaviour to have the lowest error norm. Although, Øye's and Snel's models are slightly outperformed by the other models in terms of α location of the peak.
Similarly to the attached flow case in Section 4.1, the ONERA model predicts the drag loop to be in the wrong direction. Overall the drag does not deviate much from the steady curve which the Risø model predicts better than the ONERA model. For the moment, the data from this thicker airfoil shows a significantly different shape with now no figure-8 present at all, despite the ONERA model still predicting one. The Risø model has the correct general shape which results in the best pitch damping parameter. However, when looking at the l^2-norm the improvement of the Risø model over the ONERA model is not much due to having an offset for a large part of the loop.

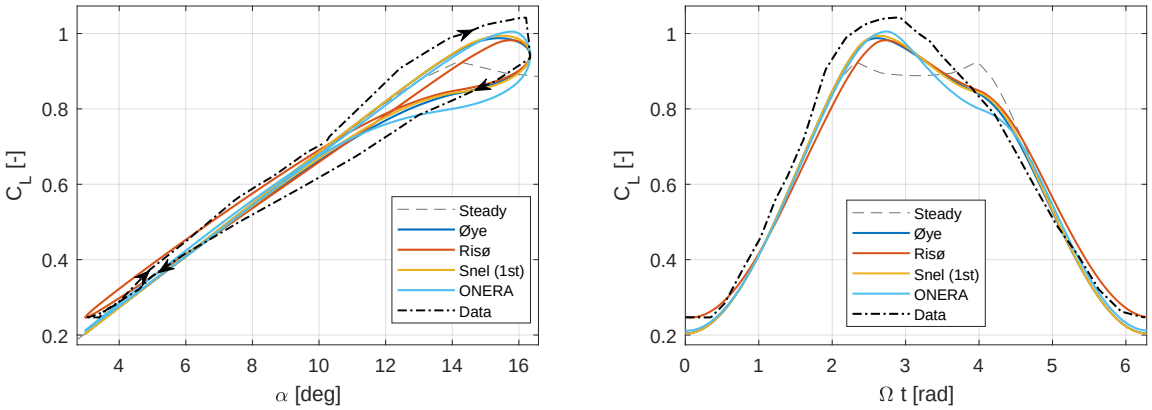

(a) C_L vs α

(b) C_L vs Phase

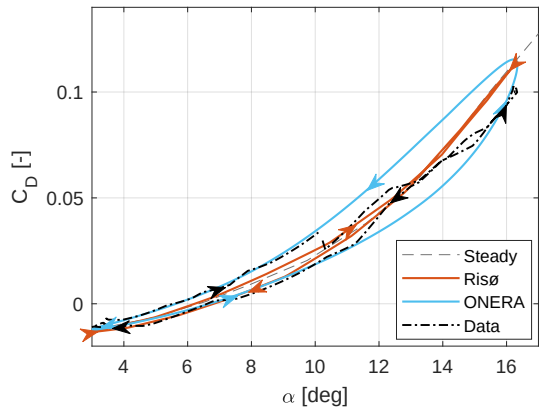

(c) C_D vs α

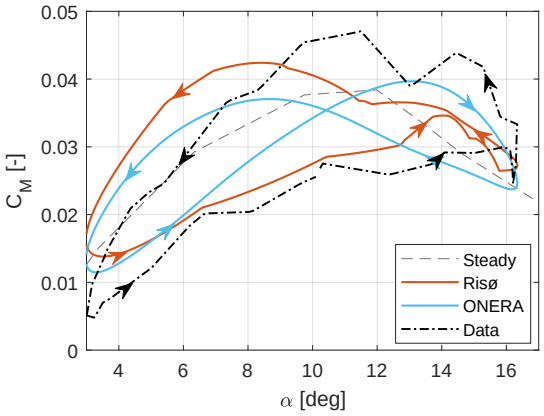

(d) C_M vs α

Figure 4.4: Model responses for the NACA0030 airfoil where $k = 0.051$, $\alpha_m = 10°$ and $\alpha_a = 6°$

Table 4.2: Results for the NACA0030 airfoil where $k = 0.051$, $\alpha_m = 10°$ and $\alpha_a = 6°$

	Unit	Øye	Risø	Snel (1st)	ONERA	Data
l^2-norm C_L	[-]	0.045	0.056	0.045	0.048	-
l^2-norm C_D	[-]	-	0.0058	-	0.0115	-
l^2-norm C_M	[-]	-	0.0058	-	0.0078	-
$\Delta C_{L,max}$	[-]	-0.055	-0.061	-0.049	-0.038	-
$\Delta\alpha\big\vert_{C_{L,max}}$	$[deg]$	-0.82°	-0.44°	-0.72°	-0.44°	-
ζ_P	$[1/rad]$	-	0.058	-	0.009	0.074

The next case is the most feasible α loop that could occur regularly in a turbine while in power production as it remains within the angles of attack before the lift drop off in stall and it has a relatively small α_a. The dynamic stall behaviour is still important here as it goes off the linear part of the lift curve indicating that the trailing edge stall has started. The responses for this case are in Figure 4.5. In some of the data for the NACA4415 airfoil a vertical offset upwards of the dynamic lift coefficient is seen to the static curve (e.g. in Figure 4.10). Therefore, it

may be the case that the dynamic C_L's are shifted up here too.

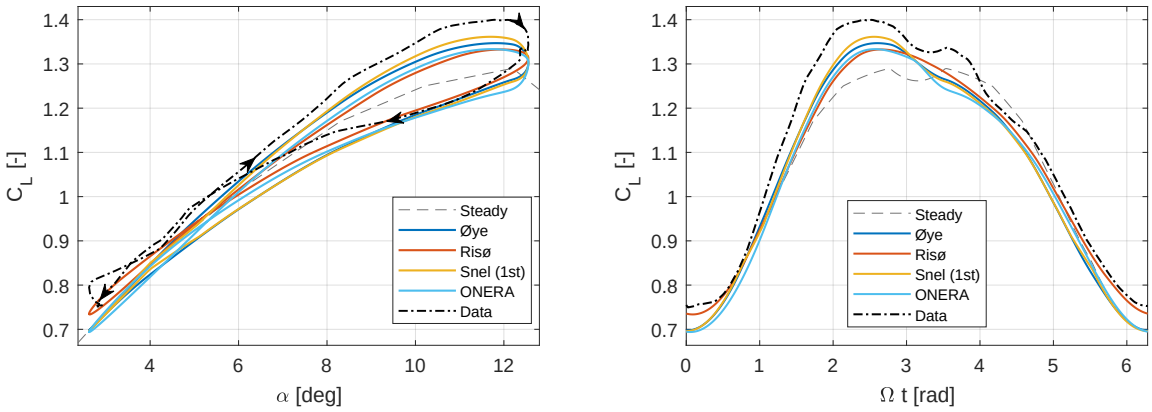

(a) C_L vs α

(b) C_L vs Phase

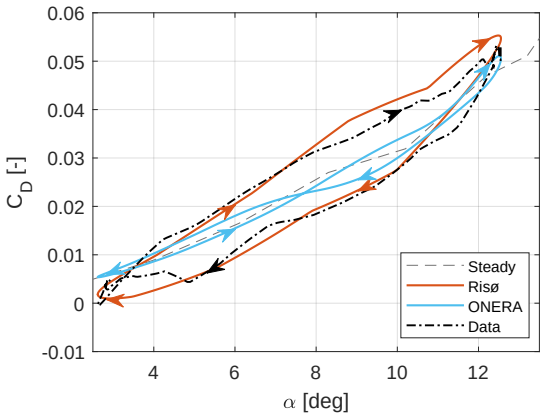

(c) C_D vs α

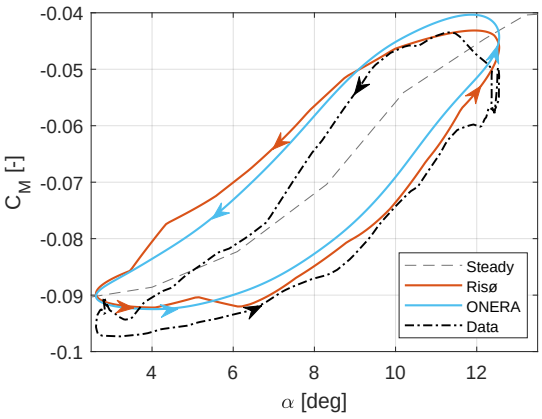

(d) C_M vs α

Figure 4.5: Model responses for the NACA4415 airfoil where $k = 0.037$, $\alpha_m = 8°$ and $\alpha_a = 5°$

The Risø model has the best Euclidean norm for the lift, although this is mainly due to the attached flow behaviour as it also has the worst Lift Hyst., $\Delta C_{L,max}$ and $\Delta\alpha\big|_{C_{L,max}}$. Closest to stall, so at the highest α's, it is Snel's model which performs the best followed by Øye's model.
For the drag it is again the Risø model which clearly outperforms the ONERA model with the ONERA model showing a Figure-8 shape not seen in the data. For the moment, on the other hand, the ONERA model slightly outperforms the Risø model.

Table 4.3: Results for the NACA4415 airfoil where $k = 0.037$, $\alpha_m = 8°$ and $\alpha_a = 5°$

	Unit	Øye	Risø	Snel (1st)	ONERA	Data
l^2-norm C_L	[-]	0.055	0.053	0.054	0.063	-
l^2-norm C_D	[-]	-	0.0030	-	0.0058	-
l^2-norm C_M	[-]	-	0.0062	-	0.0060	-
Lift hyst.	[-]	0.095	0.064	0.119	0.104	0.134
$\Delta C_{L,max}$	[-]	-0.053	-0.067	-0.038	-0.066	-
$\Delta\alpha\big\vert_{C_{L,max}}$	$[deg]$	0.03°	0.19°	-0.08°	-0.08°	-
ζ_P	$[1/rad]$	-	0.110	-	0.095	0.090

4.3 Moderate stall

Moving deeper into stall the size of the unsteady effects becomes larger. In this section the models are compared in four different cases starting with a repetition of the two cases in the previous section (Section 4.2), although now with an increased value of 10° for α_a. These can be found in Figures 4.6 and 4.7 for the NACA0015 and NACA0030 airfoils respectively. This is followed by a roughly similar loop for the cambered NACA4415 airfoil in Figure 4.8 and then finally a loop with a low reduced frequency is looked into in Figure 4.9 for the NACA4415 airfoil.

When comparing the shape of the experimental data between Figures 4.3 and 4.6 for the NACA0015 a large difference is seen in shape of the hysteresis loop. In the case with the larger α_a the drop in lift is significantly more sudden which is seen best in the C_L vs Phase plots. This indicates the occurrence of leading edge stall and the shedding of a leading edge vortex. As the leading passes over the airfoil it results in a sharp spike away from the static curve for both the drag and moment coefficients. The only model that shows such a large and sudden drop in lift is the ONERA model; however, it predicts this drop too early. This could be fixed in this model relatively easily by increasing the value of the stall delay $\Delta\tau$. The ONERA model is additionally the most accurate on the reattachment part of the loop, matches the figure-8 shape the best and comes the closest to matching the peak value and location. Despite this, it still has the largest C_L l^2-norm in Table 4.4 due to the sharp drop in lift after predicting the stall too early. This results in a large lift discrepancy between the model and data until stall also occurs in the data. Extra attention should be paid to the magnitude of the l^2-norm, the lift hysteresis and $\Delta\alpha\big\vert_{C_{L,max}}$ which all indicate that no models managed to match the experimental results too well. They do all give a significant improvement over the steady curve though.
For the drag both models perform similarly for the l^2-norms, although the ONERA model does again predict the hysteresis loop to have the wrong direction when the flow is attached. The moment loop now has two crossovers and so three different enclosed areas. The ONERA model successfully predicts the presence of these two crossings. Furthermore, it has the closest C_M value during the spike down due to the passing of the leading edge vortex over the airfoil in the data. These good visual properties of the ONERA model translate into the best Euclidean norm and it additionally matches ζ_P the best.

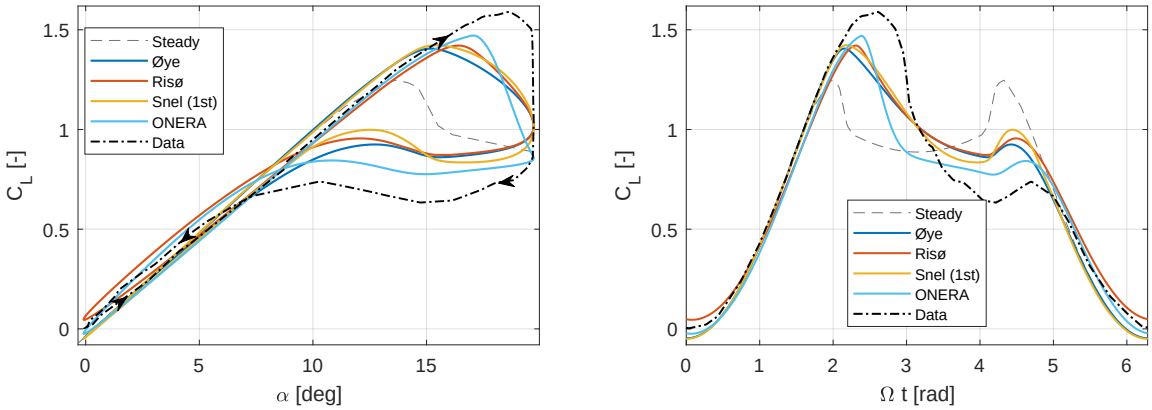

(a) C_L vs α

(b) C_L vs Phase

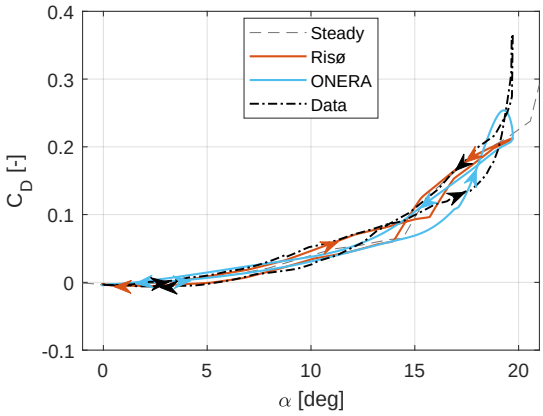

(c) C_D vs α

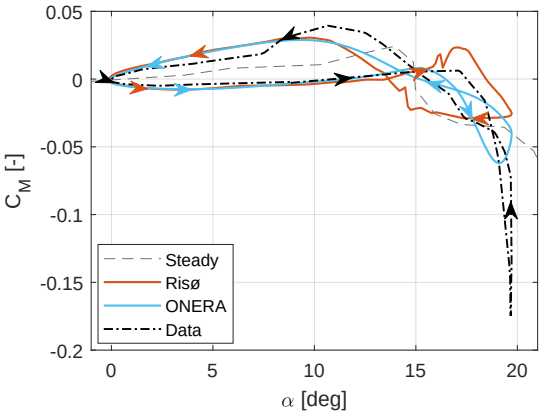

(d) C_M vs α

Figure 4.6: Model responses for the NACA0015 airfoil where $k = 0.051$, $\alpha_m = 10°$ and $\alpha_a = 10°$

Table 4.4: Results for the NACA0015 airfoil where $k = 0.051$, $\alpha_m = 10°$ and $\alpha_a = 10°$

	Unit	Øye	Risø	Snel (1st)	ONERA	Data
l^2-norm C_L	[-]	0.145	0.146	0.141	0.147	-
l^2-norm C_D	[-]	-	0.0408	-	0.0389	-
l^2-norm C_M	[-]	-	0.0376	-	0.0286	-
Lift hyst.	[-]	0.542	0.545	0.571	0.676	0.846
$\Delta C_{L,max}$	[-]	-0.183	-0.168	-0.167	-0.119	-
$\Delta\alpha\big\vert_{C_{L,max}}$	$[deg]$	-3.45°	-2.22°	-3.32°	-1.66°	-
ζ_P	$[1/rad]$	-	0.022	-	0.053	0.043

Next the same comparison is conducted for the NACA0030 airfoil between Figures 4.4 and 4.7 for $\alpha_a = 6°$ and $\alpha_a = 10°$ respectively.

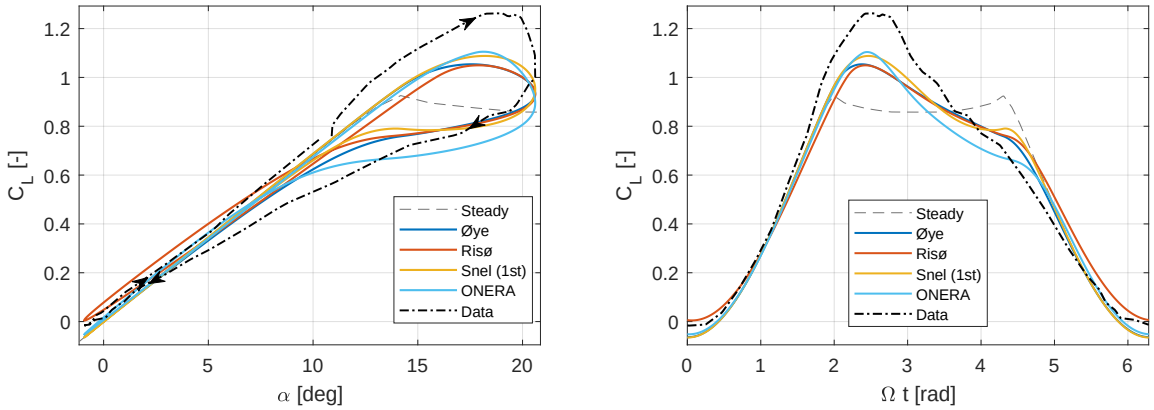

(a) C_L vs α

(b) C_L vs Phase

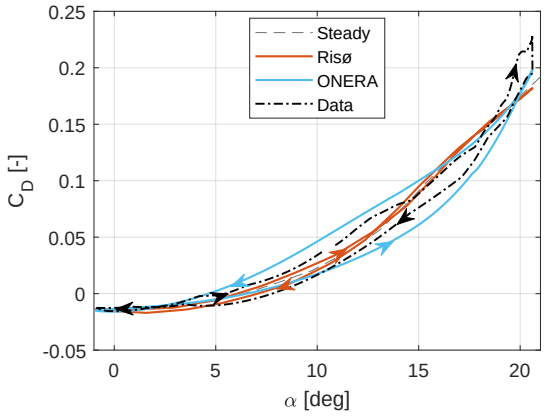

(c) C_D vs α

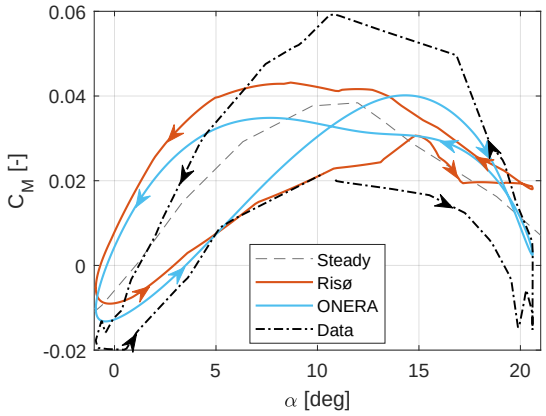

(d) C_M vs α

Figure 4.7: Model responses for the NACA0030 airfoil where $k = 0.051$, $\alpha_m = 10°$ and $\alpha_a = 10°$

For this thicker airfoil the shape of the dynamic curves for all the coefficients is roughly the same as in Figure 4.4 indicating that the stall type has not changed from the light stall case and is still trailing edge stall. The discrepancy of the peak value of the lift between the data and models is seen to be quite significant in Table 4.5 at around 0.16 for the Snel and ONERA models and even above 0.2 for the other two models. With the larger amplitude the loops are thicker which is most notable in the ONERA model. The ONERA model also shows improvement in the moment coefficient for the larger α_a as now the reverse loop is smaller. The hysteresis loop for the drag is still in the counter-clockwise direction, opposite to the data, though.

Table 4.5: Results for the NACA0030 airfoil where $k = 0.051$, $\alpha_m = 10°$ and $\alpha_a = 10°$

	Unit	Øye	Risø	Snel (1st)	ONERA	Data
l^2-norm C_L	[-]	0.094	0.109	0.088	0.095	-
l^2-norm C_D	[-]	-	0.0145	-	0.0195	-
l^2-norm C_M	[-]	-	0.0144	-	0.0147	-
$\Delta C_{L,max}$	[-]	-0.209	-0.213	-0.174	-0.158	-
$\Delta\alpha\|_{C_{L,max}}$	$[deg]$	-1.29°	-0.94°	-0.61°	-0.72°	-
ζ_P	$[1/rad]$	-	0.056	-	0.023	0.087

The cambered airfoil is used in a similar case as the two previous cases in this section for which the results can be found in Figure 4.8 and Table 4.6. As mentioned in Section 3.3 Snel's model was tuned using data from the same measurement series as the data for the NACA4415 airfoil, so it should have an advantage.

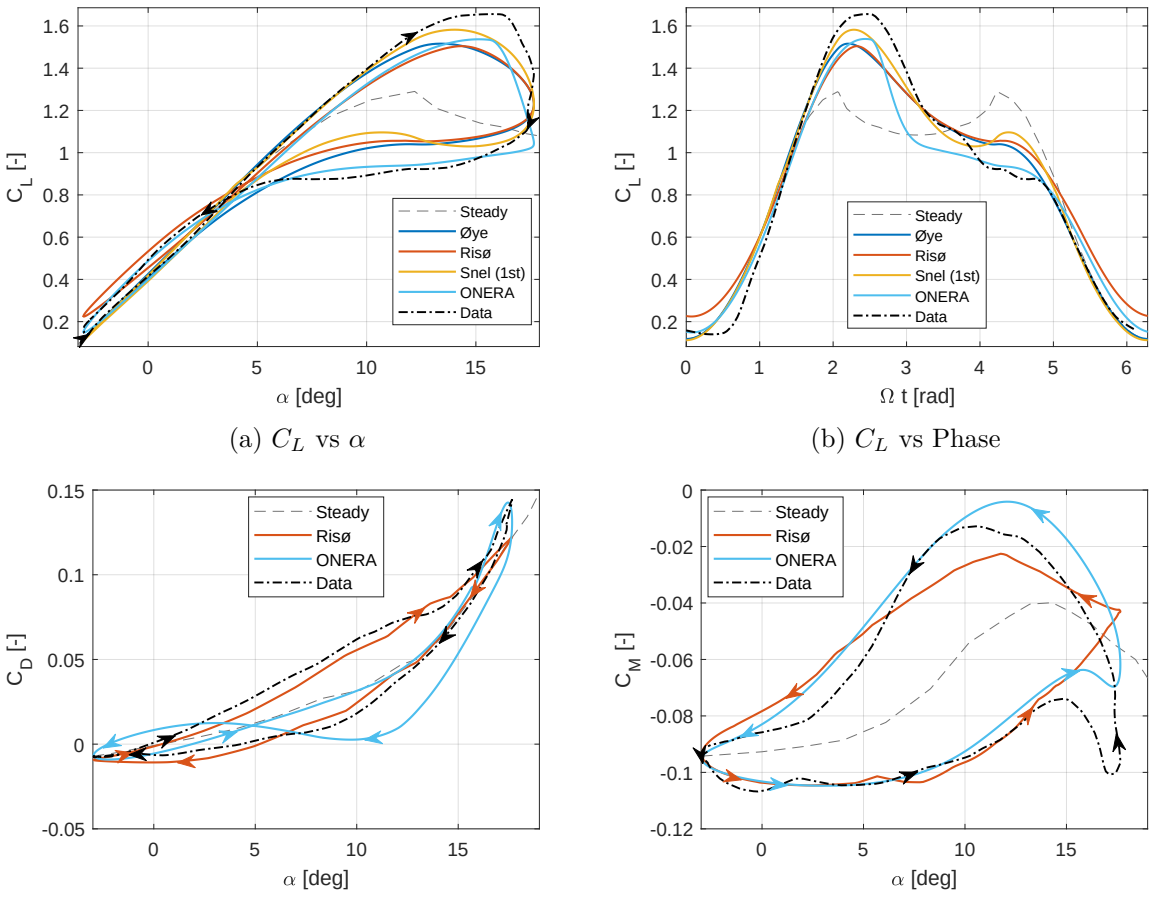

(a) C_L vs α

(b) C_L vs Phase

(c) C_D vs α

(d) C_M vs α

Figure 4.8: Model responses for the NACA4415 airfoil where $k = 0.056$, $\alpha_m = 8°$ and $\alpha_a = 10°$

When looking at the lift coefficient the general shape of the results is surprisingly similar to that of the uncambered NACA0015 airfoil in Figure 4.6 with the differences that stall is slightly

more gradual and that there are no sharp spikes in C_D or C_M. This indicates that the leading edge vortex is less pronounced. The moment coefficient does still show a little tail at the higher angles of attack indicating that there may still be a smaller leading edge vortex being shed. In that case the stall mode is likely a combination of leading edge and trailing edge. When looking at the statistics in Table 4.6 it is seen that the ONERA model captures the location of the peak the best, but it is Snel's model that has the best lift l^2-norm, lift hysteresis and peak lift value.
The drag and moment hysteresis loops do show significant differences from the symmetrical airfoil. The C_D loop is thicker which both models manage to capture. However, the ONERA model's C_D is slightly offset and it additionally falsely predicts a figure-8 shape at low angles of attack. This gives it an l^2-norm that is double that of the Risø model. For the moment coefficient it is the ONERA model that outperforms the Risø model and even manages to slightly capture the tail at high angles of attack. It does slightly overpredict the pitch damping parameter though.

Table 4.6: Results for the NACA4415 airfoil where $k = 0.056$, $\alpha_m = 8°$ and $\alpha_a = 10°$

	Unit	Øye	Risø	Snel (1st)	ONERA	Data
l^2-norm C_L	[-]	0.087	0.113	0.082	0.104	-
l^2-norm C_D	[-]	-	0.0086	-	0.0187	-
l^2-norm C_M	[-]	-	0.0191	-	0.0154	-
Lift hyst.	[-]	0.473	0.439	0.549	0.561	0.655
$\Delta C_{L,max}$	[-]	-0.140	-0.152	-0.074	-0.118	-
$\Delta\alpha\big\vert_{C_{L,max}}$	$[deg]$	-2.33°	-1.33°	-1.69°	-0.54°	-
ζ_P	$[1/rad]$	-	0.127	-	0.147	0.135

Next a case with a low reduced frequency is looked into in Figure 4.9. This frequency is representative of 1P oscillations in angle of attack, so due to for example yaw and shear, for the outerboard parts of the blade where the majority of the power and thrust are produced. Although, the large α_a is less representative of normal turbine operation.

When comparing this case to the previous case in Figure 4.8 which uses the same airfoil, α_a and α_m the same general trends are visible where the peak value of the lift and the lift hysteresis parameter are underestimated and the drop in lift is predicted too early. Again different models perform the best for each of the coefficients when looking at the Euclidean norms with Snel's model best for C_L, Risø for C_D and ONERA for C_M. Here the offset in drag coefficient for the ONERA model is smaller and for the moment the Risø model shows some improvement relative to the ONERA model despite predicting an small figure-8 shape at the highest angles of attack.

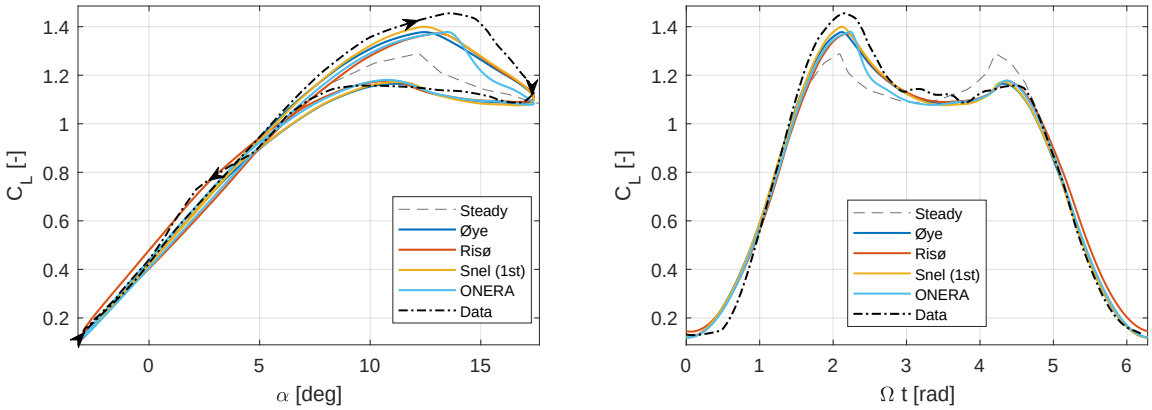

(a) C_L vs α

(b) C_L vs Phase

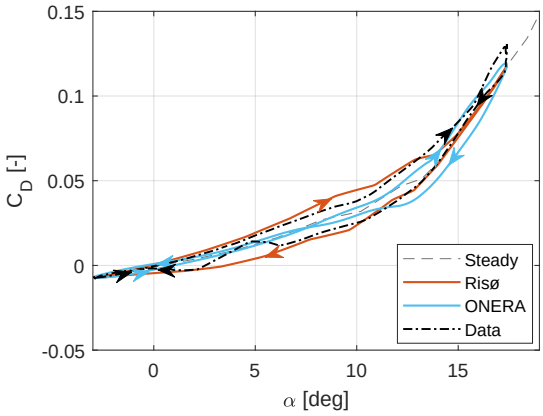

(c) C_D vs α

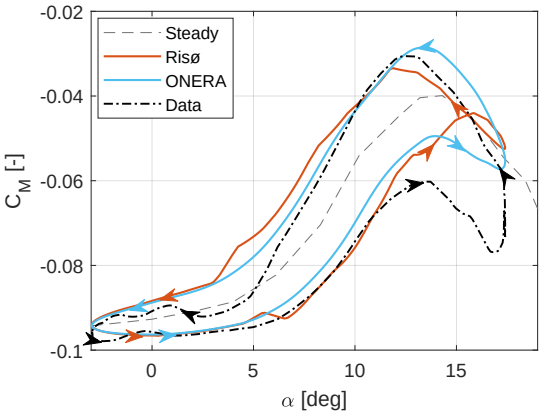

(d) C_M vs α

Figure 4.9: Model responses for the NACA4415 airfoil where $k = 0.019$, $\alpha_m = 8°$ and $\alpha_a = 10°$

Table 4.7: Results for the NACA4415 airfoil where $k = 0.019$, $\alpha_m = 8°$ and $\alpha_a = 10°$

	Unit	Øye	Risø	Snel (1st)	ONERA	Data
l^2-norm C_L	[-]	0.045	0.054	0.041	0.051	-
l^2-norm C_D	[-]	-	0.0092	-	0.0109	-
l^2-norm C_M	[-]	-	0.0107	-	0.0092	-
Lift hyst.	[-]	0.242	0.252	0.260	0.266	0.318
$\Delta C_{L,max}$	[-]	-0.077	-0.083	-0.055	-0.076	-
$\Delta\alpha\big\vert_{C_{L,max}}$	$[deg]$	-1.07°	-0.53°	-1.07°	-0.14°	-

4.4 Deep stall

Moving even further into stall first another low k is used to compare the models which is then followed by two middle reduced frequency cases. The first of which has a large α_a in Figure 4.11 and the second a small α_a in Figure 4.12. Starting with the low k case in Figure 4.10.

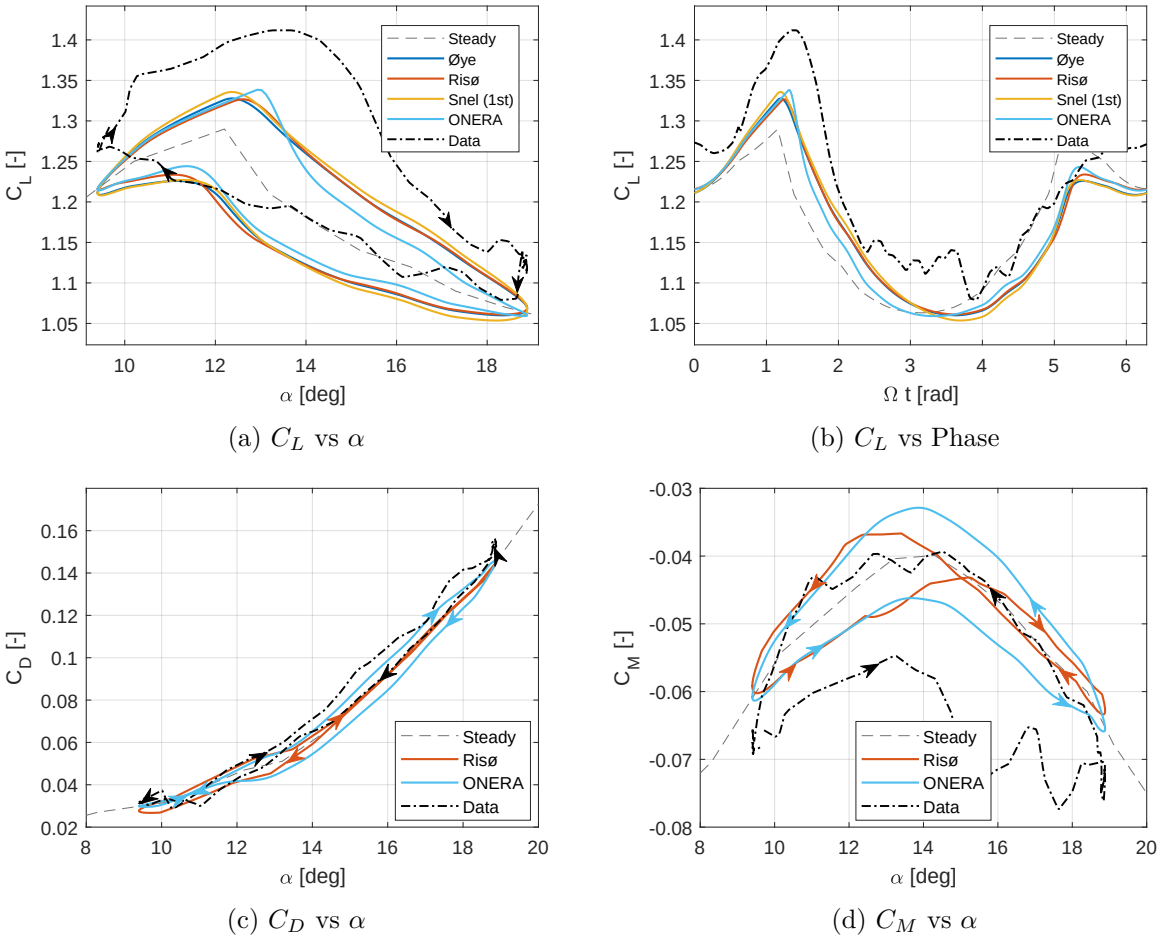

(a) C_L vs α

(b) C_L vs Phase

(c) C_D vs α

(d) C_M vs α

Figure 4.10: Model responses for the NACA4415 airfoil where $k = 0.019$, $\alpha_m = 14°$ and $\alpha_a = 5°$

The data has an offset in particular for the lift and moment coefficients so the Euclidean norms are ignored. The general shape and size of the loop can still be compared using the Lift Hyst and ζ_P in Table 4.8. For the lift the ONERA model has the closest lift hysteresis parameter to the data. However, after the drop in lift the remaining part of the tail is too thin which has been found to be a consistent negative characteristic of the ONERA model over most of the cases. It is in particular notable in this case as stall occurs early in the hysteresis loop leaving a large portion of the phase where lift is too low.
When looking at the drag, it is the ONERA model that roughly has the correct thickness and it additionally captures the shape of the moment hysteresis loop the best. The Risø model erroneously predicts a figure-8 shape in C_M and therefore greatly underestimates the pitch damping.
This case is additionally interesting due to the presence of higher frequency oscillations within the measured $k = 0.019$ loop despite the data being averaged over 10 cycles. This is likely due to the static case containing a large amount of unsteadiness and vortex shedding due to the large degree of stall. That these higher frequency oscillations are so visible despite the averaging could suggest that there is a level of repetition is these vortices being shed. If this is

the case then the dynamic stall cycle could be having a effect on when these vortices are shed.

Table 4.8: Results for the NACA4415 airfoil where $k = 0.019$, $\alpha_m = 14°$ and $\alpha_a = 5°$

	Unit	Øye	Risø	Snel (1st)	ONERA	Data
Lift hyst.	[-]	0.140	0.159	0.143	0.174	0.218
ζ_P	$[1/rad]$	-	0.021	-	0.056	0.088

Next a higher reduced frequency case is used where there is a significantly larger amount of hysteresis as seen in Figure 4.11.

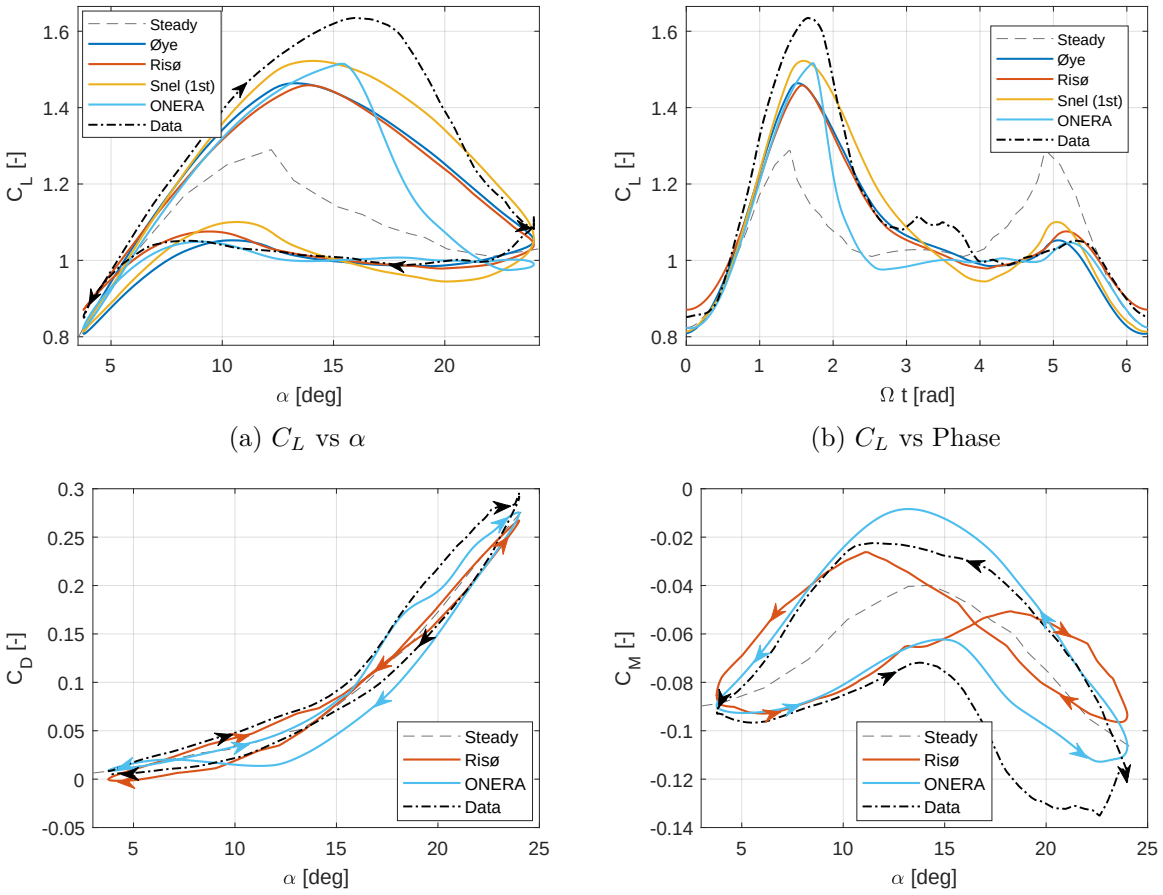

(a) C_L vs α

(b) C_L vs Phase

(c) C_D vs α

(d) C_M vs α

Figure 4.11: Model responses for the NACA4415 airfoil where $k = 0.039$, $\alpha_m = 14°$ and $\alpha_a = 10°$

Again the level of lift hysteresis is underestimated and the ONERA model predicts stall too early and then drops below the steady lift value with even a small reverse loop at the highest angles of attack. This small reverse loop is seen as unphysical and poor model behaviour. As mentioned before it is possible to fix this through tuning the stall delay in non-dimensional time. Overall Snel's model matches the data the best for the lift and has the lowest Euclidean

norm in Table 4.9.
For the drag it is the Risø model this time that shows rotation in the wrong direction at high angles of attack. For the dynamic C_M, similarly to the $k = 0.019$ case, the Risø model predicts a significant figure-8 shape, which does not occur in the measurement. So unsurprisingly the ONERA model has the lowest l^2-norm for both these coefficients.

Table 4.9: Results for the NACA4415 airfoil where $k = 0.039$, $\alpha_m = 14°$ and $\alpha_a = 10°$

	Unit	Øye	Risø	Snel (1st)	ONERA	Data
l^2-norm C_L	[-]	0.073	0.076	0.064	0.099	-
l^2-norm C_D	[-]	-	0.0316	-	0.0285	-
l^2-norm C_M	[-]	-	0.0299	-	0.0170	-
Lift hyst.	[-]	0.450	0.446	0.504	0.518	0.631
$\Delta C_{L,max}$	[-]	-0.171	-0.177	-0.112	-0.119	-
$\Delta\alpha\big\vert_{C_{L,max}}$	$[deg]$	-2.77°	-2.13°	-1.81°	-0.54°	-
ζ_P	$[1/rad]$	-	0.041	-	0.123	0.142

The last deep stall case is a loop with a smaller α_a and a high α_m that remains well away from the attached flow part of the lift curve. It can be found in Figure 4.12. This case is pushing the boundaries of the design range of the models; however, is relevant for the model behaviour in some of the standstill cases to be analysed in Chapter 5.

Looking at the lift coefficient shows that this data for the NACA4415 airfoil is shifted up again. Ignoring this offset and simply looking at the loop thickness at the mean angle of attack, 19°, it is seen that the Risø and Øye models get the closest to the data, while Snel's model overpredicts the loop thickness and the ONERA model greatly underestimates the thickness. The ONERA model even predicts a figure-8 shape at the highest α's.
The Risø model does not fair well for the drag and moment coefficients with both rotating in the wrong direction. This results in the Risø model having the highest l^2-norm for the drag in Table 4.10. Furthermore, this causes the pitch damping parameter to be negative for the Risø model. That the Risø model predicts a clockwise C_M loop is due to the moment arm correction term indicating that this term may not be accurate in deep stall. Without this moment arm term the Risø model would roughly follow the static curve which would be an improvement.

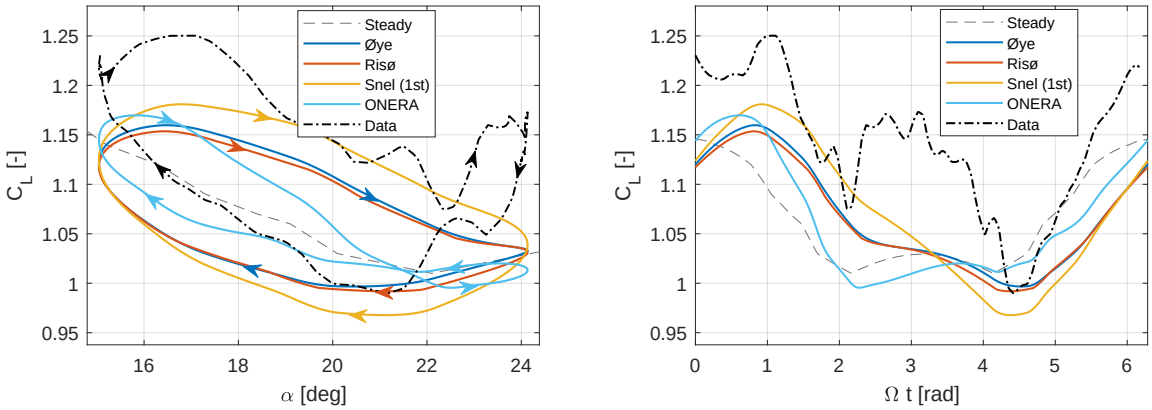

(a) C_L vs α (b) C_L vs Phase

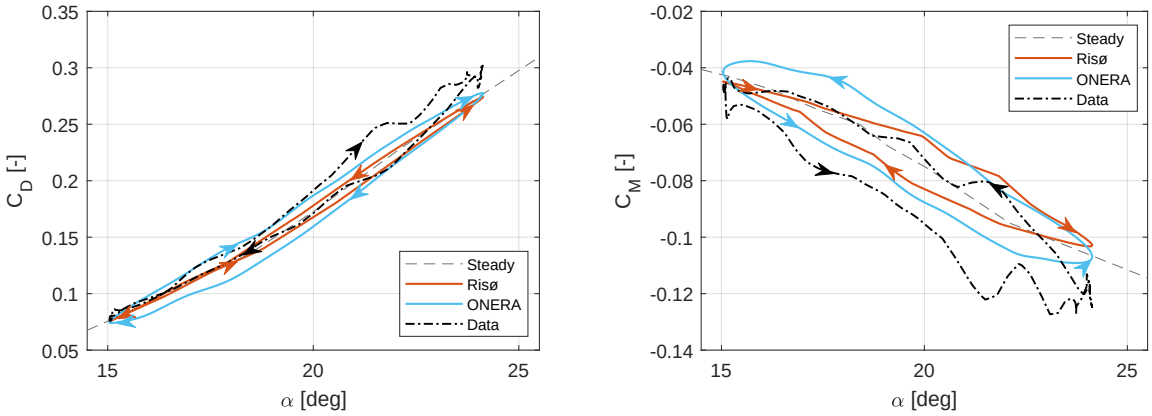

(c) C_D vs α (d) C_M vs α

Figure 4.12: Model responses for the NACA4415 airfoil where $k = 0.037$, $\alpha_m = 20°$ and $\alpha_a = 5°$

Table 4.10: Results for the NACA4415 airfoil where $k = 0.037$, $\alpha_m = 20°$ and $\alpha_a = 5°$

	Unit	Øye	Risø	Snel (1st)	ONERA	Data
l^2-norm C_D	[-]	-	0.0218	-	0.0185	-
ζ_P	$[1/rad]$	-	-0.051	-	0.099	0.103

4.5 High reduced frequencies

To push the boundaries of what the models are capable of two cases with higher reduced frequencies are looked into. These k's are too high to be from 1P excitations, although may be possible in instability or resonance cases. It should be noted that as the amplitude of the pitching oscillation is 10° in either direction this represents an incredibly violent instability such that a turbine will likely already have failed before it encounters this in normal operation. In

an simulation environment, however, it could potentially be encountered in the design process.

The first case has $k = 0.102$ for the NACA0015 airfoil in Figure 4.13. The measurement data shows a spike to a C_L value of above 2 followed by a sharp drop at the maximum lift which indicates the presence of leading edge stall followed by a leading edge vortex traveling over the airfoil. The drag and moment coefficients additionally show a spike at the highest angle of attack which corresponds to this leading edge vortex traveling over the airfoil and causing a rapid change in the location of the center of pressure. For the lift coefficient the ONERA model best captures the C_L peak, the sharp drop and the late reattachment. Looking at Figure 4.13b it is seen that the ONERA does predict the drop-off significantly too early. Both the Øye and Risø models predict the peak in lift coefficient over 5° to early (as seen in Table 4.11) and furthermore underestimate the magnitude of the C_L peak by over 0.6. For the drag neither model performs stellar, although they do both correctly predict a figure-8 shape. For the moment the ONERA model does not manage to capture the figure-8 shape at all which results in it incorrectly predicting an aerodynamically damped pitching motion.

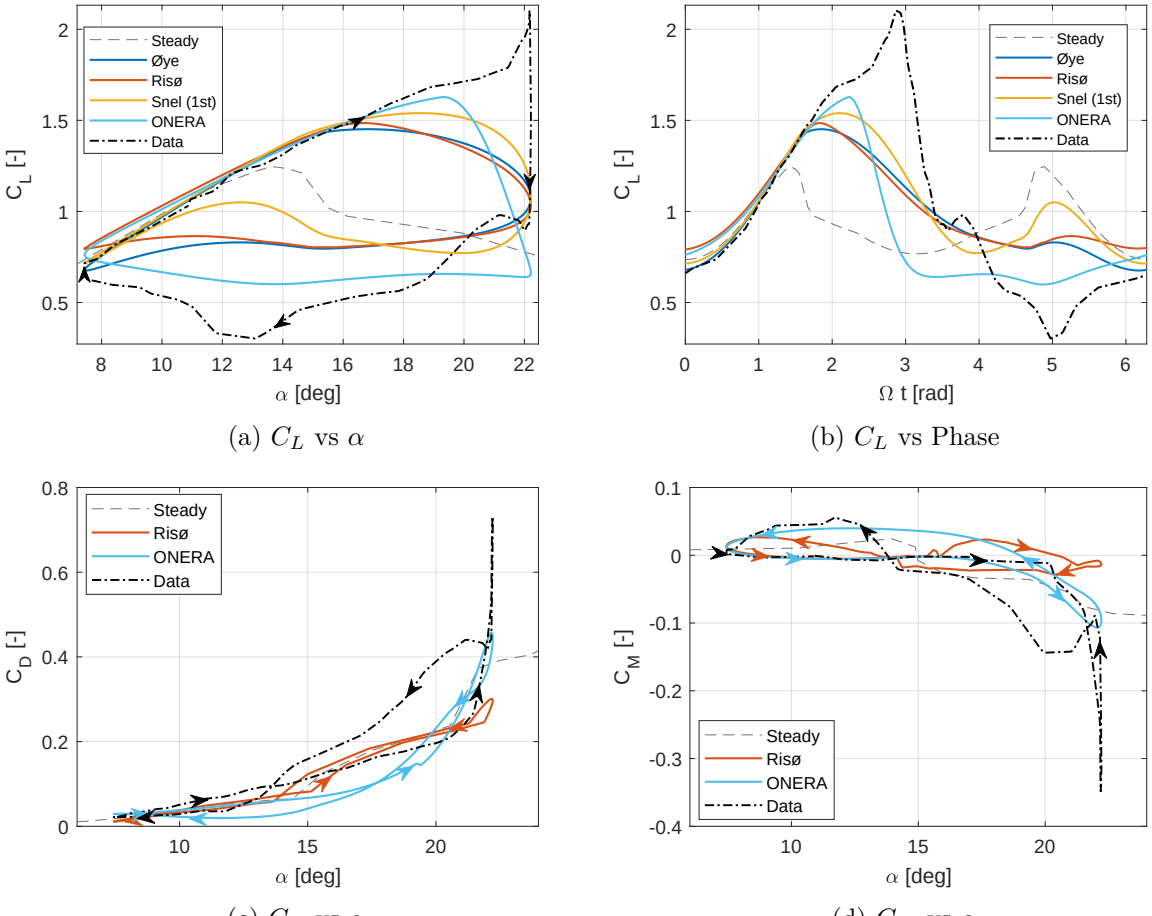

(a) C_L vs α

(b) C_L vs Phase

(c) C_D vs α

(d) C_M vs α

Figure 4.13: Model responses for the NACA0015 airfoil where $k = 0.102$, $\alpha_m = 15°$ and $\alpha_a = 8°$

Table 4.11: Results for the NACA0015 airfoil where $k = 0.102$, $\alpha_m = 15°$ and $\alpha_a = 8°$

	Unit	Øye	Risø	Snel (1st)	ONERA	Data
l^2-norm C_L	[-]	0.305	0.331	0.321	0.372	-
l^2-norm C_D	[-]	-	0.1333	-	0.1010	-
l^2-norm C_M	[-]	-	0.0985	-	0.0728	-
$\Delta C_{L,max}$	[-]	-0.651	-0.617	-0.562	-0.474	-
$\Delta\alpha\big\vert_{C_{L,max}}$	$[deg]$	-5.32°	-5.43°	-3.62°	-2.84°	-
ζ_P	$[1/rad]$	-	-0.022	-	0.113	-0.029

For an even higher k of 0.153 in Figure 4.14 all models except the ONERA model show significantly different behaviour from the measurements. As the ONERA model is the only model designed for helicopters it is not surprising that this model is superior for the larger k's. For the drag and moment coefficients, however, it is the ONERA model that shows different hysteresis loop shapes as in the data.

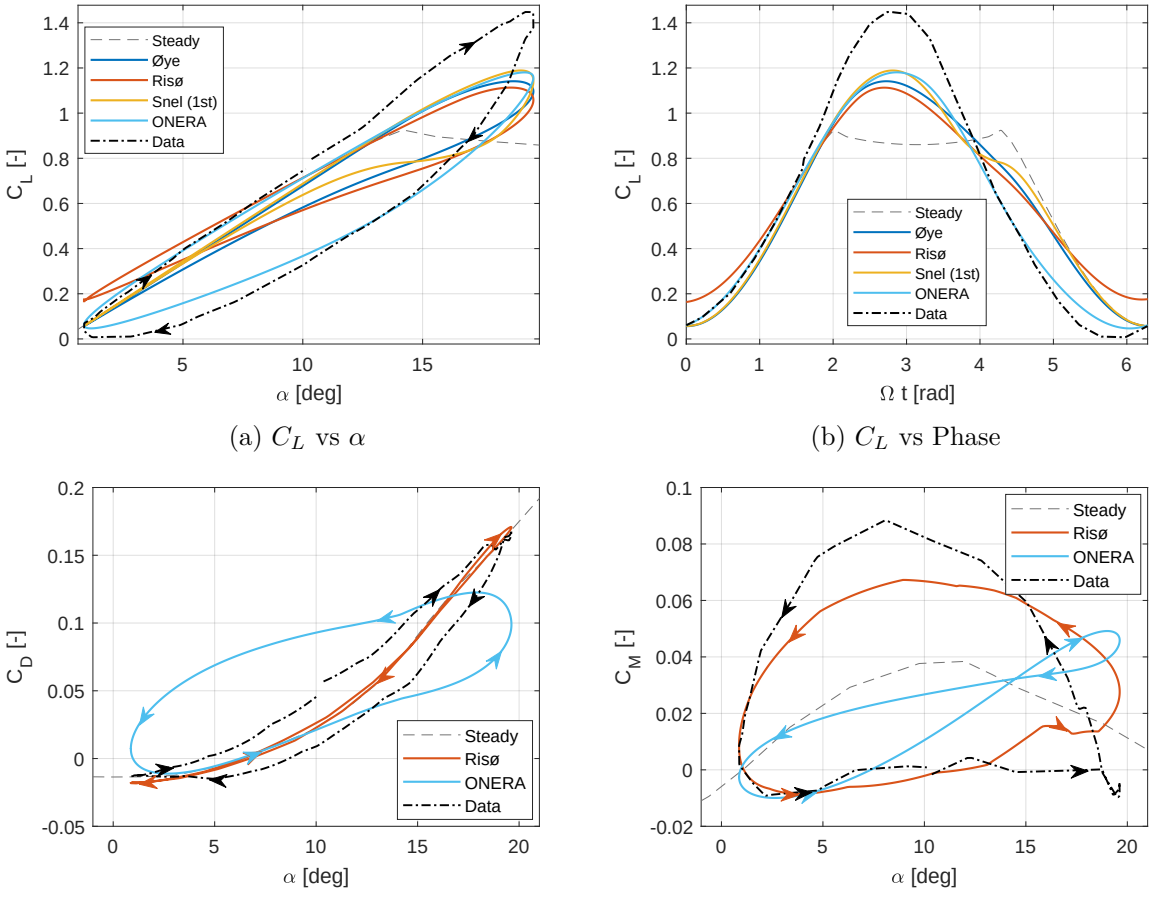

(a) C_L vs α

(b) C_L vs Phase

(c) C_D vs α

(d) C_M vs α

Figure 4.14: Model responses for the NACA0030 airfoil where $k = 0.153$, $\alpha_m = 10°$ and $\alpha_a = 10°$

4.6 Ramp function

In addition to sinusoidal oscillations the response to a ramp function for the two symmetrical airfoils, NACA0015 and NACA0030, is investigated. This is to compare the models in a non-periodic case. The chosen ramp goes from 0 to 30° at a reduced ramp rate of 0.0116 which dimensionally corresponds roughly $100°/s$ in the wind tunnel where $c = 0.55\ m$ and $U \approx 40\ m/s$. Therefore the 30° sweep is finished in around 0.33 seconds. The data shown is averaged over 5 runs. Similarly to all other measurement data the Reynolds number is close to 1.5 million and the Mach number is roughly 0.12.

In Figure 4.15 the angle of attack ramp shapes of the two measurement campaigns are seen to have only minor differences for each airfoil.

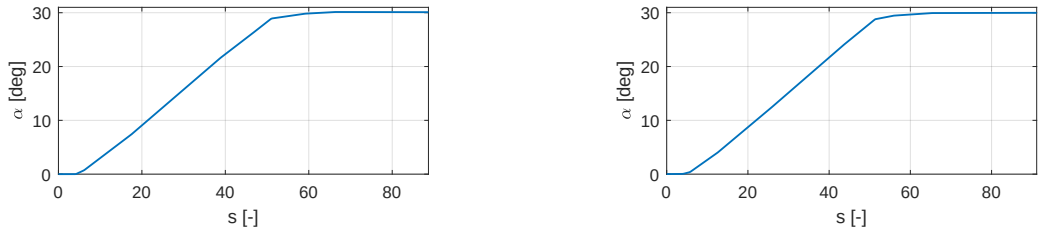

(a) NACA0015 (b) NACA0030

Figure 4.15: Angle of attack against time for the ramp functions

The lift response is found in Figure 4.16. Here it is the extreme loads, so the peak in the lift coefficient, and the following transition back to the steady lift that are important.

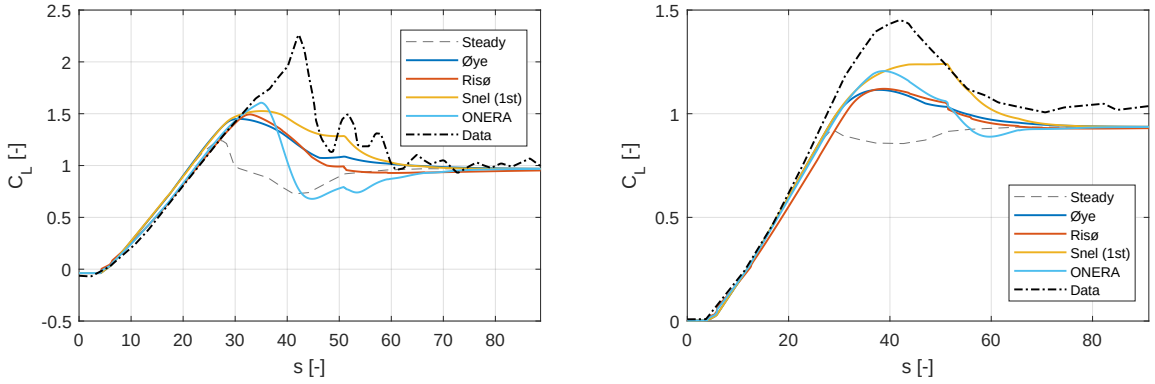

(a) NACA0015 (b) NACA0030

Figure 4.16: Lift coefficient against non-dimensional time for the ramp functions

Looking at the data, only the NACA0015 airfoil shows clear leading edge vortex formation and shedding with a sharp drop off after the large C_L peak. This is followed by rapid oscillations in all three coefficients due to the shedding of more vortices at a high frequency. As the data is the average of 5 measurements it is likely that these higher frequency oscillations are triggered by the separation of the leading edge vortex and so reoccur similarly in each test.

The NACA0030 will also have unsteadiness and vortices shedding after stall. That this is not visible in the averaged data indicates that it is more random and has averaged out over the 5 runs. Another notable point in the NACA0030 data is that it does not tend towards the steady curve towards the end. This could simply be due to not measuring long enough for the transients to die out. It could also be due to the wind tunnel conditions differing between runs or perhaps the large thickness resulting in more blockage effects which, as the wind tunnel is closed, may add extra transients that act on a larger time scale.
Additionally, it can be seen that the linear part of the data extends past stall which indicates that in this case for both airfoils there is a time delay where the flow is remains fully attached and no separation occurs.

All dynamic stall models predict an overshoot in the lift coefficient over the static peak, although none reach the peak C_L in the data. Table 4.12 shows these overshoots for the lift coefficient and angle of attack of the stall peak. For the analysis here two of the parameters used to quantify the differences in the hysteresis loops are modified for use for the ramp case. These are $\Delta C_{L,max}$ and $\Delta\alpha\left|_{C_{L,max}}\right.$. They are changed such that they represent the difference to the steady peak lift coefficient instead of the unsteady data peak and are therefore named $\Delta C^{st}_{L,max}$ and $\Delta\alpha\left|^{st}_{C_{L,max}}\right.$.

Table 4.12: Comparison of overshoots in C_L and α for the peaks in the ramp cases with respect to the steady curve

Airfoil	Parameter	Unit	Øye	Risø	Snel (1st)	ONERA	Data
NACA0015	$\Delta C^{st}_{L,max}$	[-]	0.204	0.247	0.279	0.360	1.016
	$\Delta C^{st}_{L,max}$	[%]	16.3%	19.8%	22.4%	28.8%	81.5%
	$\Delta\alpha\left\|^{st}_{C_{L,max}}\right.$	$[deg]$	2.6°	4.0°	5.5°	5.4°	10.0°
NACA0030	$\Delta C^{st}_{L,max}$	[-]	0.189	0.195	0.315	0.280	0.527
	$\Delta C^{st}_{L,max}$	[%]	20.5%	21.0%	34.0%	30.3%	56.8%
	$\Delta\alpha\left\|^{st}_{C_{L,max}}\right.$	$[deg]$	6.1°	6.7°	14.4°	6.7°	8.7°

This shows that the in unsteady data of the NACA0015 the lift peak is delayed by 10° and reaches a C_L almost double that of the static stall peak. None of the dynamic stall models come close to this with the ONERA model coming the closest in terms of lift and Snel's model in terms of α. Øye's model underestimates the location of the peak the most by 7.4°. Although, as this is a clear leading edge vortex case, it is not expected that the Øye, Risø or Snel models will be able to model this accurately due to only modeling trailing edge stall.
For the NACA0030 the match between the peak of the data and the models is slightly improved with Snel's model now predicting the highest peak C_L. This peak occurs 5.7° after the peak in the data, though, which is due to Snel's model not showing a conventional peak in Figure 4.16b. Rather, it shows a plateau at the highest C_L caused by the forcing $\Delta\dot{C}^{pot}_L$ applied in stall when $\dot{\alpha}$ is non-zero. As the data does not show similar behaviour this is possibly unphysical, although it does improve the match to the data for both airfoils in Figure 4.16.
The ONERA model drops below static lift values after the stall delay, $\Delta\tau$, for the NACA0015 airfoil and after the ramp is finished for the NACA0030 airfoil. This is similar to the behaviour

in for example Figure 4.11 which is seen as unphysical. In the leading edge stall case the ONERA model does roughly predict the same magnitude of drop in lift after stall. Therefore, an increased value of the stall delay parameter, $\Delta\tau$, will allow the ONERA model to match the data significantly better for the NACA0015 airfoil. As the peak of the unsteady data is 15.4 and 13.4 non-dimensional time units after the static stall peak for the for the NACA0015 and the NACA0030 respectively, this data would suggest a new value of roughly $\Delta\tau = 14$.

The moment and drag responses to the ramp function are shown in Figures 4.17 and 4.18 respectively.

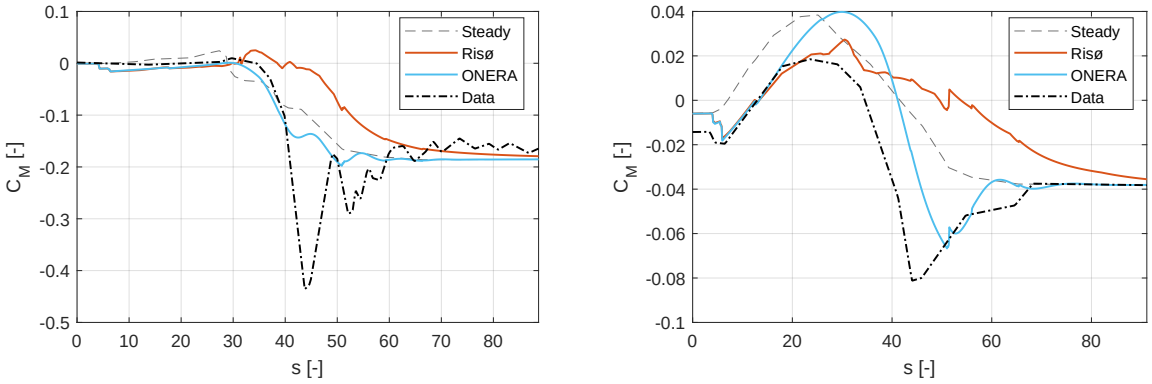

(a) NACA0015 (b) NACA0030

Figure 4.17: Moment coefficient against time for the ramp functions

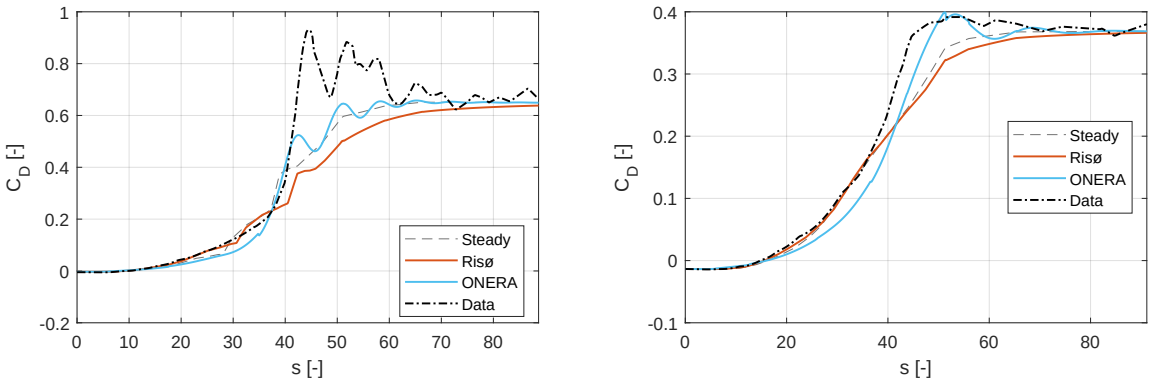

(a) NACA0015 (b) NACA0030

Figure 4.18: Drag coefficient against time for the ramp functions

For both coefficients and both airfoils the Risø model matches the data most accurately before stall, so during the first 30-40 non-dimensional time units. Hereafter, it is the ONERA model that captures the drop in moment coefficient and the reattachment the best. The ONERA model even captures the oscillations due to the vortex shedding a little. The discrete jumps in the Risø results are due to the jumps in $\dot{\alpha}$ at the start and end of the ramp and due to the moment arm as a function of the separation point not being completely smooth.

4.7 Discussion

Overall there is not one model that always outshines the other models in this 2D comparison against measurement data. Each model has different strengths and weaknesses and each model has at least one case with the lowest Euclidean norm.

The Risø model has the best attached flow behaviour for the lift, drag and, in a pure pitching motion, the moment coefficient. The ONERA model, on the other hand, performs better for the moment coefficient in the attached flow pure plunging case, although it does not fully capture the rotation of the lift hysteresis loop which is arguably the more important as C_L is in general the most important coefficient. For the drag coefficient in attached flow the ONERA model often gives the hysteresis loop in the wrong direction and so gives a deterioration in accuracy from the static curve.

Further into stall the ONERA model in general has a slight edge due to the hard stall delay being present in $\Delta\tau$. However, in the cases that it was not the best model, it was often the worst and occasionally showed unphysical figure-8 shapes in C_L at high angles of attack in particular in deep stall. It additionally always predicts stall to early which results in it generally having the largest Euclidean norms for the lift despite capturing the lift peak the best. This early stall can be fixed relatively easily in the ONERA model by increasing $\Delta\tau$.
The Risø and Øye models in general have similar peak values in lift coefficient and underestimate the peak lift coefficient which is unconservative for extreme loads. Broadly speaking Øye's model performs better than the Risø model for the thickest airfoil, the NACA0030, while for the 15% thick airfoil this is the other way around. These differences between the Øye and Risø models are largely due to the attached flow behaviour rather than having different stall properties. Snel's model has a slightly higher peak C_L in general than the Risø and Øye models; however, predicts reattachment too quickly. Despite this, Snel's model is found to have the best l^2-norms for the lift for the moderate and deep stall cases.

For the high k cases the ONERA model outperforms the other models for the lift, but produces C_D and C_M shapes very different from that data for the $k = 0.153$ case. These drag and moment coefficients seem more difficult to predict overall. This is possibly due to them being sensitive to small changes in for example the location of the center of pressure or the angle of the resultant force. It could also simply be due to there being less research and tuning done into the drag and moment coefficients in dynamic stall. There are even some cases where the correction introduced by the models make the match with the experimental data worse. The moment coefficient hysteresis loops are in particular hit or miss when looking at the pitch damping coefficient and if there is a figure-8 shape or not. In general for attached flow the Risø model performs more reliably for C_D and C_M. However, in deep stall the ONERA model often outperforms the Risø model for these coefficients which is highlighted in particular by the deep stall and ramp cases.

The Øye model is found to be the most robust model and never shows any undesirable behaviour, although in general the other models are more accurate. The Risø model follows closely on robustness for the lift; however, shows too much attached flow behaviour in the light stall cases. This is interesting as the flat plate values from Theodorsen's theory are used, while the airfoils used here are at least 15% thick. If the circulatory parameters in the Risø model (A_1,

A_2, b_1 and b_2) had been tailored to the thicker airfoils, then the attached flow behaviour would have been larger and the fit with the data worse. Despite these attached flow loops being too thick, they do still improve the fit to the data and reduce the l^2-norms for the 15% thick airfoils.

All models do give a great improvement with respect to no dynamic stall model being used at all. Furthermore, perfect matches with the data are not expected as the measurement data contains its own uncertainties in particular further into stall. There are some cases where the dynamic stall models even fail to capture the correct shape such as in Figure 4.3 for the NACA0015 in light stall where the drop in lift due to stall only occurs on the return loop or Figure 4.6 where leading edge stall is seen again for the NACA0015. These cases show that there is still room for improvement in these dynamic stall models.
For the 15% thick airfoils both leading edge stall and trailing edge stall is seen to occur. In general the leading edge stall characteristics are seen in the more extreme cases so with the larger k's and α_a's which will only rarely occur in wind turbines. More often either pure trailing edge stall or a mix of the stall types will occur. This mix of stall types, as for example seen in Figure 4.8 and to a lesser extent Figure 4.11, adds an extra level of complexity for the modeling of dynamic stall for wind turbine applications. It is important though, as this thickness is often used in the regions of the blades where the majority of the power is generated. The ONERA model is most suited to capture this complex behaviour and could be improved even more through the large tunability of the model. For the Risø model the presence of this leading edge stall violates the assumption made when neglecting the leading edge vortex module from the Beddoes-Leishman model.

CHAPTER 5

Aeroelasticity

In this chapter various full turbine response cases are used to compare the performance of the dynamic stall models. First, the fundamentals of an aeroelastic code are briefly detailed in Section 5.1. This is then followed by an extreme load case in Section 5.2, various standstill cases in Section 5.3 and the a flutter speed comparison in Section 5.4.
In this chapter the dynamic drag correction in the ONERA model is turned off due to it's poor performance in Chapter 4.
The turbine used is a Vestas turbine which is already in operation and has proven itself in the field. In this chapter the boundaries of the blade stability of this turbine will be pushed to compare the dynamic stall models. It should be mentioned that this is purely an theoretical exercise that is not representative of any real life behaviour of the Vestas turbine. To ensure the confidentiality of Vestas proprietary information the results have been normalized.

5.1 Aeroelastic code

An aeroelastic code based on Blade Element Momentum theory, BEM, is an efficient tool to model the response of a turbine in the time domain for a certain wind field input. It combines the aerodynamics, structure and control of the turbine. This results in a complex environment due to the sheer size of the system and the interactions between the different components. Additionally, each of these components have their own assumptions and accuracies. One benefit of using such a code is that the different models and components can be turned on or off and different settings applied as desired. This allows for differences in turbine response to a new dynamic stall model to be investigated while using identical values for all other inputs.

The most basic version of BEM uses the following assumptions: [37] [38]

- Steady flow conditions (So no turbulence, vibrations or controls)
- No radial interdependence
- Spanwise flow is negligible (2D characteristics)
- Axially symmetric conditions
- No yaw angle
- No wind shear or tower shadow

These assumptions allow for the rotor plane to be divided up into a number of radial annuli in which the 1D momentum equation is satisfied. This is done by making a balance between the out-of-plane aerodynamic force generated by the blades and the thrust force acting on the wind as in Equation 5.1. A similar equation can be set up between the in-plane aerodynamic

force and the power coefficient for an annulus and is shown in Equation 5.2.

$$\frac{1}{2}\rho U_\infty^2 C_T 2\pi R dr = \frac{1}{2}\rho U_{rel}^2 C_n c B dr \tag{5.1}$$

$$\frac{1}{2}\rho U_\infty^3 C_P 2\pi R dr = \Omega r \frac{1}{2}\rho U_{rel}^2 C_t c B dr \tag{5.2}$$

Where ρ is the air density, U_∞ the free stream velocity, C_T the local thrust coefficient, R the rotor radius, dr the radial length of the annuli, C_T the local thrust coefficient, U_{rel} the relative velocity to the airfoil, C_n the normal coefficient (out-of-plane) from the airfoil forces, B the number of blades, C_P the local power coefficient, Ω the rotational speed of the rotor, r the radial position of the annuli and C_t the tangential coefficient (in-plane) from the airfoil forces. Due to the dependence of these equations on the axial and tangential induction factors they need to be solved in an iterative manner.
In most operating conditions the assumptions for these 1D momentum equations are severely violated and therefore several extensions to the classical BEM can be used: [37] [38]

- Dynamic stall
- Dynamic inflow
- Tip (and root) correction due to having a finite number of blades
- Yawed inflow
- Tower shadow modelling
- 3D Lift correction
- Turbulent wake state

These extensions allow the BEM code to be used in a much more general environment; however, are all still approximations of the physics involved and so contain errors of their own. The dynamic stall module will affect the C_n and C_t terms in Equations 5.1 and 5.2 and so change the inductions and the thrust and power coefficients. Additionally, this changed loading will affect the deformations and vice versa which is important for instabilities.

In the standstill cases BEM theory is simplified due to the lack of power generation, thrust and blade rotation. Other issues do become more important such as crossflow along the blade [39] and the fidelity of the aerodynamics at high angles of attack in terms of the static coefficient curves, dynamic stall and periodic vortex shedding. Furthermore, the tip and root corrections will be different due to the different load distribution over the blade.

During the implementation of the dynamic stall models in the aeroelastic code an extra assumption is made to simplify and smooth $\dot{\alpha}$ which will affect the Risø and ONERA models. This is that $\dot{\alpha}$ is approximated as the physical pitching velocity of the airfoil section only. Therefore, the heaving component, $\ddot{h}$, and the rotation of the wind field are neglected. The reasoning and estimation of the effects of this assumption are detailed in Appendix G.

5.2 Extreme load

The IEC Design Load Case, DLC, 1.4 is for simulating a worst case scenario where a large gust is encountered together with a change in wind direction [40]. The so called coherent gust with

direction change. To make the case more extreme and push the angle of attack further into stall, the velocity at the start of the gust is lowered to 5 m/s and the controller state frozen at $t = 10$ s. Furthermore, all dynamic aerodynamic corrections such as inflow or wake are turned off including tower shadow. This does mean that this run is not representative of the normal behaviour of the turbine or aeroelastic code; however, allows for a better comparison of the dynamic stall models in isolation. The added complexity of the blades deflecting during the simulation is still present in addition to the effects of the varying wind velocity and rotor speed.
As the IEC standard states [40] the wind ramp from 5 m/s will increase the wind speed by 15 m/s and change the wind direction by 144° over 10 seconds. This results in the time series of angle of attack in Figure 5.1 at 80% along the analysed blade when no dynamic stall model[1] is used. When a dynamic stall model is used, the angle of attack will be different due to the difference forces causing slightly different blade deflections, rotor speed and induced velocities.

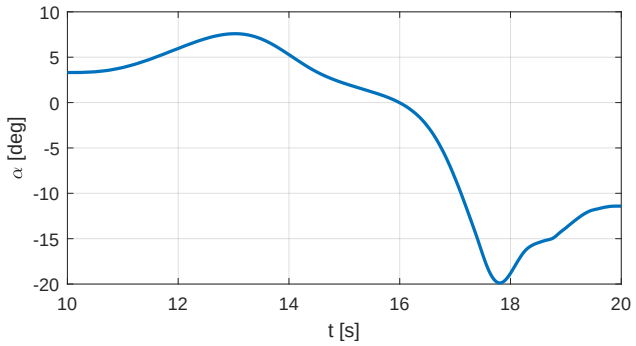

Figure 5.1: Angle of attack response at 80% along the blade for the modified DLC 1.4 case with no dynamic stall model

The results in the lift coefficients in Figure 5.2. C_L has been normalized using the absolute value of the negative stall peak lift coefficient from the static curve.

The model performance seen here is roughly similar to that found for the NACA0030 ramp case in Section 4.6 due to the ramp like nature in α vs t plot between 16 and 18 seconds. Furthermore, the drop-off in lift coefficient after the stall peak in the static curve is gradual, similar to that of the NACA0030 airfoil. One difference to the ramp case is that Snel's model does not predict a much larger peak C_L here than the Øye and Risø models. The overshoots over the steady stall peak are 18.3%, 17.5% and 19.8% for the Øye, Risø and Snel models respectively. For the ONERA model it is only 3.5%.
That the ONERA model does not show much hysteresis behaviour is due to several factors such as different blade deflections and rotor speed. However, the most important reason is the method of implementation of the W_1 and W_0' terms. These time derivatives are fundamental to the stall behaviour of the ONERA model as detailed in Appendix G.
In general the lift overshoots are lower here than for the NACA0030 ramp case in Section 4.6 indicating that this case is slightly less extreme. That they are not far off indicates that the ramp case is not entirely unfeasible for in a turbine, although the case here only reaches -20°,

[1]For ease of reading the case with no dynamic stall model is called the steady model.

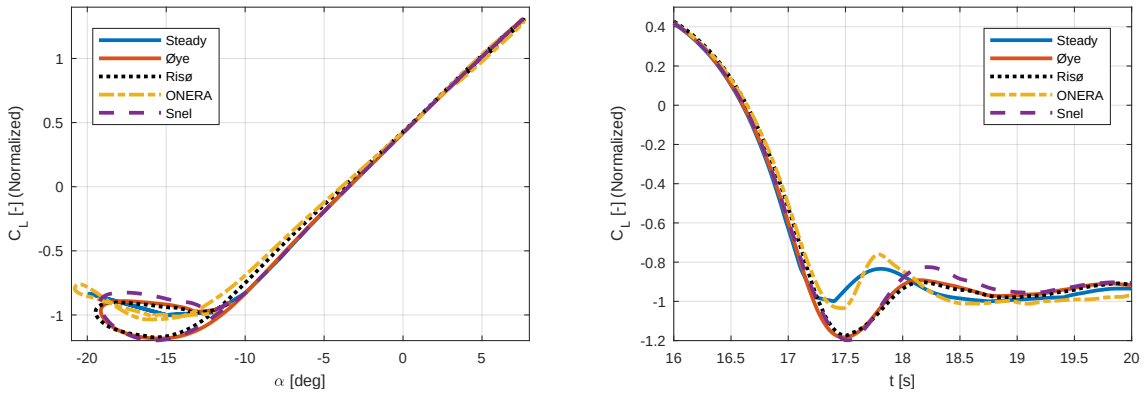

(a) C_L vs α (b) C_L vs t

Figure 5.2: C_L model responses for the modified DLC 1.4 case at 80% along the blade

while the ramp goes to 30°.

The flapwise tip position is shown in Figure 5.3 where a positive tip deflection is towards the tower and a negative tip deflection is away from the tower. It is normalized such that the extreme values of the steady model response are set to 1 and -1. Therefore, the normalized tip position of zero is no longer the true zero.

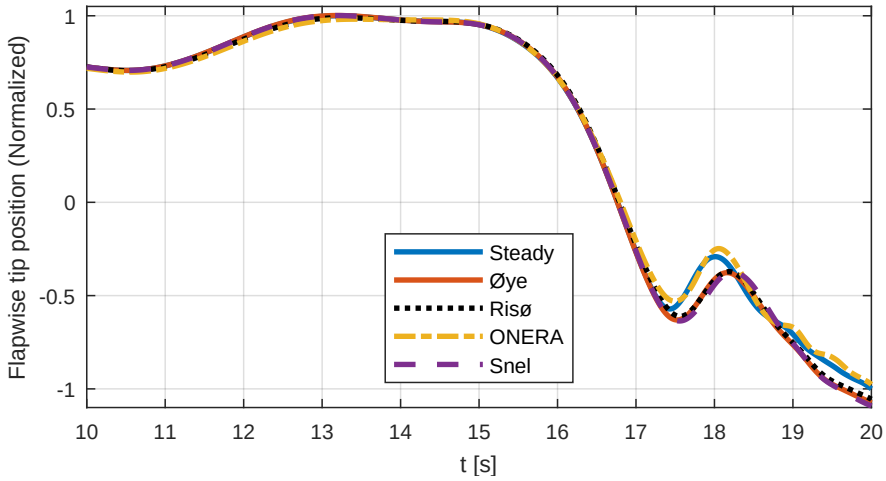

Figure 5.3: t vs normalized tip position model responses for the modified DLC 1.4 case

For the attached flow region all models perform similarly with the only differences being that the Risø and ONERA models have a slight time delay. For the initial drop in the tip position, so between $t = 16$ s and $t = 18$ s, all dynamic stall models except ONERA predict a larger tip deflection at the peak. One of the reasons that the ONERA model shows a smaller deflection than the steady case is due to the minimal lift overshoot combined with a lower rotor speed. This lower rotor speed is caused by the attached flow dynamics gradually slowing the rotor

down relative to the Steady model. At $t = 17\ s$ the ONERA model has a 1.2% lower rotor speed than the Steady model while the Risø model has an 0.1% decrease and the Øye and Snel models an 0.7% increase. A lower relative velocity over the blade will reduce the dimensional forces and therefore also the tip deflection. Furthermore, the more inboard sections will reach stall earlier and then also reach the drop in lift back to the other side of the steady coefficient (as in Figure 5.2b between 17.5 s and 18 s) earlier. This smaller magnitude of the lift coefficient inboard will additionally contribute to the reduced the tip deflection.

After $t = 18$ seconds the tip continues to deflect away from the tower despite α decreasing due to the relative velocity increasing for all models. This is in turn due to the large yaw angle combined with the blade being at the azimuthal angles where it rotates into the wind.

5.3 Standstill

The IEC standard states in Design Load Case (DLC) 6.2 that a parked turbine without a backup generator must withstand a 50 year extreme wind coming from any direction [40]. This means that the blades need to be designed such that they can withstand vibrating in (deep) stall. The most critical directions are generally when a blade is in stall resulting in stall-induced vibrations.

When in stall it is possible that a translatory motion in certain vibration directions can have negative aerodynamic damping. If this negative aerodynamic damping is larger than the other contributions to the damping of the system, such as structural damping, then an instability will occur. For the flapwise direction the negative slope of the C_L - α curve in stall adds negative damping to the vibration [41]. Dynamic stall will counter this negative damping making the dynamic stall model an important part of the blade standstill stability. These flapwise oscillations are generally more damped than those in the edgewise direction [42]. This is also what Bir and Jonkman [10] found using an aeroelastic code to simulate such instabilities on the NREL baseline 5 MW wind turbine [18] when parked and free to idle. They found that when the turbine was parked the first blade edgewise mode (out-of-plane due to the pitch angle of 90°) showed negative damping at yaw angles of ±20° and ±30°. This negative damping at a yaw angle of 30° is also found by Wang et al. [43] for all azimuthal angles. These edgewise instabilities are damped by the dynamic stall models as the vibration of the blade will always contain a flapwise component.

5.3.1 Cases and Methodology

For DLC 6.2, the yaw angles where the negative damping is found in literature are used (i.e. ±20° and ±30°) for the wind speed 42.5 m/s. 42.5 m/s corresponds to the 50 year extreme wind speed for the IEC wind class II. Furthermore, three extra cases are looked into to compare the models in a wider range of situations. First, a lower wind speed case at a very large yaw error and wind shear is used. This is then followed by two similar cases with different turbulence seeds and slightly different conditions which will be used to estimate the sensitivity. These conditions are summarized in Table 5.1 in order of increasing wind speed. Here TI stands for turbulence intensity and α_{shear} for the wind shear exponent.

Table 5.1: Conditions for the standstill cases

Case	Type	Wind Speed $[m/s]$	Yaw $[deg]$	TI [-]	α_{shear} [-]	ρ $[kg/m^3]$
1	-	12.09	-67.16°	0.0644	0.459	1.161
2	-	17.25	-37.12°	0.1033	0.085	1.124
3	-	17.92	-36.73°	0.0974	0.11	1.122
4	DLC 6.2	42.5	20°	0.11	0.11	1.225
5	DLC 6.2	42.5	-20°	0.11	0.11	1.225
6	DLC 6.2	42.5	30°	0.11	0.11	1.225
7	DLC 6.2	42.5	-30°	0.11	0.11	1.225

From these conditions the angle of attack regions that each blade will be in can be determined. These are shown in Table 5.2 where the angles of attack have been rounded to the nearest 5° for confidentiality.

Table 5.2: Mean angles of attack for each blade at 88% span rounded to the nearest 5°

Case	α_1 $[deg]$	α_2 $[deg]$	α_3 $[deg]$
1	-65°	30°	65°
2	20°	-35°	25°
3	20°	-35°	25°
4	20°	-25°	0°
5	-25°	0°	20°
6	30°	-30°	0°
7	-30°	0°	30°

Before any analysis is conducted it should be noted that the dynamic stall models are not well verified for deep stall [44] and so the accuracy of the models will be less than that seen in the comparison to the measurement data in Chapter 4. Additionally if even a small time lag is added to the quasi-static deep stall behaviour, then the stability limits increase significantly [45]. This could result in small modelling differences causing large differences in the stability limits. Furthermore, the case at a 65° yaw angle will, in particular, have a large amount of spanwise flow for at least one blade. Such spanwise flow will affect the aerodynamics greatly. Despite these issues it is still useful to compare the models in these situations to better understand their behaviour and design limits.
Another potential issue for the accuracy is the large reduced frequencies seen in these standstill cases which are often outside the design range of the models. These reduced frequencies for the instabilities are estimated using the NREL 5MW reference turbine [18] in Table 5.3. Two frequencies are used: the 1st flapwise and the 1st edgewise blade modes.

Table 5.3: Example k's for the 5MW NREL turbine [18] at 88% span

Wind speed [m/s]	k for 1st flap	k for 1st edge
12.1	0.41	0.66
17.5	0.28	0.46
42.5	0.11	0.19

These reduced frequencies are significantly higher than those used in the 2D comparison in Chapter 4. These were based on 1P excitations, though, rather than standstill vibrations. The reduced frequencies of the currently used Vestas turbine are a little lower than those of the NREL turbine, although still the same order of magnitude. Furthermore, using a single k is a simplification as, when the blade is oscillating in these modes, the relative velocity will be varying during each cycle due to the blade motion. The turbulence will additionally cause the relative velocity to vary within each cycle.

Negative aerodynamic damping does not necessarily result in a negatively damped system as the structure will always provide some positive damping. This structural damping is used as a metric to compare the models. The original structural damping of the blades, specifically the logarithmic decrement in the flapwise and edgewise directions, is multiplied by a percentage called the Damping factor, abbreviated DF. This DF is varied to test the stability across a wide range of structural damping levels[2]. Then by finding the DF where the blades become unstable for each model, the models can be compared for how much aerodynamic damping they add to the system. Instabilities are detected using the highest magnitude of the peak-to-peak root edgewise bending moment, M_{edge}. It is calculates as the maximum value of the bending moment subtracted by the minimum with the criterion that these extremes occur within of 5 seconds of each other. When M_{edge} is seen to suddenly increase it is an indication of an instability. At the end of Section 5.3.3 the dominant frequencies in the edgewise root bending moment are calculated to check that it is in fact the edgewise mode that becomes unstable as predicted in the literature.

5.3.2 Case 2 Results

Before the full results are given in Section 5.3.3, Case 2 is looked into in more detail starting with Figure 5.4 which shows M_{edge} plotted against DF. Here M_{edge} is normalized to 1 at the highest damping factor for the Steady model. The horizontal axis, so the Damping factor, is set to 100 at the point when $M_{edge} = 2$ for again the Steady model in case 2. So in Figure 5.4a $M_{edge} = 1$ at the highest DF of 400 and $M_{edge} = 2$ at a DF of 100. The normalization of M_{edge} is repeated separately for each case. This separate normalization per case prevents a comparison of the loads between the different cases. The main goal here, however, is to compare the different dynamic stall models to each other over a wide range of conditions. The normalization of DF is kept constant between the different cases such that the locations of the instabilities can still be compared.

[2]It is checked that the structural damping remains within the underdamped region for the damping ratio to prevent overdamped behaviour

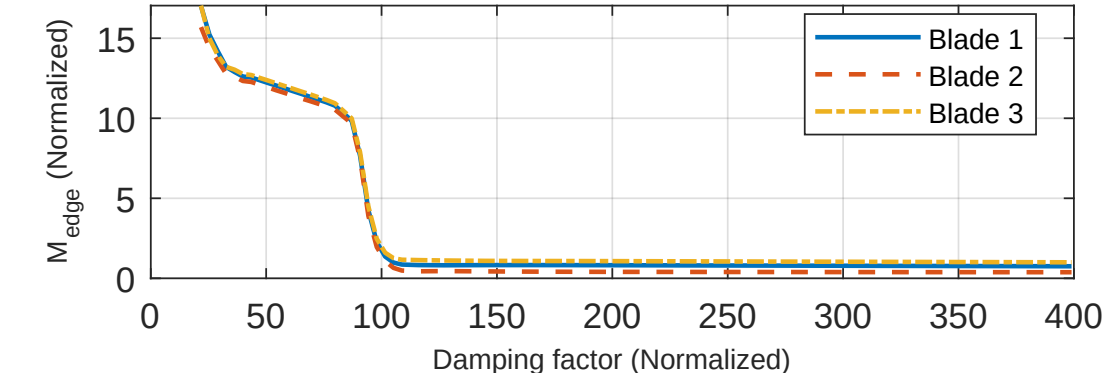

(a) No dynamic stall model (Steady)

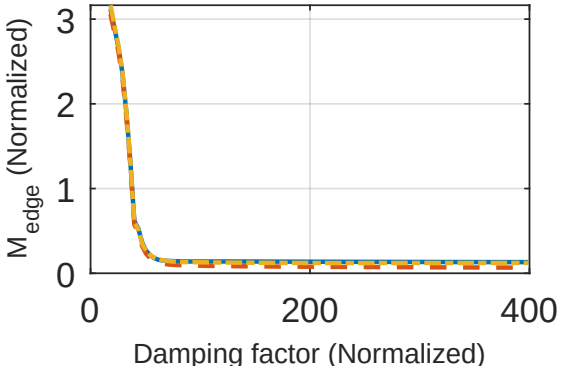

(b) Øye dynamic stall model

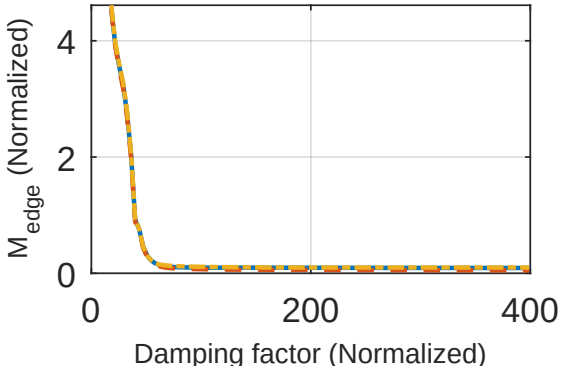

(c) Risø dynamic stall model

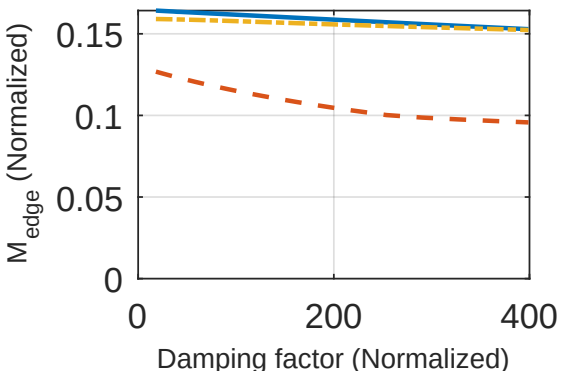

(d) Snel dynamic stall model

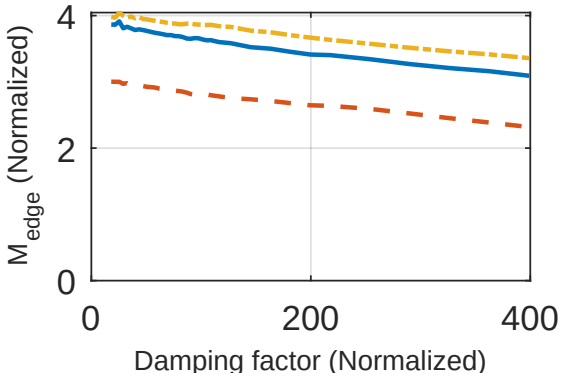

(e) ONERA dynamic stall model

Figure 5.4: Normalized peak-to-peak root edgewise bending moments for case 2

In these figures the Steady, Øye and Risø models all predict a sudden increase in M_{edge} at a certain DF indicating that the positive structual damping has become smaller than the negative damping from the aerodynamics and an instability occurs. Snel's model remains relatively constant at an M_{edge} well below 1, so below the steady value at max damping, indicating that no unstable behaviour occurs even at the lowest Damping factors. The opposite is the case for the ONERA model which is seen to have M_{edge} values above 1 even for the highest damping factors. Therefore, this model actually adds negative aerodynamic damping to the system.

The Øye and Risø models become unstable at lower Damping factors than the Steady case so these models add positive damping to the system. This is expected based on the research by Buhl [46] who looked at the damping of a wind turbine blade in HAWC2 after exciting the blade in edgewise direction, both with and without the Risø dynamic stall model enabled. He found that the dynamic stall model added damping for all angles of attack after stall where the dynamic stall model was active.

To get a better insight into how the models are behaving in these standstill cases, the lift coefficient is plotted against the angle of attack for the full time series at the highest DF in Figures 5.5 to 5.8. In Figure 5.4 blades 1 and 3 have higher M_{edge} values than blade 2, so the differences between the hysteresis loops on blades 1 and 3 will be more important. Unlike for the 2D hysteresis loops in Chapter 4, the angle of attack variations here are partially due to the turbulent inflow and partially due to the blade motion. Both the C_L and α are normalized to the values of positive and negative stall such that positive stall is at $C_L = 1$ and $\alpha = 1$ and negative stall at $C_L = -1$ and $\alpha = -1$. Here positive stall is defined as the peak with maximum lift for positive α's and negative stall as minimum lift point for negative α's.

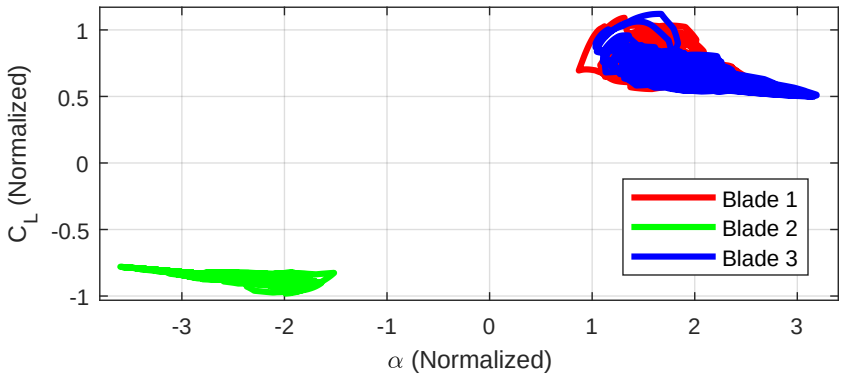

Figure 5.5: C_L time traces with Øye's model in Case 2 at the highest Damping factor

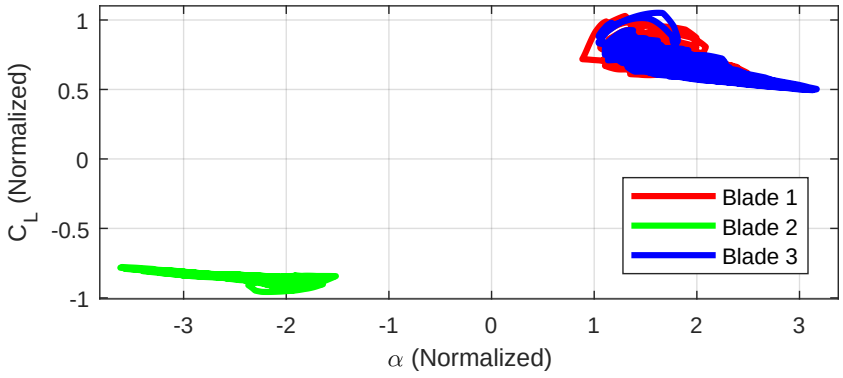

Figure 5.6: C_L time traces with the Risø model in Case 2 at the highest Damping factor

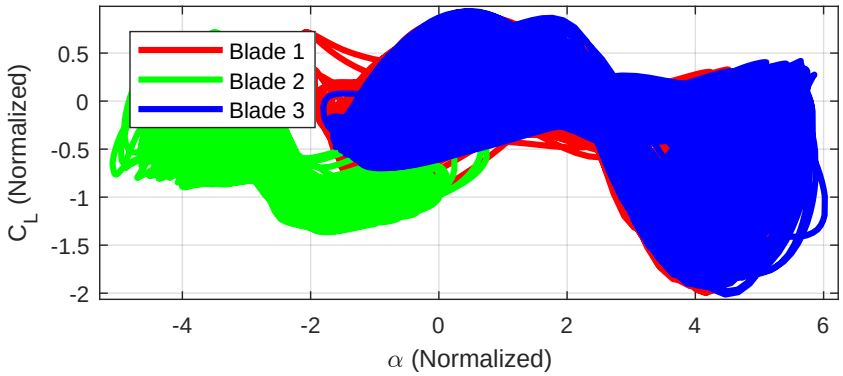

Figure 5.7: C_L time traces with the ONERA model in Case 2 at the highest Damping factor

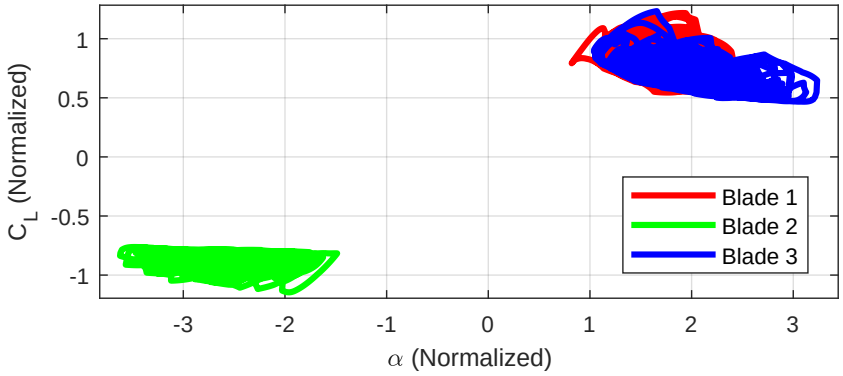

Figure 5.8: C_L time traces with Snel's model in Case 2 at the highest Damping factor

The Risø and Øye models are seen to perform similarly to each other with the Øye model showing a slightly higher peak C_L on both the sides of positive and negative stall. Snel's model has more hysteresis behaviour in general and in particular at the higher angles of attacks (roughly $|\alpha| > 2.5$) where large deviations from the static curve are seen.
The ONERA model, on the other hand, shows completely unphysical behaviour with huge figure-8 loops for each of the blades. This, combined with the knowledge that there are large flapwise oscillations, explains why the model adds negative damping to the system. The reason for these figure-8 loops is two fold. First of which is that these loop pass through a region between roughly 20° and 40° where the lift hysteresis loops go in the wrong direction, counter-clockwise, as shown in Figure D.7 in Appendix D.1 or even slightly in Figure 4.11. Secondly, it is due to the choices made in the implementation of the W_1 and W_0' terms in the aeroelastic code as already mentioned in Section 5.2 for the DLC 1.4 case and explained in more detail in Appendix G.

As the metric used is based on the edgewise bending moment, the behaviour of the dynamic drag coefficient is also important to look at. For the Risø model the normalized drag plots can be found in Figure 5.9. Here C_D is normalized to the range between 0 and 1 and for α the same normalization is used as for C_L. No dynamic drag plot is shown for the ONERA model as this drag correction was turned off after the poor results from the 2D comparison against

data.

This shows that the dynamic behaviour of the drag is minimal and the deviations from the static curve are small. Interestingly for blade 1 the drag coefficient even goes slightly negative.

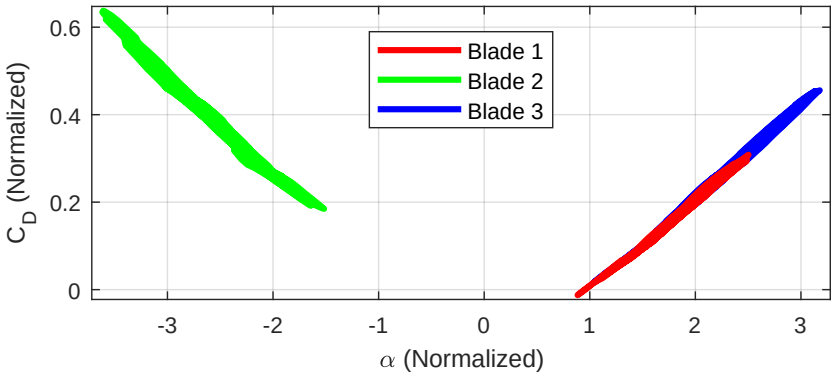

Figure 5.9: C_D time traces with the Risø model in Case 2 at the highest Damping factor

5.3.3 General Results

For all 7 cases, figures similar to Figure 5.4 are made. The values of M_{edge} for the worst blade at the minimum and maximum DF's in each of the cases can be found in Table 5.4.

Table 5.4: Extreme values of M_{edge} for the different dynamic stall models

Case		M_{edge} (Normalized) Steady	Øye	Risø	ONERA	Snel
Case 1	at min DF	185.83	4.86	0.77	13.53	1.09
	at max DF	1.00	0.79	0.68	9.35	1.01
Case 2	at min DF	17.14	3.92	8.97	4.05	0.19
	at max DF	1.00	0.13	0.10	3.36	0.15
Case 3	at min DF	17.31	4.05	9.48	4.32	0.18
	at max DF	1.00	0.13	0.11	3.63	0.16
Case 4	at min DF	4.51	0.57	0.63	5.41	0.54
	at max DF	1.00	0.45	0.50	3.66	0.49
Case 5	at min DF	3.90	0.55	0.62	4.97	0.73
	at max DF	1.00	0.48	0.48	2.70	0.58
Case 6	at min DF	3.74	0.89	0.98	3.79	0.26
	at max DF	1.00	0.21	0.21	3.18	0.20
Case 7	at min DF	4.99	1.07	2.36	5.87	0.59
	at max DF	1.00	0.40	0.39	3.71	0.55

The Steady model, so without any dynamic stall, always has a value of 1.00 at the highest

DF which is due to the normalization to this point. At the lowest M_{edge} the DF is always significantly higher which is due to the occurrence of an instability. The size of this peak M_{edge} at min DF is seen to decrease for the larger wind speeds. These increased wind speeds will increase the normal deflections before any instability occurs. Therefore, when an instability does occur, the blades do not have to increase the size of the oscillations as much to reach deflections large enough where the non-linearities in the system cause a limit cycle oscillation. In general the dynamic stall models reduce the edgewise loading at the maximum Damping factor which is due to the models adding damping. Of course the models can give a peak C_L larger than the static stall peak; however, overall the dynamic effects reduce the magnitude of the blade vibrations by adding damping. This damping is due to the hysteresis behaviour extracting energy over each cycle. The stark exception to this load reduction is the ONERA model indicating that the unstable behaviour in Figure 5.7 occurs regularly.
For every case the Øye and Risø models perform comparably at max DF and reduce the peak-to-peak root edgewise bending moment with respect to the steady case. This similarity indicates that the dynamic C_D correction in the Risø model has a smaller contribution than the other dynamic effects which is backed up by the time traces of the drag coefficient in Figure 5.9 showing minor deviations from the static curve.
Snel's model gives a similar M_{edge} at both the minimum and maximum Damping factor for all cases which indicates that it contributes a much larger amount of positive aerodynamic damping to the system than the other models. Even with the lowest level of structural damping, the blades remain stable. This is unexpected as the hysteresis loops in the 2D comparison chapter are similar. It is possibly due to Snel's model having the largest hysteresis loops in the deep stall cases especially for the larger k's as seen in Figure 4.11 in the 2D comparison chapter. This is investigated in more detail in Appendix D.2. This behaviour is furthermore seen within the aeroelastic code implementation in Figure 5.8 where Snel's model still shows dynamic behaviour when well into the fully separated flow region. Therefore, the amount of damping added by Snel's model is likely too large and possibly unphysical. However, this can not be determined conclusively without having measurement data[3].
For the two DLC6.2 cases at yaw angles of $\pm 20°$, so Cases 4 and 5, similar behaviour is seen with the Øye and Risø models not showing any signs of an instability. However, when looking at the cases with the yaw angles of $\pm 30°$, these two models do start to show unstable behaviour with the M_{edge} at min DF being significantly larger than that at max DF. Therefore, either the negative aerodynamic damping from the static curve is larger or the models provide less damping at these higher angles.

Next the locations of the instabilities are estimated in Table 5.5 by finding DF's of the intersections with $M_{edge} = 1$ and $M_{edge} = 2$ in the M_{edge} vs DF curves.

[3] Additionally this analysis is not fully comprehensive as it for example does not consider the direction of vibration which is an essential part of these instabilities [41] and could be influenced by dynamic stall.

Table 5.5: Damping factors for the crossings where M_{edge} is either equal to 1 or 2

Case		Damping factor (Normalized) Steady	Øye	Risø	ONERA	Snel
Case 1	at $M_{edge} = 1$	400	18	-	-	-
	at $M_{edge} = 2$	91	7	-	-	-
Case 2	at $M_{edge} = 1$	400	38	40	-	-
	at $M_{edge} = 2$	100	32	36	-	-
Case 3	at $M_{edge} = 1$	400	41	49	-	-
	at $M_{edge} = 2$	111	34	40	-	-
Case 4	at $M_{edge} = 1$	400	-	-	-	-
	at $M_{edge} = 2$	208	-	-	-	-
Case 5	at $M_{edge} = 1$	400	-	-	-	-
	at $M_{edge} = 2$	183	-	-	-	-
Case 6	at $M_{edge} = 1$	400	-	-	-	-
	at $M_{edge} = 2$	187	-	-	-	-
Case 7	at $M_{edge} = 1$	400	8	20	-	-
	at $M_{edge} = 2$	209	-	10	-	-

For all cases the intersection of the Steady model with $M_{edge} = 1$ is at a normalized DF of 400 as this point is used to normalize M_{edge} to 1. The Damping factor itself is normalized to the intersection of case 2 with $M_{edge} = 2$ for the Steady model which is why the Damping factor here is exactly 100. For Case 1 the Steady model has the lowest intersection with $M_{edge} = 2$ at a DF of 91. This is partly due to the lower wind speed which causes the relative magnitude of the aerodynamic damping to decrease with respect to the structural damping. Therefore, the system can be kept stable with a lower structural damping level. This is also partly why the intersections with $M_{edge} = 2$ for the Cases 4 to 7 occur at DF's much higher than 100 for the Steady model. It should be noted that for Case 1 the instability actually occurs at a DF of around 20 as shown in Figure 5.10 which is significantly lower than than the 91 in Table 5.5 for the intersection with $M_{edge} = 2$. This is the only case where the $M_{edge} = 2$ criterion did not represent the correct area where the instability occurs.

Furthermore, for Case 1, it is seen that Øye's model shows intersections with M_{edge} in Table 5.5, while the Risø model does not. This indicates that the Risø model provides more damping here. However, for all other cases where intersections for the Øye model are seen, this is the other way around with Øye's model giving a higher damping. Case 1 is possibly the exception due to having blades at $\pm 65°$ where Øye's model simply gives the static curve while the Risø model still accounts for the delay in angle of attack from the circulatory terms. In the sensitivity analysis in Section 5.3.4 the effect of changes to the time constants for the Øye and Risø models show a very small sensitivity to these time constants for this case. This indicates that it is the two blades in the fully separated flow regime that are the main drivers of the instability here. Interestingly, this is despite both models showing the blade at 30° (Blade 2) to have the highest M_{edge} as in Figure 5.10 for the Steady model.

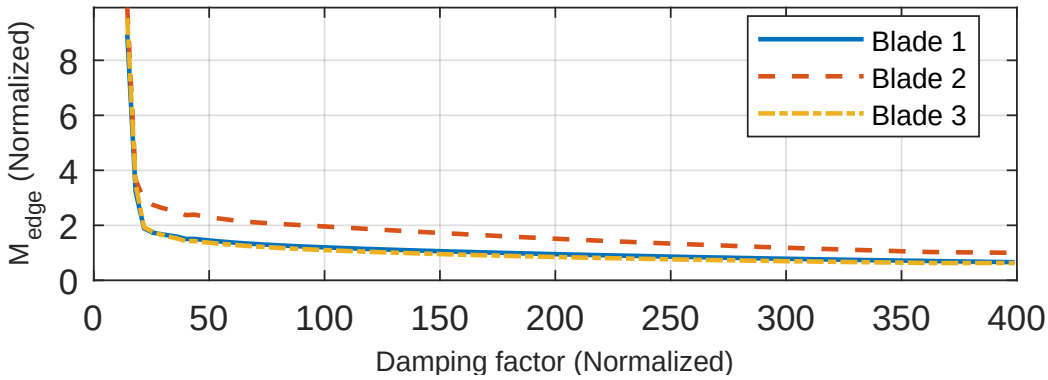

Figure 5.10: Normalized peak-to-peak root edgewise bending moments for case 1 with the Steady model

For the Øye or Risø models, in the cases where an instability is seen, this instability always occurs at a 50% or more reduced DF meaning that the required structural damping level to keep the system stable is reduced by at least factor 2. Therefore, large amounts of positive damping are added to the blade by these dynamic stall models.
When comparing Cases 2 and 3 the differences are larger than would be expected from the small differences in setup. There is an 11% increase in the DF for the intersection with $M_{edge} = 2$ for the Steady model[4] and even a 23% increase for the Risø model at $M_{edge} = 1$ indicating a large sensitivity of these results to changes in the wind time series.
When looking at the DLC 6.2 cases, it is seen that Case 4, so at a yaw angle of 20°, almost has the highest DF for the intersection with $M_{edge} = 2$ for the Steady model. Therefore this is likely the case with the largest magnitude of negative aerodynamic damping from the static curve. Despite this, no instabilities are seen for the Øye or Risø models which indicates that this is the case where the damping provided by the Øye and Risø models is the largest.
Case 5 is similarly always kept stable by the dynamic stall models.
Cases 6 and 7, on the other hand, do become unstable at the lower DF's for the Øye and Risø models. For Case 6 no intersections are seen in Table 5.5 as the instabilities start slightly before the lowest DF and have not yet reached $M_{edge} = 1$. An increase is already seen in the M_{edge} in Table 5.4 between the min and max DF's.

To get a better understanding of the instabilities that occur, the Fourier transform of the root edgewise bending moment is looked at to find the dominant peak for the blade with the worst M_{edge}. This is then matched to the closest blade mode[5]. The results are shown in Table 5.6. The ONERA model was omitted from this analysis due to its poor behaviour.

[4]It should be noted that $M_{edge} = 2$ corresponds to a slightly different dimensional value for each of the cases due to the different normalization. It still is an accurate representation of the location of the instability though.

[5]This is a simplification of reality as these blade modes can manifest themselves in different (a)symmetrical full turbine modes.

Table 5.6: Dominant blade mode for the highest and lowest Damping Factors in the blade with the largest M_{edge}

Case		Steady	Øye	Risø	Snel
Case 1	at min DF	2^{nd} edge	2^{nd} edge	1^{st} edge	1^{st} flap
	at max DF	1^{st} flap	1^{st} flap	1^{st} flap	1^{st} flap
Case 2	at min DF	2^{nd} edge	1^{st} edge	1^{st} edge	1^{st} edge
	at max DF	1^{st} flap	1^{st} flap	1^{st} flap	1^{st} flap
Case 3	at min DF	2^{nd} edge	1^{st} edge	1^{st} edge	1^{st} edge
	at max DF	1^{st} flap	1^{st} flap	1^{st} flap	1^{st} flap
Case 4	at min DF	1^{st} edge	1^{st} flap	1^{st} edge	1^{st} flap
	at max DF	1^{st} flap	1^{st} flap	1^{st} flap	1^{st} flap
Case 5	at min DF	1^{st} edge	1^{st} flap	1^{st} flap	1^{st} flap
	at max DF	1^{st} flap	1^{st} flap	1^{st} flap	1^{st} flap
Case 6	at min DF	1^{st} edge	1^{st} edge	1^{st} edge	1^{st} flap
	at max DF	1^{st} flap	1^{st} flap	1^{st} flap	1^{st} flap
Case 7	at min DF	1^{st} edge	1^{st} edge	2^{nd} edge	1^{st} flap
	at max DF	1^{st} flap	1^{st} flap	1^{st} flap	1^{st} flap

For all cases and models, the 1^{st} flapwise mode is dominant at the highest DF which is expected for regular oscillations as this is the lowest blade mode. In the cases where an instability is seen to occur, the dominant frequency increases to an edgewise mode. This confirms that it is the edgewise modes becoming unstable.
The 2^{nd} edge mode is dominant five times. Interestingly for the times it is seen in the Steady model there is a phase between the areas of the 1^{st} flap and the 2^{nd} edge mode where the 1^{st} edge mode is dominant. An example of this is seen in Figure 5.4a where two distinct increases in M_{edge} occur. In Øye's model for Case 1 there is a small region where the 1^{st} edge mode is dominant. For the Risø model in Case 7 the dominant mode jumps directly from the 1^{st} flap to the 2^{nd} edge. In general the instabilities predicted by the Risø model, such as in Figure 5.4c, become violently unstable. This results in large M_{edge} values at DF's only slightly lower than the DF where the instability started.

Interestingly, this transition from 1^{st} flap to 1^{st} edge sometimes occurs at higher DF's than the jump in M_{edge}. This would indicate that, even though no instability was detected at the lowest DF, the Risø model is close to being unstable in Cases 1 and 4, both the Øye and Risø models for Case 6 and Snel's model for Cases 2 and 3. To verify this, the relative peak sizes are compared between the edgewise modes and the 1^{st} flapwise mode using Equation 5.3. Here S indicates the magnitude of the peak in the frequency domain.

$$\frac{S_{1^{st}\text{edge}} + S_{2^{nd}\text{edge}}}{S_{1^{st}\text{flap}}} \tag{5.3}$$

The DF is then found where this ratio is equal to 2 and shown in Table 5.7.

Table 5.7: Damping factor where the sum of the peaks for the first two edgewise modes is double that of the first flapwise mode.

Case	Damping factor (Normalized) Steady	Øye	Risø	Snel
Case 1	25	34	-	-
Case 2	94	80	78	-
Case 3	103	112	130	-
Case 4	217	-	-	-
Case 5	190	-	-	-
Case 6	186	38	80	-
Case 7	214	36	29	-

For the Steady model this criterion is seen to give similar results to the $M_{edge} = 2$ intersections in Table 5.5 so this may be a good method for detecting instabilities. However, for the dynamic stall models large differences are seen. This new method gives much larger DF's than as seen in Table 5.5 which is due the dynamic stall models damping the flapwise motions significantly more than the edgewise motions. Therefore, the relative size of the two motions are changed. This is additionally an indication that the direction of vibration could be modified by the dynamic stall models, which could explain some of the large differences between the models.
Despite the changed relative sizes, Table 5.7 still contains useful information. For the Risø model in Cases 1 and 4 and for Snel's model in Cases 2 and 3 the 1st edgewise mode was seen to be dominant in Table 5.6. In Table 5.7, on the other hand, no data is seen due to the ratio of peaks in Equation 5.3 remaining below 2. This indicates that an instability is not necessarily imminent despite the edgewise modes becoming more important at the lowest DF. For Case 6 with the Øye and Risø models, on the other hand, the ratio of peaks are seen to be high enough to reach the ratio of 2. Here the instabilities have already started at the lowest DF's with a sharp increase in M_{edge} being present; however, have not yet reached $M_{edge} = 1$ and so are not in Table 5.5.
In general the dynamic stall models are seen to greatly affect the spectra in both peak magnitudes and frequencies. Each dynamic stall model has a different distribution of damping across the turbine modes and sometimes even causes different turbine modes to be excited. For example the 1st flapwise blade mode can manifest itself in various different symmetrical or asymmetrical turbine modes. The different dynamic stall models sometimes have different turbine modes that are dominant. This results in a shift in the frequency of the peak corresponding to the 1st flapwise blade mode.

5.3.4 Sensitivity Analysis

Next a sensitivity analysis is conducted into the results obtained in the standstill cases to changes in the time constants for the Øye and Risø models. The Øye and Risø models are the only models analysed here as these are the only dynamic stall models that showed an instability start in the range of Damping factors used. Furthermore, only the time constants are varied as the other parameters are related to the attached flow behaviour. These time constants are effective in their inverse as seen in Appendix C so the inverse of the time constants will be

varied by 10% for each of the models. This inverse of the time constant can roughly be seen as the spring stiffness of the ODE's.
The investigation for Øye's model can be found in Section 5.3.4.1 and for the Risø model in Section 5.3.4.2.

5.3.4.1 Øye's model

For Øye's model an increase and decrease of $1/\tau$ by 10% gives the new τ values of 8.89 and 7.27 based on the default value of 8.0. Figure 5.11 shows the effect of these different time constants on one of the hysteresis loops from the 2D comparison chapter (Chapter 4).

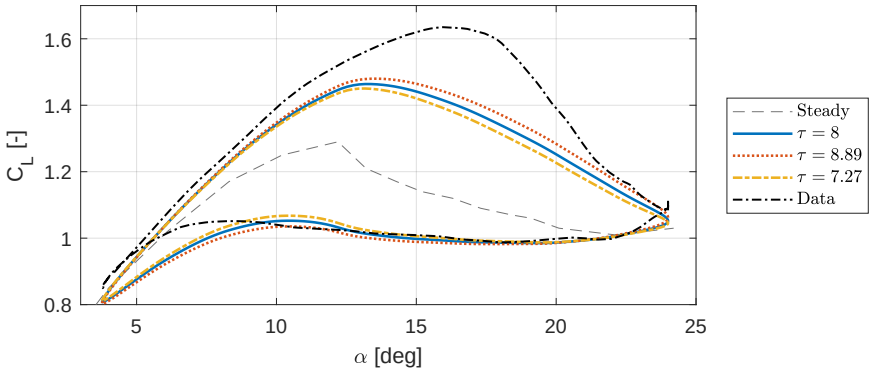

Figure 5.11: Comparison for Øye's model with different τ's on the NACA4415 airfoil where $k = 0.039$, $\alpha_m = 14°$ and $\alpha_a = 10°$

It is seen that, as expected, an increase in the time constant increases the time lag and so causes the hysteresis loop to increase in size.

The sensitivity of the location of the instabilities (Table 5.5) to these changes in τ are shown in Table 5.8.

Table 5.8: Change in Damping factor of the intersection with $M_{edge} = 1$ for different time constants in Øye's model

	$\tau = 7.27$	$\tau = 8.89$
Case 1	-0.5%	0.6%
Case 2	3.6%	-5.6%
Case 3	10.0%	-4.1%
Case 7	187.7%	-

The changes in τ are seen to have little effect in Case 1, which is due this case having two blades operating fully outside and the last oscillating near the edge of the α range where the Øye model causes any dynamic behaviour. This low sensitivity implies that it is the two blades in the fully separated flow region that are most important for the instability and not the blade with an angle of attack around 30°.
For the other cases the decreased value of τ makes the system less stable as larger structural

damping levels are required to prevent the instabilities. This is as expected as the smaller hysteresis loops should reduce the positive damping contribution from the dynamic stall model. Again large differences are seen between Case 2 and 3 indicating that these sensitivities are themselves sensitive to small variations in the wind. Therefore, it may be more rigorous to repeat each case for several wind seeds and use the averages.
Case 7 shows a large sensitivity where the DF at $M_{edge} = 1$ almost triples from 8 to 24 when going from $\tau = 8$ to $\tau = 7.27$. For $\tau = 8.89$ the instability disappears meaning the DF where it occurs has dropped below of the range of the DF's looked into. The opposite happens for Case 6 where for $\tau = 7.27$ the edgewise instability now initiates at DF=15 while for $\tau = 8$ no instability is seen.

5.3.4.2 Risø model

The Risø model has two time constants which are both varied in similar fashion to that of the Øye model. This gives the values of 1.36 and 1.67 for τ_p and 5.45 and 6.67 for τ_f. The outcome of varying these parameters is shown Figure 5.12.

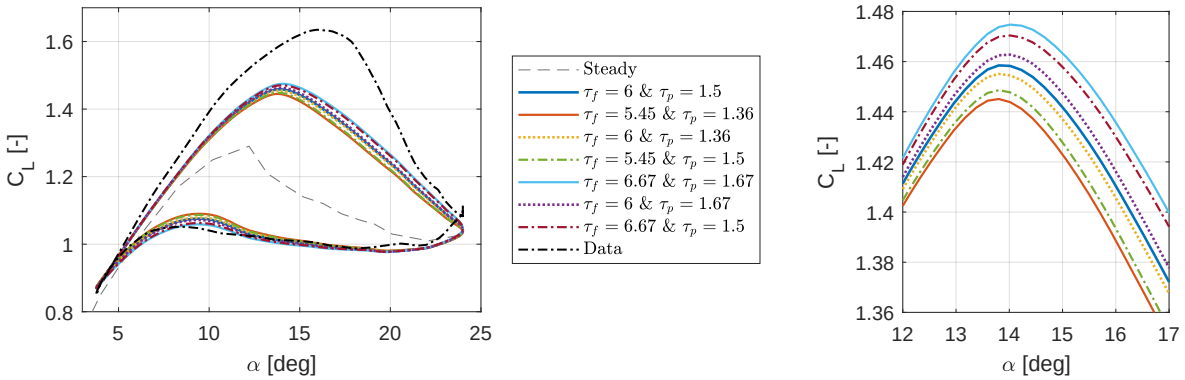

(a) Full loop (b) Zoomed in

Figure 5.12: Comparison for the Risø model with different τ's on the NACA4415 airfoil where $k = 0.039$, $\alpha_m = 14°$ and $\alpha_a = 10°$

As expected a higher time constant increases the unsteady behaviour and makes the loops larger. The effect of the change in τ_f is seen to have a significantly larger effect on the thickness of the loop than τ_p. As these deviations are small, a comparison with larger time constants is made in Figure 5.13 to better see the different effects of each time constant.

This shows that, while τ_p and τ_f both increase the hysteresis effect and move the lift peak to higher angles of attack, they affect the loop differently. When τ_p is changed, the hysteresis loop maintains the same general shape and the lift values at the minimum and maximum α's are the same. τ_f does change the C_L at the edges and, furthermore, makes the loop more circular. The reason for this is that τ_p can be seen as a time delay while τ_f is more a time decay. More specifically, the ODE with τ_p results in f^{st} being shifted to the value of f^{st} at a slightly earlier time. Hereafter, the ODE for τ_f causes f^{dyn} to decay to this lagged f^{st} value. The effect of τ_p can be visualized using Figure 2.2 where on the outgoing loop it shifts the f^{st} curve to the right while on the return loop it shifts it left.

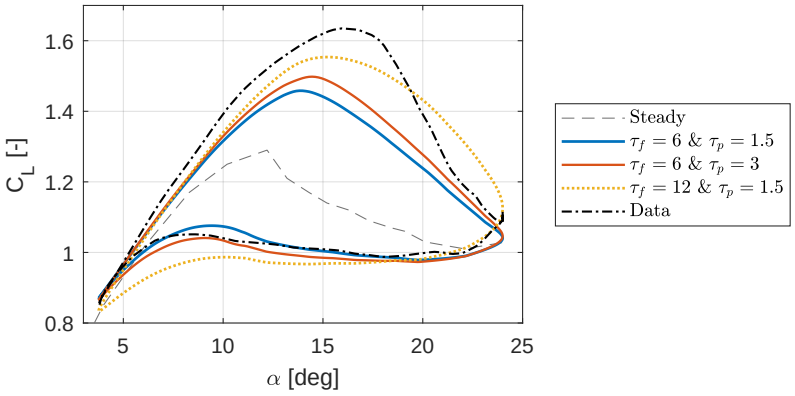

Figure 5.13: Comparison for the Risø model with large τ's on the NACA4415 airfoil where $k = 0.039$, $\alpha_m = 14°$ and $\alpha_a = 10°$

The sensitivity of the location of the instability to the changes in the time constants is shown in Table 5.9.

Table 5.9: Change in Damping factor of the intersection with $M_{edge} = 1$ for different time constant combinations in the Risø model

	$\tau_p = 1.36$ $\tau_f = 5.45$	$\tau_p = 1.36$ $\tau_f = 6.0$	$\tau_p = 1.5$ $\tau_f = 5.45$	$\tau_p = 1.67$ $\tau_f = 6.67$	$\tau_p = 1.67$ $\tau_f = 6.0$	$\tau_p = 1.5$ $\tau_f = 6.67$
Case 2	15.3%	8.3%	10.6%	-5.2%	-2.1%	-2.6%
Case 3	5.2%	2.5%	2.2%	-5.0%	-3.3%	-2.2%
Case 7	6.1%	4.0%	2.0%	-7.5%	-4.1%	-3.9%

Here, similarly to the results from the Øye model in Table 5.8, an increased time lag increases the margin to the instability by decreasing the DF where the instability occurs.
In general, the effect of the change in τ_p is roughly similar to that of τ_f which is surprising based on Figures 5.12 and 5.13 where it was seen that the change in τ_f affects the hysteresis loop more.
Again a large variability is seen between Case 2 and 3. The Risø model is different from the Øye model, though, as for the Risø model Case 2 is more sensitive to a decrease in the time constants, while for Øye's model it is Case 3 that is more sensitive.
For Case 6 no instability is seen with the standard time constants. However, when the τ's are decreased, instabilities are seen at DF=6 when both $\tau_p = 1.36$ and $\tau_f = 5.45$. Furthermore, when only τ_p is decreased, the intersection with $M_{edge} = 1$ is at DF=4. When only τ_f is decreased, this is DF=5. This indicates that the Risø model is indeed on the verge of instability at the minimum DF when using the default coefficients.

Overall this sensitivity analysis shows a large importance of the time constants for these standstill stability cases indicating that they should be estimated as accurately as possible. For the default values it is unknown how well the tuning has been done and to what data, so it is recommended to do a new tuning of these time constants which is done in Chapter 6.

5.4 Flutter speed

Next the effect of the dynamic stall models on classical flutter is investigated. As classical flutter is an attached flow phenomenon where the torsional and flapwise modes interact, it is not expected that the Øye and Snel models will have a significant effect. However, both the Risø and ONERA models include attached flow physics. Adding Theodorsen's equations, and in particular the circulatory effects, should increase the flutter speed based on the literature [20] [44] [47].
The flutter limit is found by letting the turbine initialize normally to a uniform wind speed of 5 m/s. Then the controller and generator are switched off and a wind ramp is used to accelerate the rotor until flutter occurs. All disturbances such as turbulence, wind shear, tilt and tower shadow all are turned off to get a uniform inflow. Furthermore the gravity is set to 0 m/s^2 and the tower made to be stiff. Flutter is defined to be found when the peak-to-peak tip torsional deflection exceeds 0.25° within two periods of the torsional eigenfrequency. The flutter speed is then found by taking the average of the relative wind speed within this two period time frame at 88% along the blade which exceeds this 0.25° criteria. The wind ramp is chosen such that the angle of attack remains roughly constant. In order to increase the accuracy the results from three slightly different wind ramps are averaged.

The results can be found in Table 5.10. Here the flutter speeds themselves are not shown, but rather the differences with respect to the Steady model for confidentiality.

Table 5.10: Change in flutter speed for each model with respect to the case with no dynamic stall model

	Unit	Øye	Risø	ONERA	Snel
ΔU	$[m/s]$	-0.6	10.9	-1.6	-0.4

It is seen that the Øye and Snel models do both slightly decrease the flutter speed despite not having any attached flow behaviour. This is likely due to some of the lift curves not being perfectly linear in the attached flow region so these models still cause a little hysteresis.
The Risø model increases the flutter limit by over 10 m/s which is expected. The ONERA model, however, causes a decrease of 1.6 m/s. This is surprising as the difficulties of obtaining $\dot{\alpha}$ are no issue here as the wind field does not rotate or contain turbulence. Therefore both models should show the attached flow behaviour as in the Verification chapter (Chapter 3), albeit with the heaving contributions to $\dot{\alpha}$ neglected. This is not expected to have a significant effect based on Theodorsen's theory as Lobitz [47] found a low sensitivity to the $\dot{\alpha}$, $\ddot{\alpha}$ and $\ddot{h}$ terms. However, the ONERA model is not completely rigorous in the implementation of Theodorsen's theory. Therefore, this effect of neglecting the contribution to $\dot{\alpha}$ from the heaving motion (the $\ddot{h}$ term in the theory) is briefly looked into by comparing the original heaving plot in Figure 3.2a (repeated in Figure 5.14a) to one where $\dot{\alpha} = 0$ in Figure 5.14b.

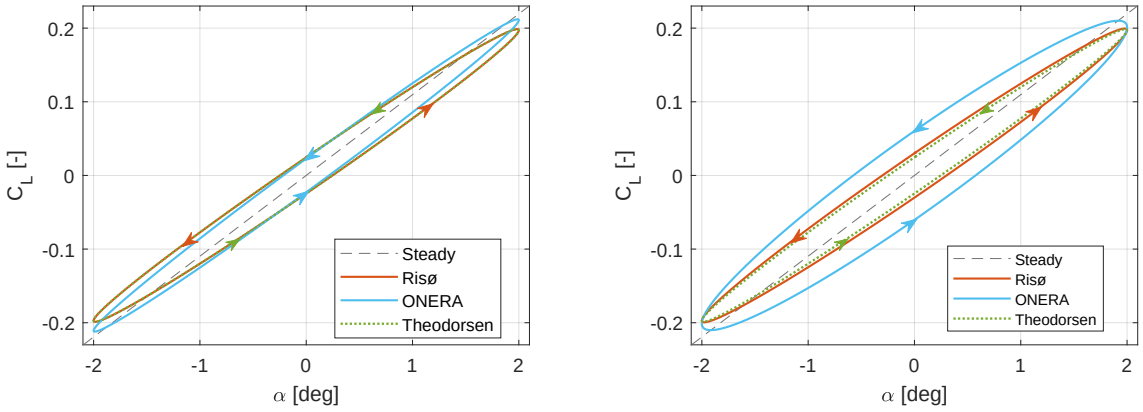

(a) Unmodified $\dot{\alpha}$

(b) $\dot{\alpha} = 0$ for Risø and ONERA

Figure 5.14: Comparison between Theodorsen's function, the Risø and ONERA dynamic stall models where $k = 0.051$ and $\tilde{\bar{h}} = 0.684$ with and without the contribution from $\dot{\alpha}$

For the Risø model the loop becomes slightly thicker than the curve from Theodorsen's theory due to the loss of the added-mass term. For the ONERA model, on the other hand, large changes are seen and the loop is significantly thicker. This is due to the ONERA also using $\dot{\alpha}$ in the forcing component of the circulatory term. Therefore, neglecting $\ddot{h}$ also affects Theodorsen's function, $C(k)$. The flutter speed does have a large sensitivity to $C(k)$ [47] due to shifting the phase between the lift and moment forces.
Another difference between the models is that for the pitching motion C_L hysteresis loop the ONERA model is slightly underrotated with respect to Theodorsen and the Risø model which again will result in a slightly modified $C(k)$ and a different phase. These phase differences can change the flutter limit in either direction, so could be the cause of this unexpected behaviour. The drag coefficient is additionally different between the Risø and ONERA models. Although, the edgewise vibrations are smaller than those in the flapwise direction before the flutter limit.

CHAPTER 6

Tuning

In this chapter it is attempted to tune the Øye and Risø models to various cases in the measurement set used in the 2D comparison in Chapter 4 by changing the time constants of the dynamic stall behaviour and, for Øye's model only, the fully separated lift polar C_L^{sep}. First the method and cases used to tune the models is detailed in Section 6.1. This is then followed by the results in Section 6.2 and a discussion in Section 6.3.

6.1 Method

As mentioned the models are tuned the data in Chapter 4. The chosen cases and their weights are listed in Table 6.1 in order of appearance in Chapter 4. There are two cases with a weight of zero indicating that these cases do not contribute to the tuning. They will be used as an independent check for the tuning results and are additionally used in the individual tuning. The individual tuning is where the models are tuned to each case individually to determine how much the optimum parameters vary over the cases.
The weights and used cases are selected with a focus on the light and moderate stall regions where no clear leading edge stall behaviour is present. Furthermore one deep stall case and one ramp case are included. As the ramp case does not decay back to the steady values at the end and it is not certain if this is physical or a measurement error, only the first 70 non-dimensional time units are considered for the tuning.
For two cases the drag and moment coefficients are included in the tuning for the Risø model. These coefficients are given a weight of 0.1 with respect to the weight of the lift coefficient.

Table 6.1: Used cases for the tuning together with their weights

Case Number	Figure Number	Airfoil	k	α_m	α_a	Weight	Use C_D and C_M
1	Fig. 4.3	NACA0015	0.051	10°	6°	0	no
2	Fig. 4.4	NACA0030	0.051	10°	6°	0.15	no
3	Fig. 4.5	NACA4415	0.037	8°	5°	1	no
4	Fig. 4.6	NACA0015	0.051	10°	10°	0	no
5	Fig. 4.7	NACA0030	0.051	10°	10°	0.1	no
6	Fig. 4.8	NACA4415	0.056	8°	10°	0.5	yes
7	Fig. 4.9	NACA4415	0.019	8°	10°	1	no
8	Fig. 4.11	NACA4415	0.039	14°	10°	1	yes
9	Fig. 4.16b	NACA0030	Ramp			0.1	no

For each of the cases with a non-zero weight the optimization function runs the model to generate the hysteresis loops and then the l^1-norm is taken of the difference between the model

and the data. This norm is calculated as l^1-norm $= \frac{1}{N}\sum_{k=1}^{N}|v_k|$ where v_k is the vector with the differences between the model prediction and the data. N is the length of this vector. It is chosen to use the l^1-norm instead of the l^2-norm (as used in Chapter 4) to try to improve the full hysteresis loop rather than focusing on the areas where the error is the largest, because often an improvement in one area will reduce the accuracy in another.
The optimizer used is the `lsqnonlin` function in Matlab for the overall tuning where again the l^1-norm is used rather than the l^2-norm which is achieved by taking the square root of the residual vector in the tuning function. For the individual tuning of each case it is not possible to use `lsqnonlin` as the residual will then be a scalar. Therefore, the system will be underdetermined if trying to solve for more than one variable, so the `fmincon` function is used for the individual tuning.

The Øye model is tuned two separate times, first with only the time constant τ as a variable and then with the fully separated lift curve, C_L^{sep}, additionally tunable. C_L^{sep} is made tunable through changing the slopes of the Hermite Interpolation polynomial at α_0 and α_{sep}. By default these slopes are $\frac{1}{2}\left.\frac{dC_L^{st}}{d\alpha}\right|_{\alpha_0}$ at α_0 and $\frac{1}{12}\left.\frac{dC_L^{st}}{d\alpha}\right|_{\alpha_0}$ at α_{sep} [8]. To make these slopes variable the fraction in front of the linear lift slope is renamed to a_{α_0} and $a_{\alpha_{sep}}$ for the derivative at α_0 and α_{sep} respectively such that by default $a_{\alpha_0} = \frac{1}{2}$ and $a_{\alpha_{sep}} = \frac{1}{12}$.
The optimization is constrained to prevent unphysical solutions. All time constants are allowed to range between 0.1 and 50 while for C_L^{sep} the limits are $\frac{1}{4} \leq a_{\alpha_0} \leq \frac{3}{4}$ and $-\frac{1}{4} \leq a_{\alpha_{sep}} \leq \frac{1}{4}$.
As an extra investigation the Risø model is also tuned a second time with the extra constraint that $\tau_p \leq 3$ to maintain consistency with the default parameters where $\tau_f > \tau_p$ as it is found that without this tighter constraint τ_p will become relatively large.

6.2 Results

In general the tuning results in an increase in the time constants as shown in Table 6.2. This is expected as the models generally showed less hysteresis than the data in Chapter 4.
Interestingly the tuned τ value of 10.03 in the Øye model is almost identical to the default τ of 10 for the Øye model in HAWC2 [19]. HAWC2 does, however, use a different method of estimating the C_L^{sep} polar. The large difference between the tuned τ's between the cases where C_L^{sep} is and is not included in the tuning indicates that this C_L^{sep} is important to consider in the tuning and care should be taken if using these τ's with different C_L^{sep} curves.
Interestingly, in the Risø model the tuning results in a much larger τ_p while τ_f actually decreases. The effect of each of these time constants is shown in Figure 5.13 in Section 5.3.4.2 and indicates that the tuned hysteresis loops will have a more triangular shape with a sharper drop at stall. This is possibly due to the possible presence of mixed trailing and leading edge stall in some of the cases which will result in a sharper drop after the peak lift coefficient than if the stall were purely trailing edge stall. No cases with dominant leading edge vortex behaviour are used in the tuning.

Table 6.2: Overall tuning results

	Øye (τ only)	Øye (τ and C_L^{sep})			Risø		Risø ($\tau_p \leq 3$)	
	τ	τ	a_{α_0}	$a_{\alpha_{sep}}$	τ_p	τ_f	τ_p	τ_f
Default	8.00	8.00	0.500	0.083	1.50	6.00	1.50	6.00
Tuned	10.03	11.51	0.733	0.021	7.45	3.98	3.00	7.92

6.2.1 Øye

For the Øye model the residuals for each case at the start of the tuning (the default parameters) are compared to the residuals at the end (the tuned parameters) in Figure 6.1. The overall value to be minimized is the l^1-norm of these residuals.

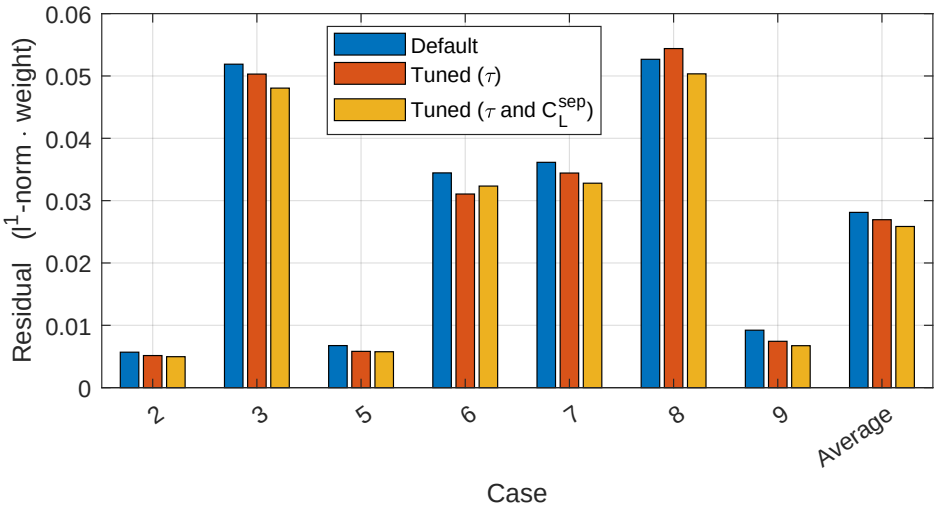

Figure 6.1: Residual magnitude for each case together with the average after tuning the Øye model for τ only and for both τ and C_L^{sep}

Overall the improvements to the residuals are small with no large changes anywhere. There is a general improvement when tuned using both τ and C_L^{sep} over when only tuned with τ. This is expected as the optimizer now has more freedom to find a better optimum.
The independent Cases 1 and 4 additionally show an improved l^1-norm fit to the data when the tuned values are used, despite not being used in the tuning. For Case 1 the improvement is 0.009 and 0.014 when tuning to τ only and to both τ and C_L^{sep} respectively. This decrease in residual is 0.007 and 0.005 for Case 4.
When only tuned to τ, Case 8 actually shows an increased residual. To see what is occurring here the hysteresis loops resulting from the tuning are shown in Figure 6.2 and 6.3 for the tuning to only τ and to both τ and C_L^{sep} respectively. Here the overall tuning results are shown in addition to optimum hysteresis loop if the case was tuned individually. Extra attention should be paid to the phase plots as these are what the optimizer uses. The optimum parameters from the individual tuning are shown after the figures in Table 6.3.

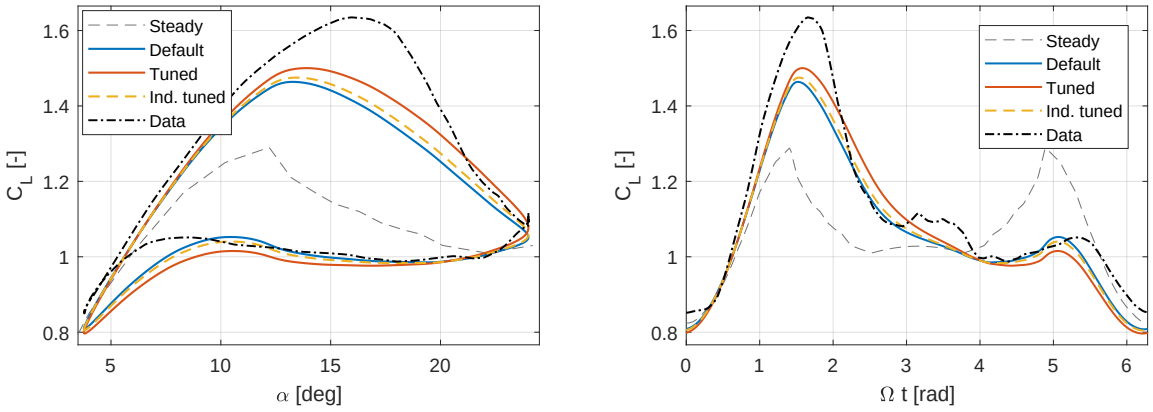

(a) C_L vs α (b) C_L vs Phase

Figure 6.2: Comparison of the overall and individual tuning results for the Øye model for Case 8 when tuning only τ

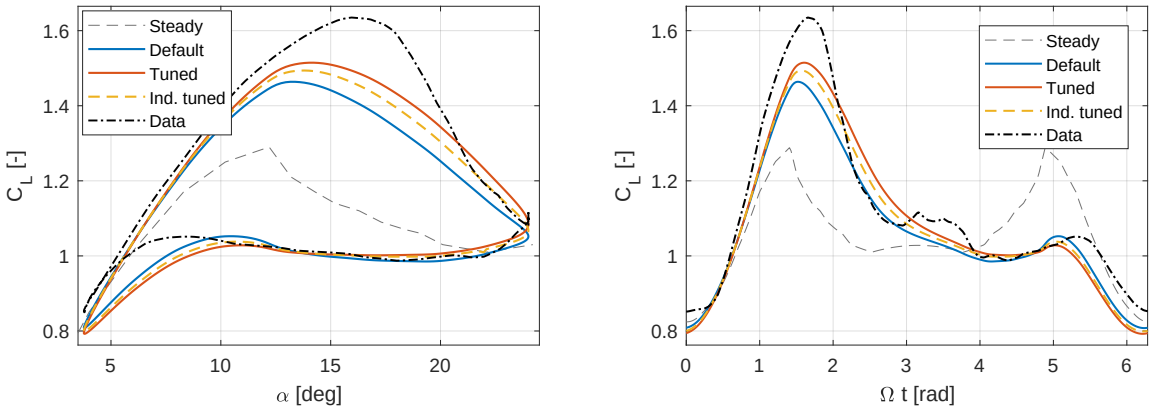

(a) C_L vs α (b) C_L vs Phase

Figure 6.3: Comparison of the overall and individual tuning results for the Øye model for Case 8 when tuning both τ and C_L^{sep}

In the case that only the time constant is increased, then the detachment part of the hysteresis loop is raised; however, the reattachment part of the loop has a lower C_L. When looking at the phase plot in Figure 6.2b it is seen that the improvement from the overall tuning is only for some parts of the detachment (roughly in the ranges $1.5 < \Omega t < 2$ and $3 < \Omega t < 4$) while the full reattachment has a decreased accuracy.
When tuned for both τ and C_L^{sep} the combination of the larger a_{α_0} together with the lower $a_{\alpha_{sep}}$ will raise C_L^{sep} along it's full length. This will also result in the whole hysteresis loop begin shifted up which allows for a larger time constant to be used without sacrificing in accuracy on the reattachment. This additionally explains why τ is larger when tuned for both τ and C_L^{sep} rather than only τ.

To learn more about how each case differs and how each case affects the overall tuning, the optimum parameters for each case are calculated individually and shown in Table 6.3.

Table 6.3: Results from the individually tuning of each case for the Øye model

	Øye (τ only)	Øye (τ and C_L^{sep})		
	τ	τ	a_{α_0}	$a_{\alpha_{sep}}$
Default	8.00	8.00	0.500	0.083
Tuned	10.03	11.51	0.733	0.021
Case 1	31.61	32.32	0.746	0.240
Case 2	17.96	17.62	0.258	0.249
Case 3	13.33	14.37	0.750	-0.248
Case 4	12.24	11.82	0.254	0.242
Case 5	15.96	15.27	0.250	0.249
Case 6	11.02	10.56	0.260	0.234
Case 7	9.93	12.96	0.749	-0.248
Case 8	8.62	10.08	0.675	0.033
Case 9	14.05	13.14	0.254	0.245

All cases have optima with a τ larger than the default value, indicating that this value may be conservative. Case 1 is an outlier when compared to the rest with an optimum τ of over 30. Therefore this may be a faulty measurement.
When additionally tuning for C_L^{sep} it is seen that the optimizer often pushes the slope ratios close to the constraints. This does not necessarily have a large effect as shown for Case 7 in Figure 6.4 when comparing the overall tuned loop to that of the individually tuned loop.

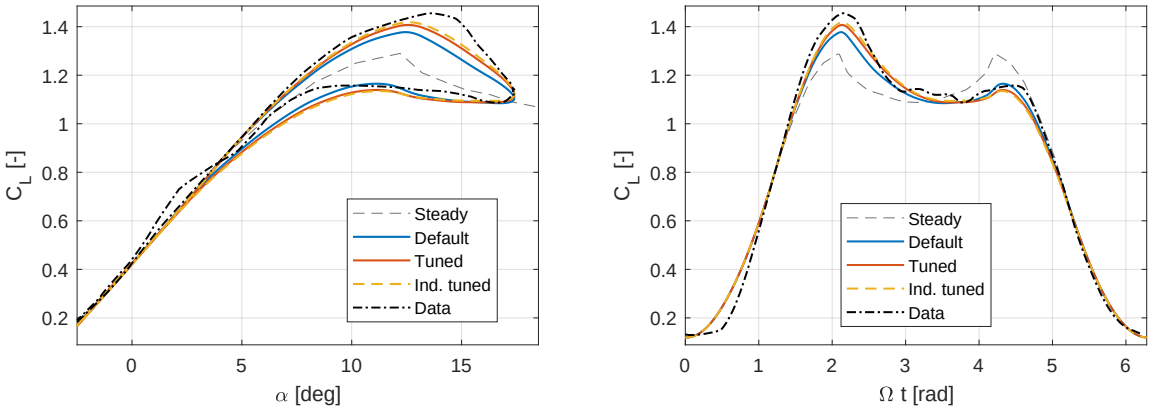

(a) C_L vs α (b) C_L vs Phase

Figure 6.4: Comparison of the overall and individual tuning results for the Øye model for Case 7 when tuning both τ and C_L^{sep}

The negative $a_{\alpha_{sep}}$ in the Ind. Tuned curve only results in the hysteresis loop being slightly moved up at the higher angles of attack.

When comparing the overall tuned loop to that of Case 8 in Figure 6.3, it is seen that again the thickness of the hysteresis loop is increased, the part of the loop going into stall has an improved fit and the return part has a decreased accuracy. Overall the magnitude of the residual is decreased as the improvement on the outgoing part is larger than the loss in accuracy on the return part.

6.2.2 Risø

The residuals for the Risø case are shown in Figure 6.5 where the original tuning results are shown together with the results with the added constraint of $\tau_p \leq 3$.

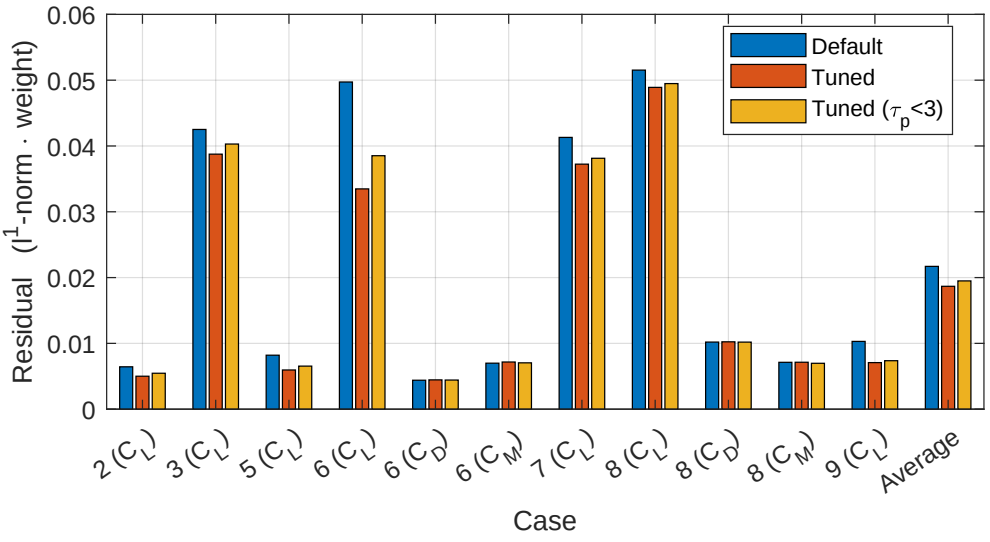

Figure 6.5: Residuals distribution over each case together with the average after tuning the Risø model

This shows that the tuning has almost no effect on the drag and moment coefficients. For the lift coefficients the optimizer has more success in minimizing the residual when it is less constrained, although the difference is small with the exception of Case 6. This case additionally has the largest improvement from the tuning. To understand why the C_L vs α plots for this case are shown in Figure 6.6.

Here the tuned loop shows a significantly higher peak lift coefficient and has an better reattachment. These improved properties are also present when the extra constraint of $\tau_p \leq 3$ is added; however, are less pronounced.

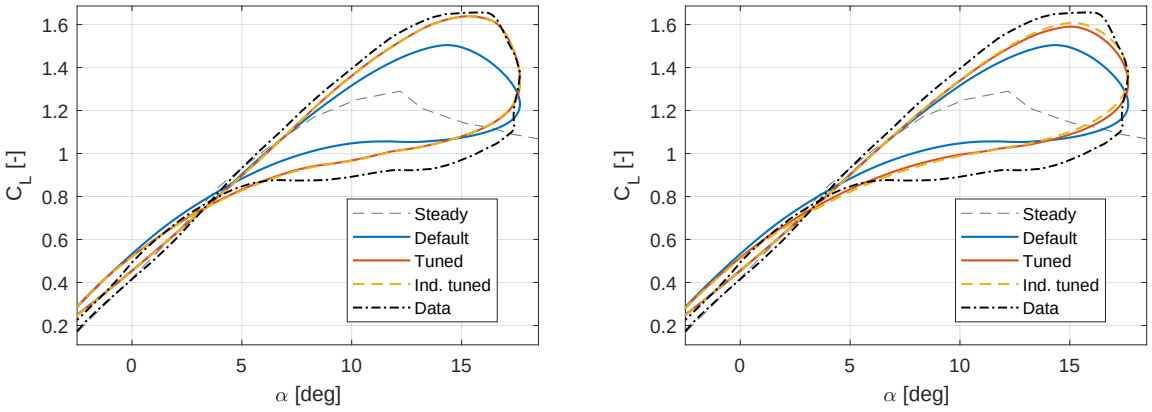

(a) Risø (b) Risø ($\tau_p \leq 3$)

Figure 6.6: Comparison of tuning results for the Risø model for Case 6

Cases 1 and 4 are again used as independent test cases. For the Risø model Case 1 shows a decrease in residual of 0.028 and 0.022 for the normal tuning and for when $\tau_p \leq 3$ respectively. For Case 4 this is 0.034 and 0.020 respectively.

As in the tuning for Øye's model, the effect of the tuning on Case 8 is shown in Figure 6.7 for the Risø model with the normal constraints and in Figure 6.8 with the extra constraint on τ_p.

This shows the differences between the two tuning results. Without the $\tau_p \leq 3$ constraint the peak lift and following drop in lift is captured better, although accuracy is sacrificed on the reattachment. The individually tuned curves are identical in Figures 6.7 and 6.8, because the optimum already has $\tau_p \leq 3$ in this case as shown in Table 6.4.

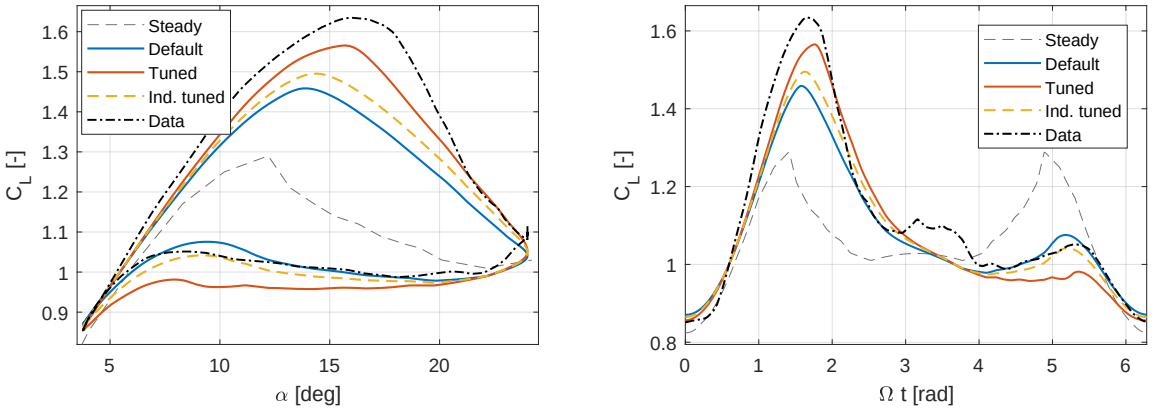

(a) C_L vs α (b) C_L vs Phase

Figure 6.7: Comparison of tuning results for the Risø model for Case 8

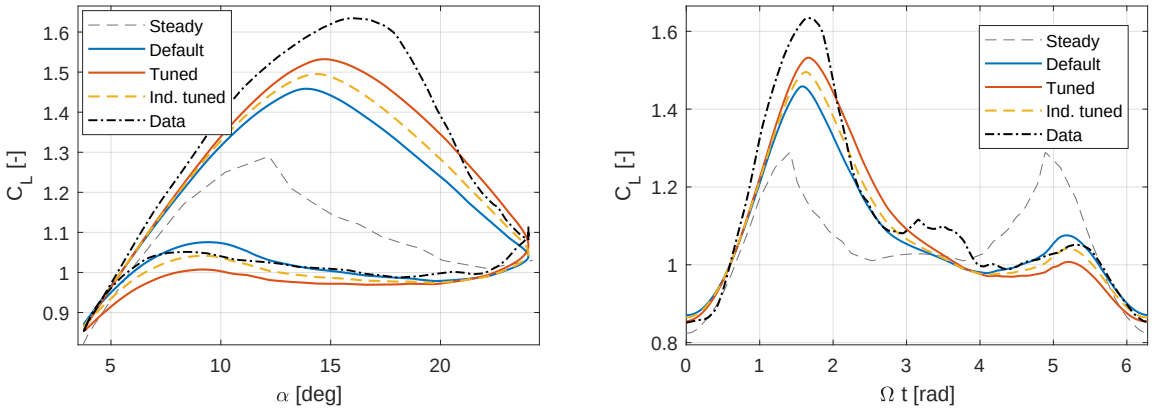

(a) C_L vs α (b) C_L vs Phase

Figure 6.8: Comparison of tuning results for the Risø model for Case 8 with $\tau_p \leq 3$

The results from the individual tuning of the Risø model are listed in Table 6.4.

Table 6.4: Results from the individually tuning of each case for the Risø model

	Risø		Risø ($\tau_p \leq 3$)	
	τ_p	τ_f	τ_p	τ_f
Default	1.50	6.00	1.50	6.00
Tuned	7.45	3.98	3.00	7.92
Case 1	2.06	23.61	2.06	23.61
Case 2	4.85	10.90	3.00	14.77
Case 3	12.97	0.12	2.91	10.37
Case 4	8.72	4.01	3.00	9.95
Case 5	8.76	5.85	3.00	12.34
Case 6	6.99	4.56	3.00	8.95
Case 7	11.08	0.17	0.30	9.95
Case 8	2.52	6.53	2.52	6.53
Case 9	11.89	3.14	3.00	10.92

Again large differences in optimum time constants are seen between the cases. The large swings sometimes seen between τ_f and τ_p don't always result in significant changes in the loop. For example Case 7 gives a τ_f that is almost 0 and a relatively large τ_p although the resulting change in dynamic stall behaviour with respect to the overall tuned results is minimal, as shown in Figure 6.9a.

The main differences are that the drop in lift just before $\alpha = 15°$ is sharper and there is a bump in the reattachment near $\alpha = 10°$. This sharpness is due to τ_p being negligible while this is the time constant that gives the smoothing. τ_f only delays the angle of attack that the underlying f^{st} is called at and therefore will result in the point of stall being shifted to larger α's and reattachment to lower α's.
In Figure 6.9b the tuning results for Case 7 are shown with the constraint in τ_p. Now it is τ_p

that is almost 0 and τ_f that is large for the individual tuning, which results in a very smooth lift peak and stall behaviour.

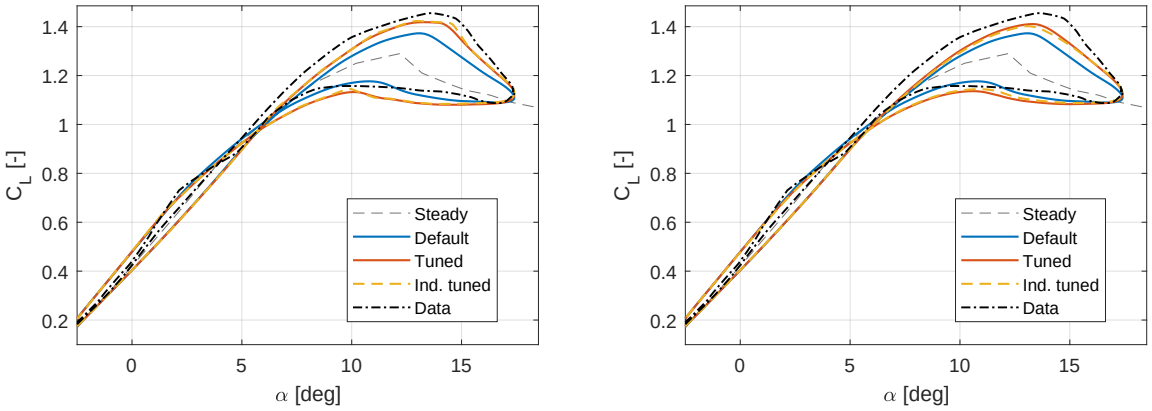

(a) Risø (b) Risø ($\tau_p \leq 3$)

Figure 6.9: Comparison of tuning results for the Risø model for Case 7

6.3 Discussion

This tuning is by no means perfect and there are many areas which could be improved. First off the data set used is relatively small. Both the OSU and Glasgow University measurement series contain far more measurements than used here which could be used to improve the tuning. Furthermore, the tuning is done at a single Reynolds number which could potentially reduce the accuracy if these tuned time constants are used at different Reynolds numbers. On top of this, the weights do heavily favour the NACA4415 airfoil with the NACA0015 not contributing to the tuning at all. The use of more airfoils would make the results more valid over a larger range of the blade length.

One important thing to note about the data is that the angle of attack input to the data differs slightly from that to the models as shown in Figure 3.6 in Section 3.3. While the models see a perfect sin wave, in the measurement the true angle of attack is slightly noisy and is slightly flattened at the peak angle of attacks. This means that while at the same phase angle both the model and the data may see different angles of attack. Furthermore there may be a slight constant phase shift over the whole loop as the sin wave used for the models is fit to the data angles of attack through least squares fitting to optimally match the phases. This is not the case for the ramp function as here the angle of attack as measured in the experiment is used. Another issue with the measurement data is that for Case 3 the data is potentially shifted slightly upwards which will affect the l^1-norm while Case 3 contributes heavily to the tuning as it is one of the most relevant cases to normal turbine operation.

The large differences in the results of the individual tuning for each case could be due to there being a large uncertainty in the measurement data. Another explanation is that the models do not capture enough of the physics of dynamic stall to properly account for the differences between the cases.

Furthermore, it should be tested if different starting points to the optimization give the same results. In particular for the tuning of the Risø model this is a potential issue as τ_f and τ_p both affect the loop in roughly similar ways. Therefore, depending on the Jacobians in the first iterations, the optimizer may end at a local minimum with for example $\tau_f < \tau_p$, while the global minimum may be for $\tau_f > \tau_p$. That τ_f and τ_p are almost interchangable can cause large shifts in magnitude between the time constants for marginal accuracy improvements.

Finally, the extra freedom given to the optimizer by allowing for C_L^{sep} to be modified in Øye's model could potentially also improve the fit of the Risø model. This is because the Risø model is similar to Øye's model in that the hysteresis loop of the data is often shifted up with respect to that predicted by the models. Therefore, a higher C_L^{sep} curve could reduce the overall residual further.

CHAPTER 7

Conclusion

In this chapter Section 7.1 summarizes the main results and answers to the research questions. Section 7.2 then presents some recommendations for future work.

7.1 Conclusion

Dynamic stall is seen to be a complex phenomenon that is difficult to model accurately and robustly over a wide range of conditions. None of the models showed a perfect match to the data; however, all models greatly improved the fit with the data with respect to the steady lift curve.
Of the four models implemented, the Øye, Risø, Snel and ONERA models, only the Risø and ONERA models simulate the unsteady behaviour in attached flow and the dynamic drag and moment coefficients. Both models showed good agreement with Theodorsen's theory with the Risø model performing better for the lift coefficient.
The 2D comparisons showed that the models all have different strengths and weaknesses. Øye's model is, in general, strongest for the thickest airfoil, the NACA0030. The Risø model has similar behaviour to the Øye model, with the difference that the lift peak is slightly improved due to the figure-8 behaviour from the attached flow physics. The ONERA model captures the lift peak the best, although predicts a too large drop in lift after this peak. This results in it usually having the largest least squares error with the data. When compared respect to the other models, Snel's model has a slightly larger lift hysteresis parameter, quicker reattachment and a stronger scaling of the thickness of the loop into deep stall. In most cases the larger lift hysteresis parameter improves the fit with the data; however, the reattachment is often too quick and the scaling causes the model to show unphysical behaviour outside the design range of the model.
For the drag and moment coefficients the Risø model performs best in the attached flow and light stall conditions. The ONERA model shows hysteresis loops for the dynamic drag that even decrease the accuracy over the steady coefficients. Further into stall though, the ONERA model is often superior. Both models do struggle to reliably predict the shape of the moment coefficient hysteresis loop in stall.

In the extreme load case of IEC DLC 1.4 (Coherent wind gust with direction change), the Øye, Risø and Snel models are seen to perform similarly, with Snel's model giving the largest peak lift. The ONERA model, on the other hand, shows a small lift overshoot and unusual hysteresis behaviour. This is due to the combination of the large model dependence on the time derivative of the angle of attack and the method of approximating the turbulence free value of this derivative in the aeroelastic code.
In the standstill instability cases, Snel's model provides the largest amount of positive damping to the system. No instabilities are seen in any of the cases even when the blades structural damping is set to lowest level. This is a completely different behaviour than that seen in the

Øye and Risø models, despite these models showing similar behaviour in the 2D comparison. Therefore, this large damping from Snel's model is possibly not physical. The Øye and Risø models still provide a large amount of aerodynamic damping as the structural damping can always be reduced by at least a factor of 2 with respect to the case without any dynamic stall model before any unstable activity starts to occur. Of these two models, the Øye model generally provides the largest amount of damping. Finally, the ONERA model actually adds negative damping, which is seen as unphysical.
When evaluating classical flutter, the Øye and Snel models show a limited effect due to not modeling attached flow. The Risø model shows the expected behaviour from the implementation of Theodorsen's theory, namely an increase in the flutter speed, while the ONERA model decreases the flutter limit.
Overall the Risø model is seen as the best for use in an aeroelastic code, despite not always being the best in the 2D lift coefficient comparisons. It is seen to be robust, accurate in attached flow and provides the dynamic drag and moment coefficients. The Øye model is also seen to be robust and, in general, it shows similar dynamic stall behaviour to the Risø model, although it lacks the attached flow physics. Snel's model performed well in the 2D comparison, but showed unexpected behaviour in the instability comparison which is likely to be unphysical. The ONERA model broke down in the aeroelastic code due to relying too heavily on the time derivative of the angle of attack.

7.2 Recommendations

The flaws seen in the Snel and ONERA models could potentially be solved with some modifications to the models. For Snel's model it is predicted that this behaviour is due to the poor scaling of the model into deep stall with large reduced frequencies. This is a flaw that could be remedied with small updates to the model. For example, in this thesis a limit was introduced for the $\dot{\alpha}$ in the spring stiffness and a similar limit could be applied to $\Delta\dot{C}_L^{pot}$ to prevent the forcing term becoming excessive.
The ONERA model broke down in the aeroelastic code mostly due to the simplifications made in the implementation of the $\dot{\alpha}$ terms in the code. However, even if the implementation was perfect, the ONERA model still would have showed the incorrect counter-clockwise reverse C_L loops in the range 20° to 40° as in Figure D.7 which are harder to solve. Phasing the attached flow physics out (i.e. reducing the deviation of $C_{L,1}$ from C_L^{pot}) in stall helps; however, this changes the shape of the normal hysteresis loops (Such as those in Chapter 4) which is not desirable. Unfortunately, any fix to this behaviour of the ONERA model will affect these hysteresis loops and will require a retuning of the model parameters.

Even without making any changes, improvements can likely be made to all models by choosing parameters more suited to wind turbine airfoils. Here the 'average' or flat plate values are used while wind turbine airfoils are relatively thick and specialized. In the Risø model, this gives the strange situation where flat plate values are used for the attached flow physics, while for dynamic stall the leading edge vortex has been neglected based on the assumption of a thick airfoil.

For further analysis it is recommended to look into the Beddoes-Leishman model as here the Risø model showed the most promise. Without the assumptions of incompressible flow and

no leading edge stall the Beddoes-Leishman model may perform better than the Risø model. Although it should be thoroughly checked to see if the robustness of the model is affected with the increased complexity and three more empirical parameters than the Risø model.
In addition to the incompressibility and leading edge stall assumptions, more improvements could potentially be made to the dynamic stall models. For example, the effects of the Reynolds number and the Coriolis or centrifugal forces on the boundary layer development could be considered. However, in particular in the standstill cases, the 2D assumption in the models will likely be the largest contributor to the error with the following being important:

- The effect of spanwise flow due to for example sweep, yaw error or even coning and rotor tilt could be analysed. Having a large spanwise flow across the blade will greatly affect both static and dynamic stall.
- The 3D nature of stall itself could cause the assumption of radial independence to be violated. If, for example, two annuli are close together and are in different phases in the hysteresis loop due to seeing different angle of attack inputs. Then stall will occur at different times and these neighbouring sections could influence each other on the timing of separation or reattachment.
- The tip vortex can have an impact on the dynamic stall loops through changing the local velocity and pressure distributions. Although this effect is only pronounced near the tip.

More broadly the analysis in the aeroelastic code could be built on by considering the following:

- The direction of vibration is an important part of the negative aerodynamic damping from the static curve at certain angles of attack and is not looked into in this thesis. It could possibly be affected by the dynamic stall models because they change the magnitude and phase of the forces.
- A comparison with field tests for full turbines could be made for the standstill cases to see if there are any specific conditions where the turbine shows an instability. Then this could be compared to the results from the aeroelastic code and the damping factors compared where the data is matched the best for each model.
- The aerodynamic damping could be estimated directly instead of indirectly through varying the structural damping. For example, by setting the structural damping to zero, exciting the blade and looking at the immediate logarithmic decrement after release.
- Wind tunnel tests (or computational fluid dynamics simulations) with stochastic α and velocity inputs could be made to further test the models. Perhaps the airfoil could be mounted with a 1D translatory freedom to determine the conditions when the aerodynamic damping becomes negative. This will additionally help determine if the behaviour of Snel's model gives unphysical results as suspected from the standstill cases.
- As the approximation of the first time derivative of the angle of attack is causing issues for the ONERA model and reducing the accuracy of the attached flow physics in the Risø model in the aeroelastic code, perhaps a better method could be used to still account for changes in the wind direction in the pitching velocity without feeding the noise from turbulence being fed to the dynamic stall models. One possibility is to filter the turbulence out using temporal and/or spacial smoothing. Although this may introduce a time delay into this pitching velocity which is undesirable.

APPENDIX A

Hermite Interpolation

For the fully separated C_L curve in the Øye model Hermite Interpolation is used to generate a polynomial between starting and ending point where not only the values, but also the first derivatives are known. The general formulation for this interpolation between $[x_0, y_0]$ and $[x_1, y_1]$ where the derivatives are noted as $\frac{dy}{dx}\Big|_0$ and $\frac{dy}{dx}\Big|_1$ respectively is in Equation A.1 . Furthermore for simplicity y_0 has already been set to zero as it will be $C_L^{st}|_{\alpha_0}$. For ease of notation two new variables are introduced:

$$t_0 = \frac{x - x_0}{x_1 - x_0} \qquad \text{and} \qquad t_1 = \frac{x - x_1}{x_1 - x_0} \tag{A.1}$$

$$y(x) = \frac{dy}{dx}\Big|_0 (x_1 - x_0)(t_0 + (t_1 - 1)t_0^2) + \frac{dy}{dx}\Big|_1 (x_1 - x_0)t_0^2 t_1 + y_1 t_0^2(1 - 2t_1) \tag{A.2}$$

Now using $x_0 = \alpha_0$, $\frac{dy}{dx}\Big|_0 = \frac{1}{2}\frac{dC_L^{st}}{d\alpha}\Big|_{\alpha_0}$, $x_1 = \alpha_{sep}$, $y_1 = C_L^{st}(\alpha_{sep})$ and $\frac{dy}{dx}\Big|_1 = \frac{1}{12}\frac{dC_L^{st}}{d\alpha}\Big|_{\alpha_0}$ gives

$$t_0 = \frac{\alpha - \alpha_0}{\alpha_{sep} - \alpha_0} \qquad \text{and} \qquad t_1 = \frac{\alpha - \alpha_{sep}}{\alpha_{sep} - \alpha_0} \tag{A.3}$$

$$C_L^{sep}(\alpha) = t_0 \left[(\alpha_{sep} - \alpha_0)\frac{1}{2}\frac{dC_L^{st}}{d\alpha}\Big|_{\alpha_0} \left(1 + t_0\left(\frac{7}{6}t_1 - 1\right)\right) + C_L^{st}(\alpha_{sep})t_0\,(1 - 2t_1)\right] \tag{A.4}$$

This function will only be used between α_0 and α_{sep} as above this region the steady lift curve is used for C_L^{sep}.
An example of the resulting curve is shown in Figure 2.2 in Section 2.2.

APPENDIX B

Flowcharts

B.1 Øye

The first flowchart is that of the Øye model in Figure B.1. In all the flowcharts the time independent variables such as chord length, α_0 or α_{sep} have been left out as they only need to be initialized once at the start of the time series.

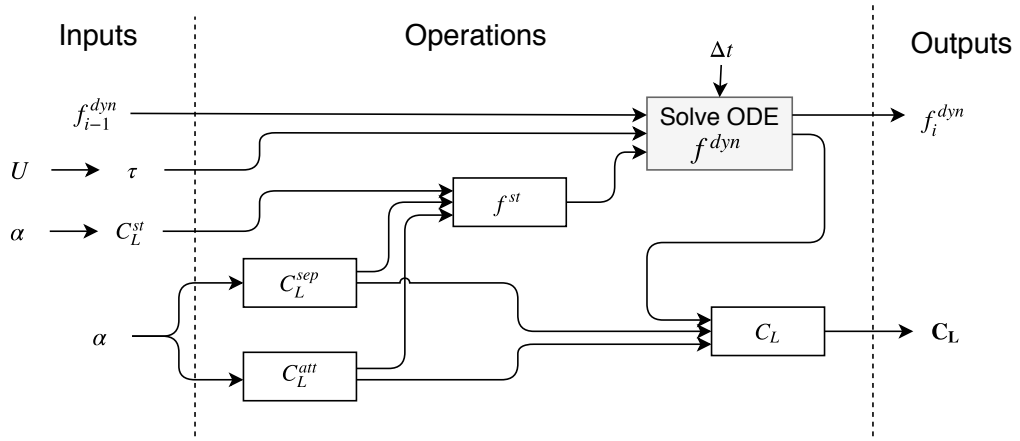

Figure B.1: Øye model flowchart

This shows this is indeed a simple model with few building blocks. This will result in fast computational times. This may, however, come at a sacrifice in accuracy.

B.2 Risø

This model is the most complex as is immediately obvious from Figure B.2.

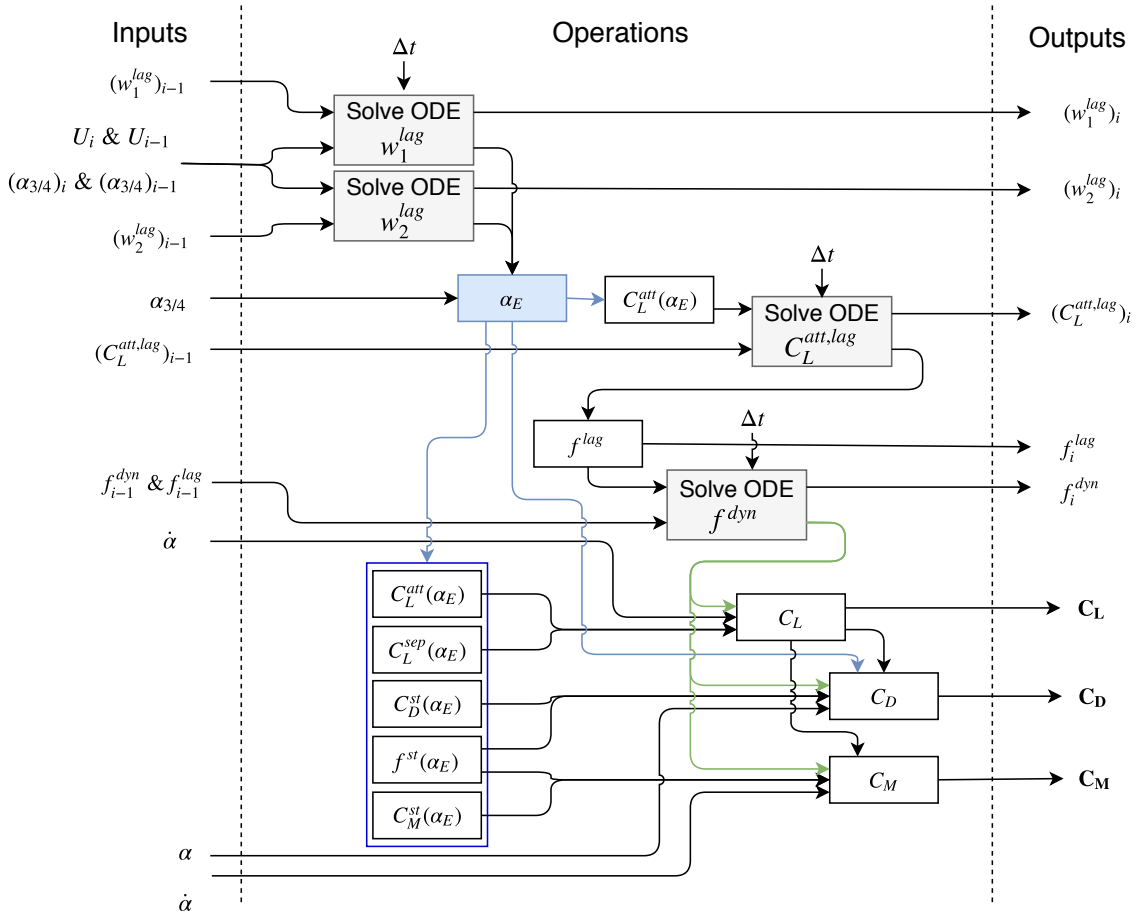

Figure B.2: Flowchart for the Risø model

The model has a cascading flow from the top left to the bottom right where each ODE is dependent on those before it resulting in a complex system with a chain of dependencies. The effective angle of attack is marked in blue to highlight that it is a key parameter that lies at the core of the model. The output of the last ODE, f^{dyn} is marked in green to show that it is used in all three force coefficients.

B.3 Snel

This dynamic stall model seems to be simple based on the flow chart in Figure B.3; however, the intricacies of this model are not in the equations, but rather in the coefficients used.

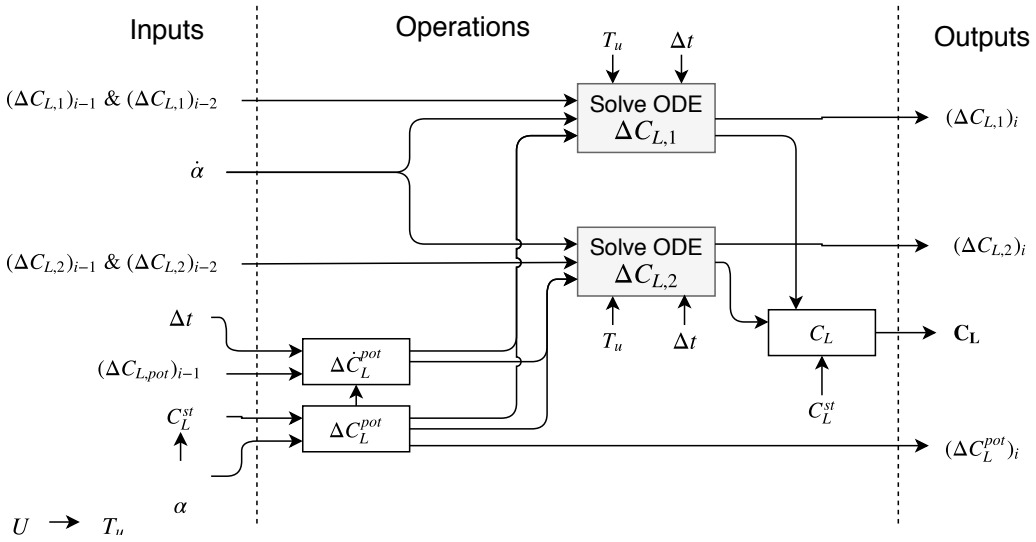

Figure B.3: Flowchart for Snel's model

B.4 ONERA

Finally the flowchart for the ONERA method is shown in Figure B.4.

From the flowchart it can be seen that there are not many equations in total, although each equation has many inputs. The ΔC_L^{pot}, indicated in blue, is used in almost very equation as it is used to indicate how far the airfoil is into stall. The ODE's for the different force and moment coefficients are not interlinked which makes any possible tuning easier as it is possible to tune each coefficient individually.

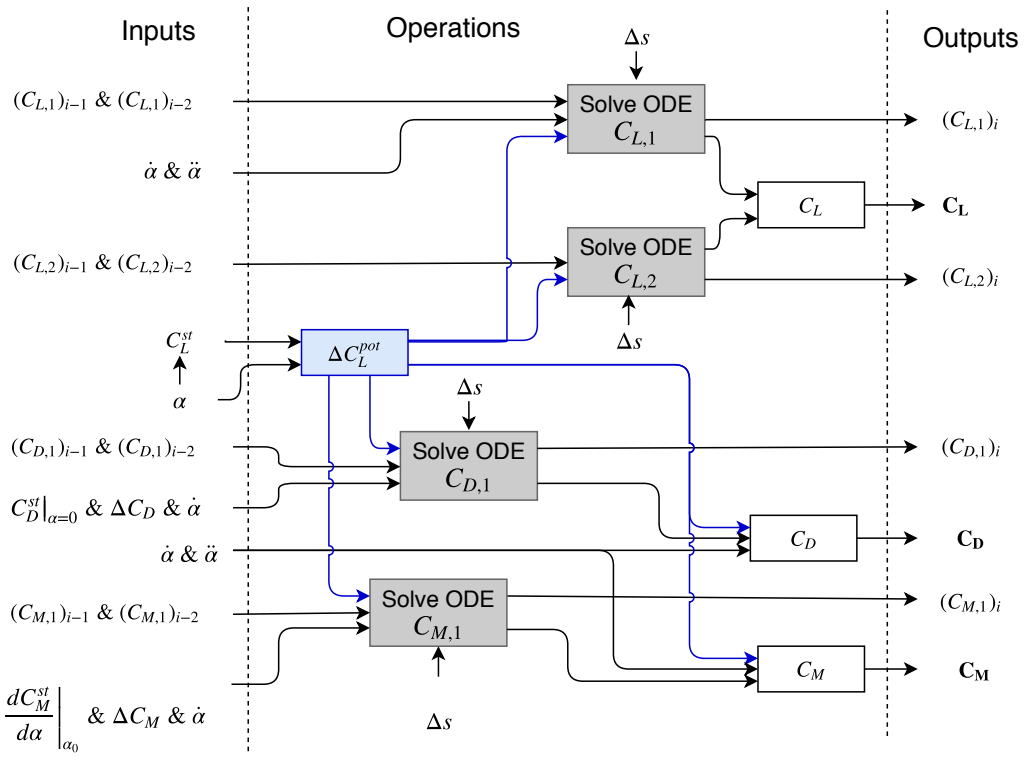

Figure B.4: Flowchart for the ONERA method

APPENDIX C

Discretization

To solve the Ordinary Differential Equations, ODE's, used by all the dynamic stall models it is assumed that the non-state-variable terms are piecewise constant. This allows the ODE's to be integrated exactly from $i-1$ to i and so solve for the state-variable at time step i.
For the first order ODE's as in Equation C.1 the solution can be found in Equation C.2.

$$\dot{x} + Bx = C \tag{C.1}$$

$$x_i = \frac{C}{B} + \left(x_{i-1} - \frac{C}{B}\right) e^{-B\Delta t} \tag{C.2}$$

This result is identical to the indicial method as described in the Risø paper [7] when the midpoint rule for the coefficients is applied correctly to all individual inputs to the coefficients B and C.
For the second order ODE (Equation C.3) the solution can be found using the system of equations in Equations C.4 to C.6.

$$\ddot{x} + A\dot{x} + Bx = C \tag{C.3}$$

$$D_1 = 2e^{-A\Delta t/2} \cos\left(-\frac{\Delta t}{2}\sqrt{4B - A^2}\right) \tag{C.4}$$

$$D_2 = e^{-A\Delta t} \tag{C.5}$$

$$x_i = \frac{C}{B}(1 - D_1 + D_2) + D_1 x_{i-1} - D_2 x_{i-2} \tag{C.6}$$

Here the assumption is made that Δt is the same from $i-2$ to $i-1$ and from $i-1$ to i. Another issue is what happens to the imaginary number in the cosine when $4B - A^2 < 0$. In Matlab this is handled correctly, although other languages may give an error. Fortunately, this is only a potential issue for Snel's model when using the second order correction as with the coefficients for the ONERA model as in Section 2.4 $4B - A^2 > 0$ will always be satisfied.

APPENDIX D

Extreme Hysteresis Loops

In this appendix the deep stall and high reduced frequency behaviour of the models are compared using the NACA64618 airfoil. It is important to keep in mind that none of the models have been validated to far into stall or when the airfoil is upside down (so reverse flow). Despite this, the model behaviour is still relevant to know as the full range of angles of attack will be thrown at the dynamic stall models in the aeroelastic code.
First the full range of angles of attack are run through in Section D.1, followed by a selection of extreme cases in Section D.2.

D.1 Full range of angles of attack

The first model looked into over all angles of attack is Øye's model in Figure D.1. Only the positive angles of attack are looked into as the hysteresis loops for the negative angles of attack are similar. In both attached flow and fully separated flow this model follows the steady curve which is as expected.

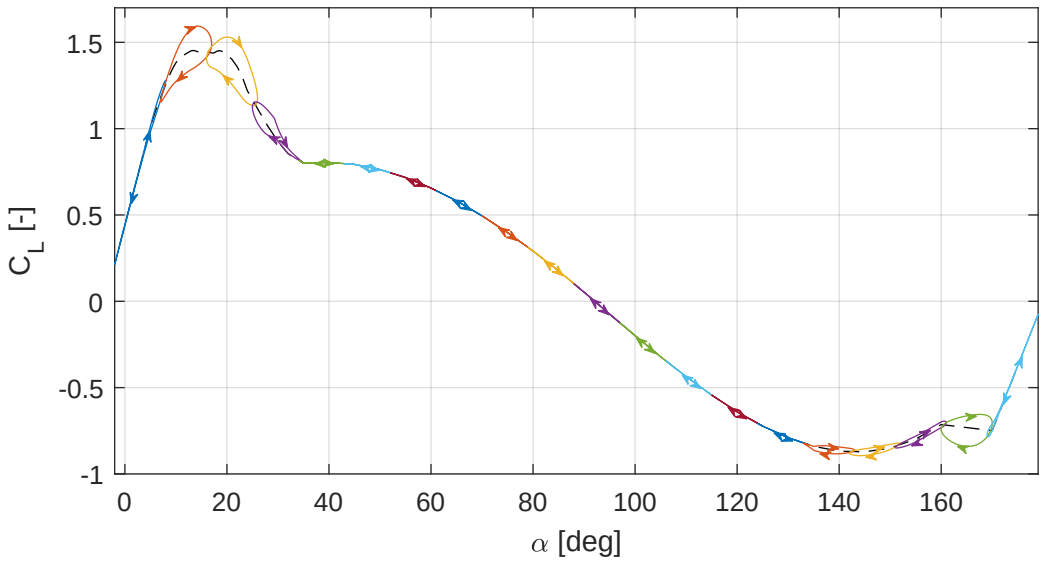

Figure D.1: C_L deep stall behaviour for Øye's model for $k = 0.05$

The Risø model does have attached flow and fully separated flow hysteresis behaviour as seen in Figures D.2, D.3 and D.4 for the lift, drag and moment respectively. For fully separated flow, the contribution from the separation point in the force and moment coefficients drops out as it becomes a constant ($f = 0$); however, the effects from the delayed angle of attack, α_E,

and the added-mass terms remain[1]. For the drag, the dynamic coefficient lags slightly behind the static curve although it never strays far. For the dynamic moment coefficient the dominant term is that from the added-mass and so the hysteresis loops remain very similar throughout the angle of attack range.

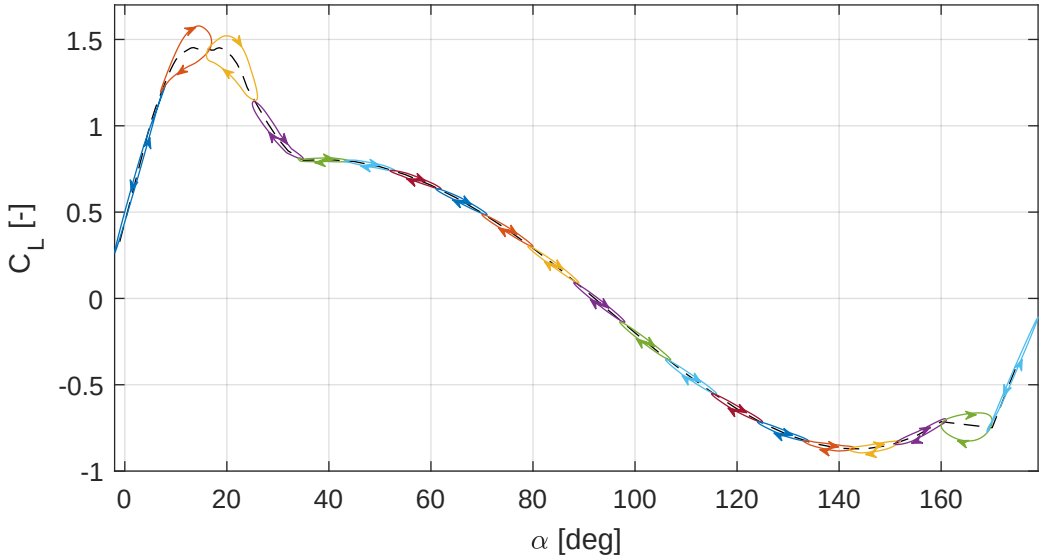

Figure D.2: C_L deep stall behaviour for the Risø model for $k = 0.05$

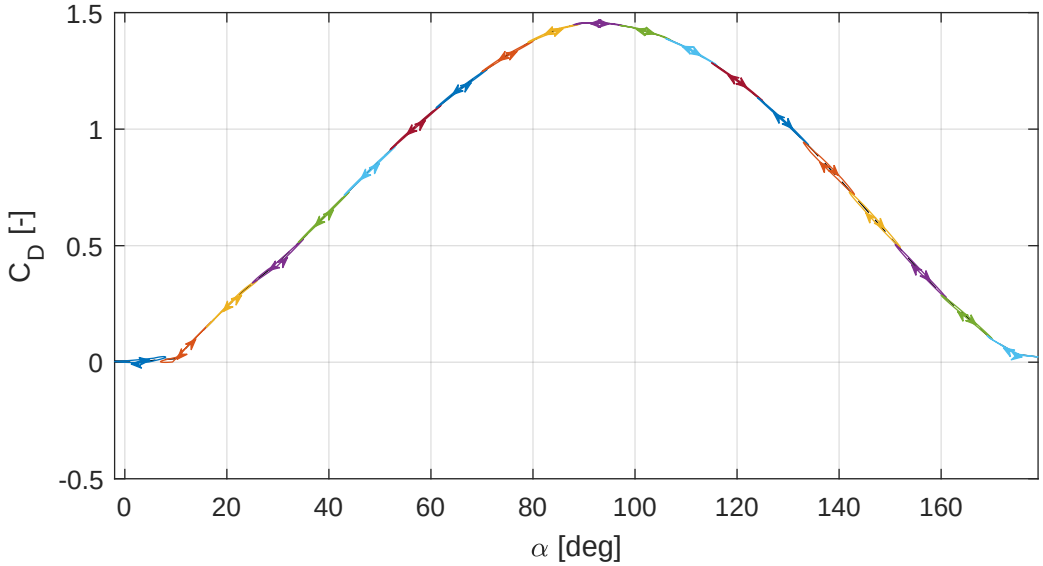

Figure D.3: C_D deep stall behaviour for the Risø model for $k = 0.05$

[1]Although the added-mass terms are phased out using $|\cos(\alpha)|$ as mentioned in Section 2.5

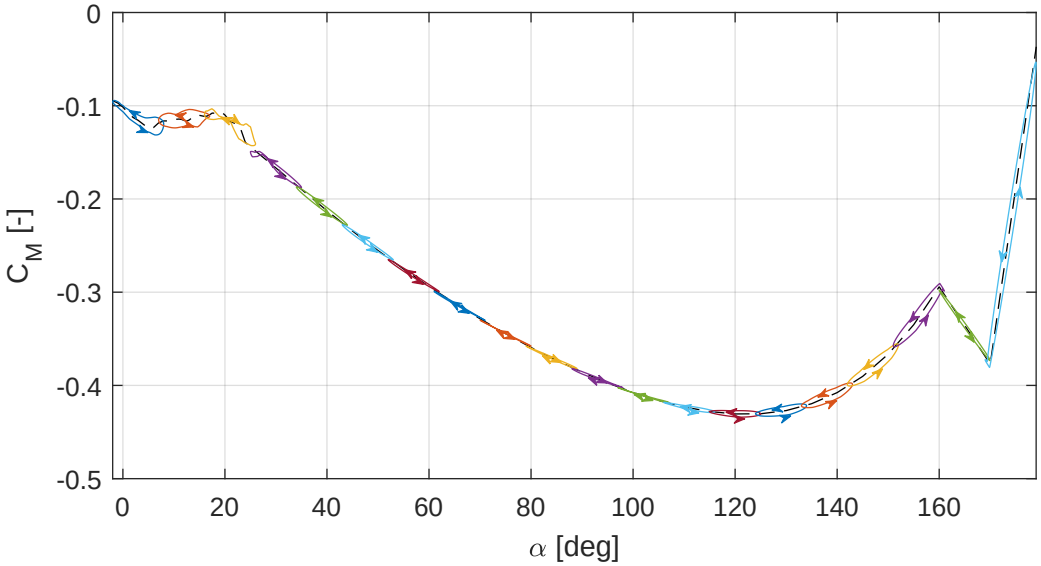

Figure D.4: C_M deep stall behaviour for the Risø model for $k = 0.05$

For Snel's model in Figure D.5 the size of the hysteresis loops decreases as the angle of attack gets closer to 90° which is due to the a combination of, first, a large ΔC_L^{pot} causing a large spring stiffness in the ODE and, secondly, the use of $\sin(\alpha)$ for C_L^{pot} causing C_L^{pot} to flatten out and so the forcing term in the ODE ($\Delta \dot{C}_L^{pot}$) is decreased.

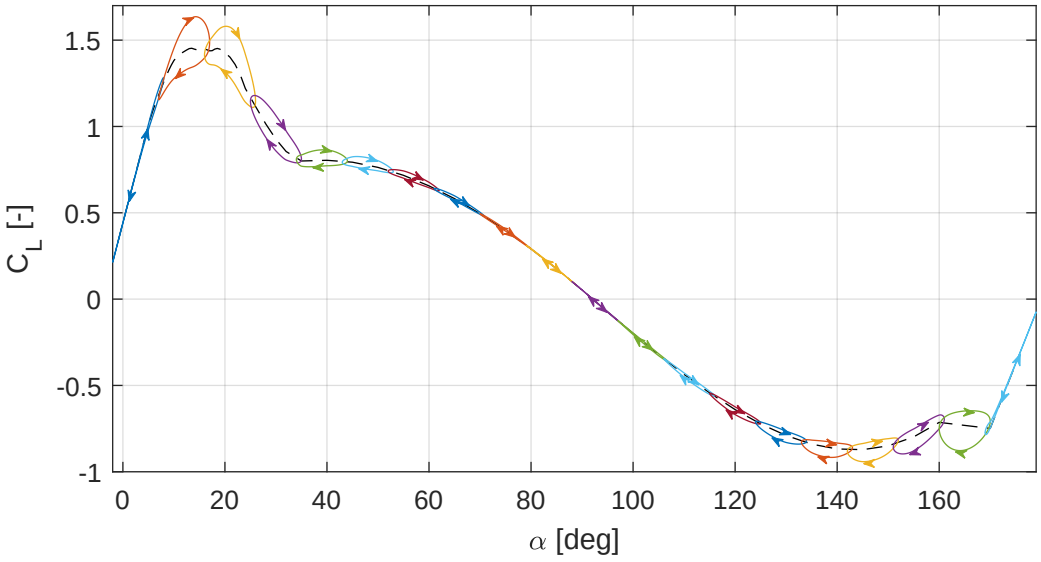

Figure D.5: C_L deep stall behaviour for Snel's model for $k = 0.05$

Finally, the deep stall curves for the ONERA model are shown in Figures D.6 to D.9. For the lift relatively large hysteresis loops are seen in deep stall (These loops are too large to be generated through only a phase delay to the steady curve, so the model must be adding some

forcing) and similarly to Snel's model the unsteady effects are suppressed near 90° as here both C_L^{pot} and ΔC_L^{pot} decrease to 0. This reduces the forcing terms for both lift components and, on top of this, the added-mass terms based on W_0' goes to zero due to $\sin(\alpha)$ flattening out. At smaller angles of attack, between roughly 20 and 40°, strange behaviour is seen with the presence of significant figure-8 shapes. Figure D.7 shows this region zoomed in with smaller amplitude α oscillations.

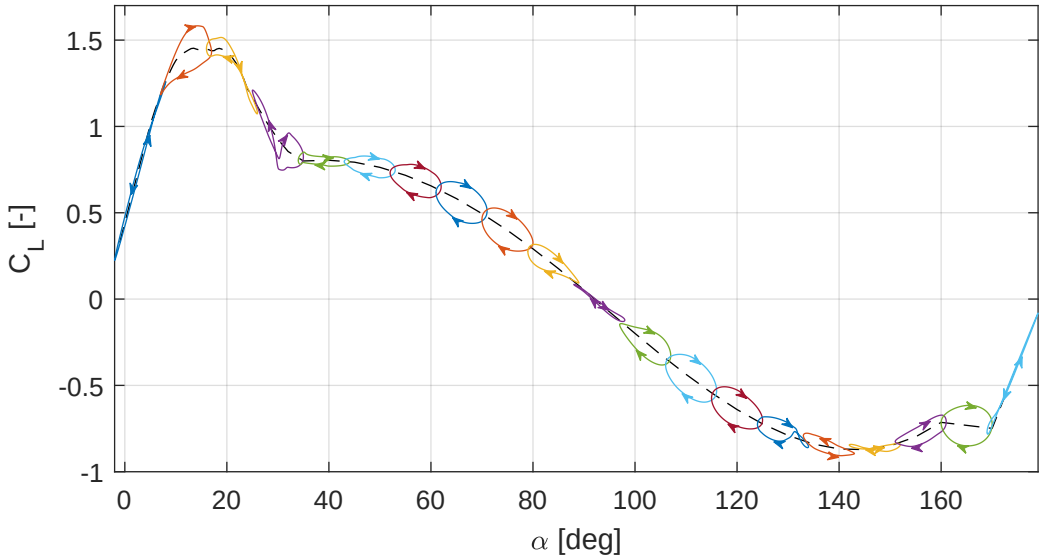

Figure D.6: C_L deep stall behaviour for the ONERA model for $k = 0.05$

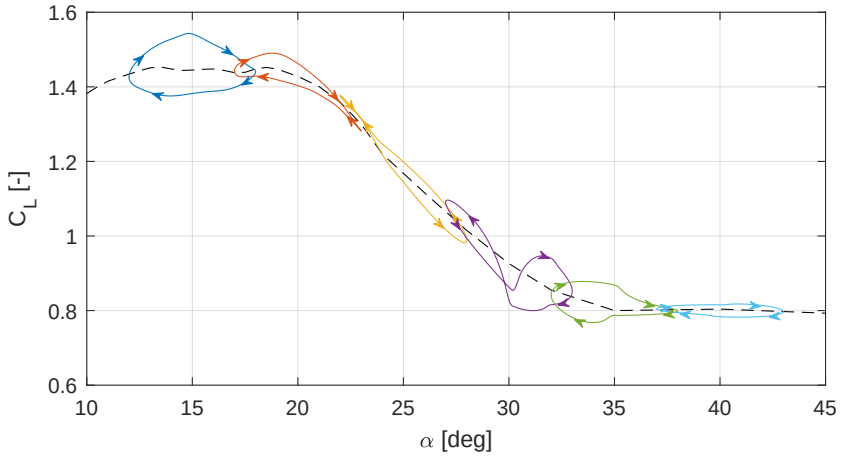

Figure D.7: Stall behaviour for the ONERA in the range 15° to 40° model for $k = 0.05$

In the region of roughly 23° to 30° the hysteresis loops rotate in the opposite direction. At roughly 30° $C_{L,pot}$ reaches the value of $4C_L$ and then $C_{L,pot}$ starts to decrease again due to the modification to the model where $C_{L,pot}$ is limited to a maximum of $4C_L$. This changes the forcing as $C_{L,pot}$ and $dC_{L,pot}$ go from increasing to decreasing which results in the loop

swapping direction. Another change in forcing is seen at around 35° as here the C_L flattens out and as $C_{L,pot} = 4C_L$ here so do $C_{L,pot}$ and $dC_{L,pot}$ which results in the ODE giving a simple decay to the steady state with the exception of the contribution from the added mass terms.

The deep stall characteristics of the drag in Figure D.8 are interesting as they show thicker and thinner hysteresis loops along the angle of attack range. This is partly due to the modification of the potential lift curve. Around $\alpha = 90°$ it is expected that the thickness of the hysteresis loops decrease due to similar reasons as for the lift coefficient. Interestingly, when fully stalled, the hysteresis loops for the Risø and ONERA models rotate in opposing directions. For the range of roughly 30° to 80° the Risø model predicts counter-clockwise loops, while the ONERA model predict clockwise rotation. For the range 100° to 150° the direction for both models is flipped, so they both still rotate in opposing directions. This is surprising and likely means that one of the models gives unphysical behaviour for the drag. As the ONERA model is more empirical than the Risø model and the author, Petot, indicates that the drag model has not been verified properly [23] in general, it is likely the Risø model that gives the better results. It should be noted, however, that the Risø model has not been verified for use this far into stall either.

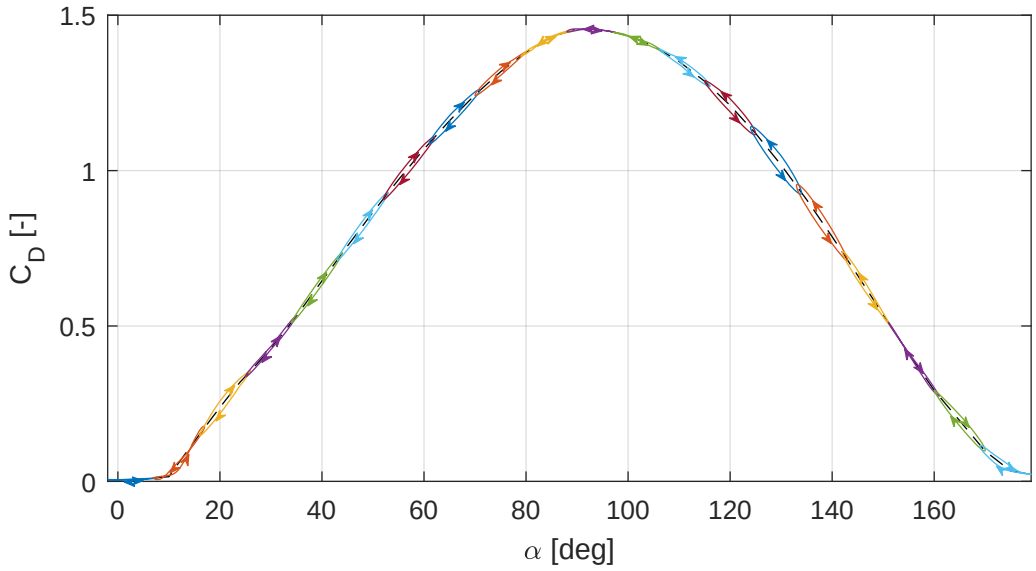

Figure D.8: C_D deep stall behaviour for the ONERA model for $k = 0.05$

For the moment the hysteresis loops are similar to those from the Riso model with the same direction although are slightly thicker.

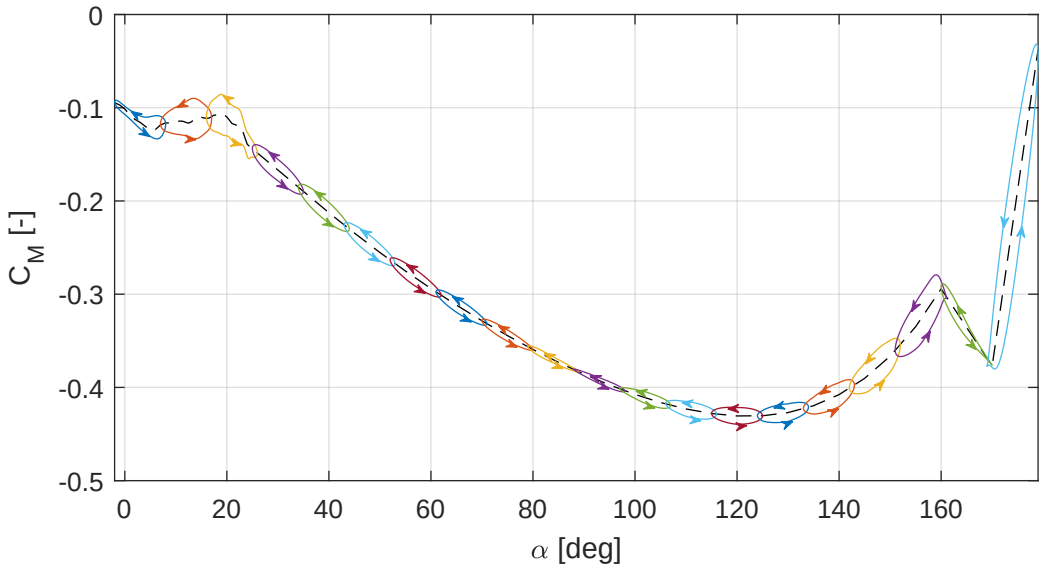

Figure D.9: C_M deep stall behaviour for the ONERA model for $k = 0.05$

D.2 Specific extreme cases

In this section some examples of interesting model behaviour are shown, starting with how both the Øye and Risø models handle the transition when C_L^{att} reaches $C_L^{att} = 4C_L^{st}$ (normally between 30° and 40°). Here the static separation point reaches the leading edge and so for higher angles of attack both models simply show an exponential decay of this f^{st} to zero. This is equivalent to an exponential decay of the dynamic lift coefficient to the static lift coefficien. This can be seen very clearly for Øye's model around 33° in Figure D.10. For the Risø model this also occurs, however, is much less visible partly due to the presence of the circulatory and added-mass terms. The different shapes of C_L^{sep} additionally contribute to the differences. The Risø model C_L^{sep} has a more gradual decrease in f^{st} to zero before $C_L^{att} = 4C_L^{st}$ than the Hermite interpolation used in Øye's model.

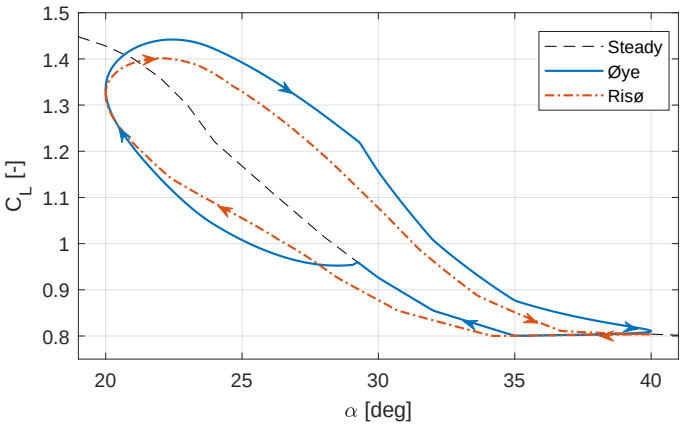

Figure D.10: Øye and Risø model behaviours at $\alpha_m = 33°$, $\alpha_a = 10°$ and $k = 0.05$

Next the scaling behaviour of Snel's model in deep stall for k's above the design range of the models is shown in Figure D.11 in comparison to the Risø model.

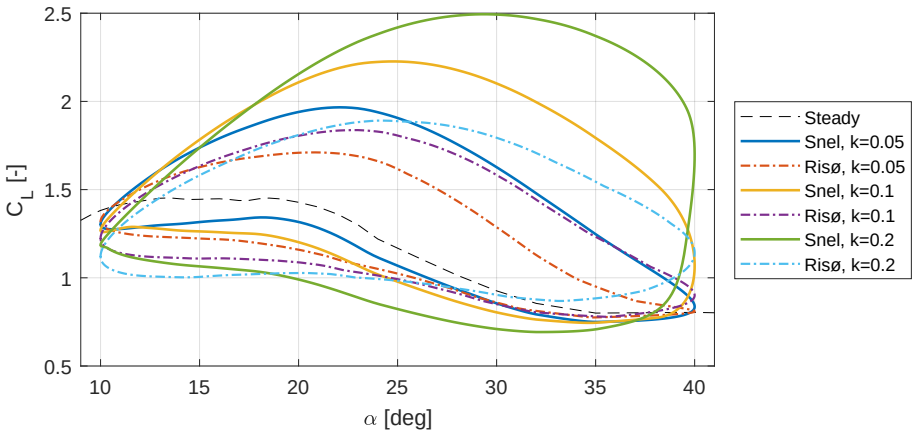

Figure D.11: Snel and Risø model behaviours at different k's at $\alpha_m = 25°$, $\alpha_a = 15°$

Here it is seen that the hysteresis loops of Snel's model can reach huge C_L's when used outside of the bounds it was tuned in. Furthermore, it has a stronger relative scaling with k than the Risø model. This due to the large dependence of the ODE in Snel's model on time derivatives. The magnitude of the forcing term (ΔC_L^{pot}) increases linearly with k and the spring stiffness on the outgoing loop decreases with $\dot{\alpha}$. The decrease of the spring stiffness is capped so that it can not become too low as mentioned in Section 2.5, however ΔC_L^{pot} is left unchecked. In particular the loop at $k = 0.2$ is unusual for Snel's model as it shows a sharp drop in lift at the highest angle of attack which is similar to leading edge stall, however the lift peak is well before this drop in lift which is not typical of leading edge stall.

APPENDIX E

ONERA $\ddot{\alpha}$ Comparison

In this appendix the effect of neglecting the acceleration term of the angle of attack in the ONERA model is shown. This is done for a single test case at $k = 0.04$ using the NACA0015 airfoil and the angle of attack input in Figure E.1. Both a pure sine wave input and a sine wave with added noise are used.

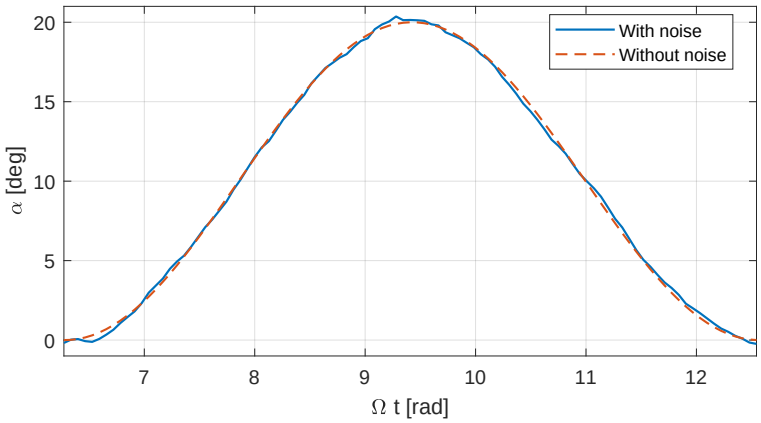

Figure E.1: Noisy and smooth angle of attack inputs comparison

In Figure E.2 the results for three cases are shown: the results from the smooth angle of attack input where $\ddot{\alpha}$ is not used and then both cases with and without $\ddot{\alpha}$ for the noisy input.

It is seen that the hysteresis loop with noise changes with respect to the smooth α input, which is both expected and physical due to the angles of attack and time history being different. Comparing the two cases with the added noise in the input shows that the contribution from $\ddot{\alpha}$ is minimal everywhere and is only really noticeable when zooming in on the edges of the plot where $\ddot{\alpha}$ is largest. This is done in Figure E.2b for the largest angles of attack.

Here it is seen that the $\ddot{\alpha}$ term mainly increases the noise in the lift coefficient which is due to the method of calculating $\ddot{\alpha}$ using backward Euler on $\dot{\alpha}$. Each time backwards Euler is used the noise in the input α is amplified resulting in increased noise in the output. For the moment coefficient this effect even worse as the added-mass terms are dominant. There is no $\ddot{\alpha}$ term in the calculation of the drag coefficient.

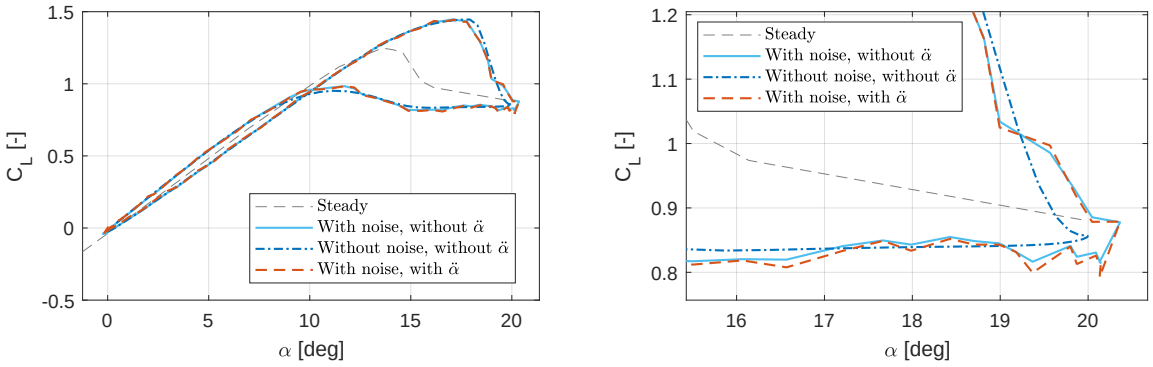

(a) C_L vs α (b) Zoomed C_L vs α

Figure E.2: Model responses for the given angle of attack input function where $k = 0.04$, $\alpha_0 = 10°$ and $\alpha_1 = 10°$

APPENDIX F

Snel Comparison

In this appendix the full Snel's model using both the first and second order correction terms is compared to the first order correction only. This is done using two of the deep stall experimental cases from the OSU measurements: One with a low reduced frequency (Figure F.1) and one with a medium reduced frequency (Figure F.2). The medium frequency case is one of the plots in Snel's paper illustrating the model [5]. The ramp function from from Section 4.6 is additionally used in Figure F.3. The experimental set up and the methodology for the plots is explained in Chapter 3. The dynamic data for the low k case in Figure F.1 does seem to be a little shifted up with respect to the steady curve as already mentioned in Chapter 4.

From both hysteresis loops it is seen that Snel's model with the first order term gives better agreement in general, in particular on the return loop. The second order model does capture the peak and so the maximum lift coefficient better. The higher frequency oscillations introduced by the second order correction term are not seen in the data and so are seen to be non-physical as also done by Holierhoek et al. [12]. Furthermore, the low reduced frequency case in particular shows the full Snel model decreasing well below the steady curve at the highest angles of attack. This is due to the second order term introducing a steady state error into the model which increases with increasing α.

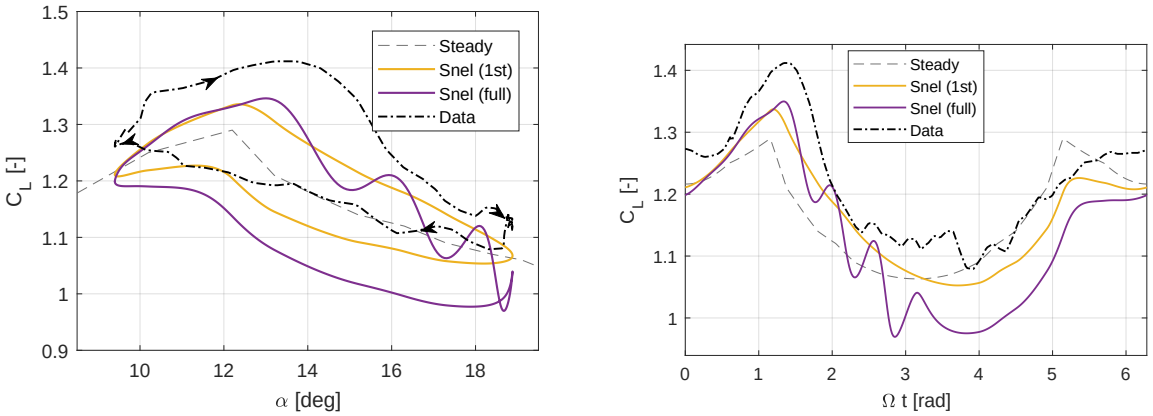

(a) C_L vs α (b) C_L vs Phase

Figure F.1: Snel model responses for the given angle of attack input function where $k = 0.019$, $\alpha_0 = 14°$ and $\alpha_1 = 5°$

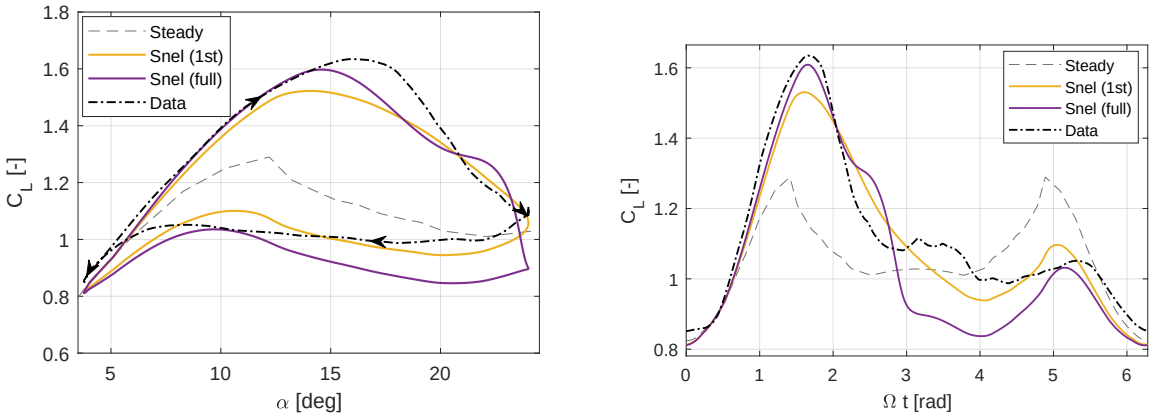

(a) C_L vs α (b) C_L vs Phase

Figure F.2: Snel model responses for the NACA4415 airfoil where $k = 0.039$, $\alpha_0 = 14°$ and $\alpha_1 = 10°$

The ramp case does show clear periodic vortex shedding for the NACA0015 airfoil. Therefore, the dynamic stall model could potentially be improved by attempting to model this periodic vortex shedding after the leading edge vortex has separated. Unfortunately, the oscillations introduced by the second order correction term of Snel's model are at a different frequency and magnitude. These ramp cases also clearly show the steady state error introduced by the second order correction term when comparing the Steady curve to the full Snel model after $s = 60$.

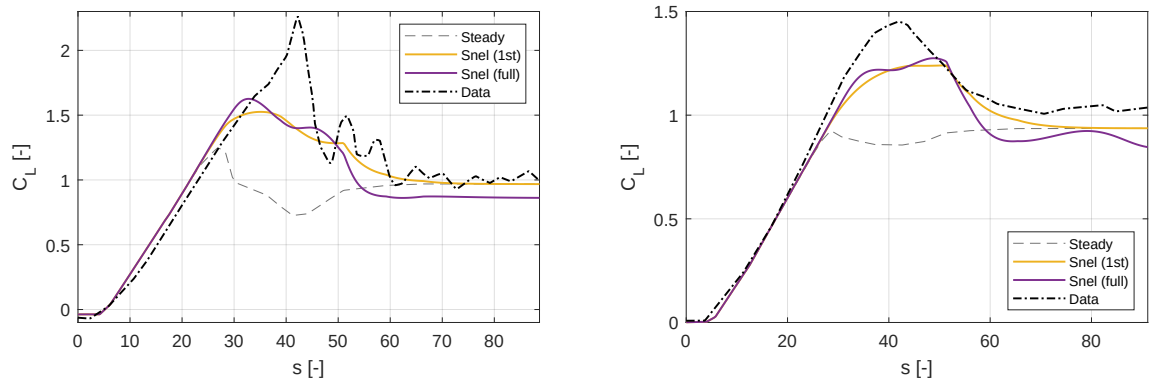

(a) NACA0015 (b) NACA0030

Figure F.3: Lift coefficient against non-dimensional time for the ramp functions for the Snel model variants

APPENDIX G

Importance of $\dot{\alpha}$

In this appendix the importance and implementation of the $\dot{\alpha}$ term is looked into for the models that use it, namely the Risø, Snel and ONERA models. Furthermore, the method used to estimate it explained.
$\dot{\alpha}$ is used in the added-mass terms in the Risø and ONERA models as so has a direct contribution to the lift and moment coefficients. When the turbulence level is high and α changes rapidly, the use of the raw $\dot{\alpha}$ signal results in unphysically large force coefficients. Furthermore, these added-mass terms are taken from Theodorsen's theory which based on sinusoidal pitching and heaving motions, so these turbulent fluctuations should arguably not have any affect on these added-mass terms. Therefore, this $\dot{\alpha}$ is estimated as only the physical pitching velocity of the airfoil section. The downside of this is that all contributions from changes in the wind direction and from the heaving motions are neglected.

The aeroelastic cases looked into in this report will be some of the cases where this assumption will cause the largest deviations from the true $\dot{\alpha}$. In DLC 1.4 the wind field undergoes large changes where the wind direction changes over 150°. In the standstill cases the turbulence will have a larger relative effect due to the (mostly) stable velocity component from the rotation of the blades being missing. This results in large k's with large α variations.

The effect on the models of having a wrong estimation of $\dot{\alpha}$ is estimated in Section G.1 for the ONERA model, Section G.2 for the Risø model and finally for Snel's model in Section G.3.

G.1 ONERA

In the ONERA model $\dot{\alpha}$ is used in two of the downwash terms: W_1 and W_0'. W_1 is defined as the difference in angle of attack between $\alpha_{1/4}$ and $\alpha_{3/4}$ which, for a constant wind field, will be equal to the non-dimensional pitching velocity if using a small angle approximation. Therefore, using the pitching velocity only results in the difference in wind direction between quarter and three-quarters chord to be neglected. For W_0', on the other hand, the use of the pitching velocity is a more significant assumption as this term is defined as $W_0' = \frac{d\sin(\alpha)}{ds} = \frac{d\alpha}{ds}|\cos(\alpha)|$[1] and so the full α should technically be used. Unfortunately this is not possible for the ONERA model due to this model's large dependence on W_0' for both the attached flow and dynamic stall behaviour. If the $\dot{\alpha}$ is obtained from the raw α input, then this will cause the ONERA model to show unphysical behaviour so bad that the aeroelastic code will terminate for the standstill cases.

Figure G.1 shows an example lift hysteresis loop for a pure pitching motion without turbulence compared to the loops when either W_1 or W_0' are set to zero.

[1] Here the absolute value of $\cos(\alpha)$ is taken to account for the leading and trailing edge swapping at 90°.

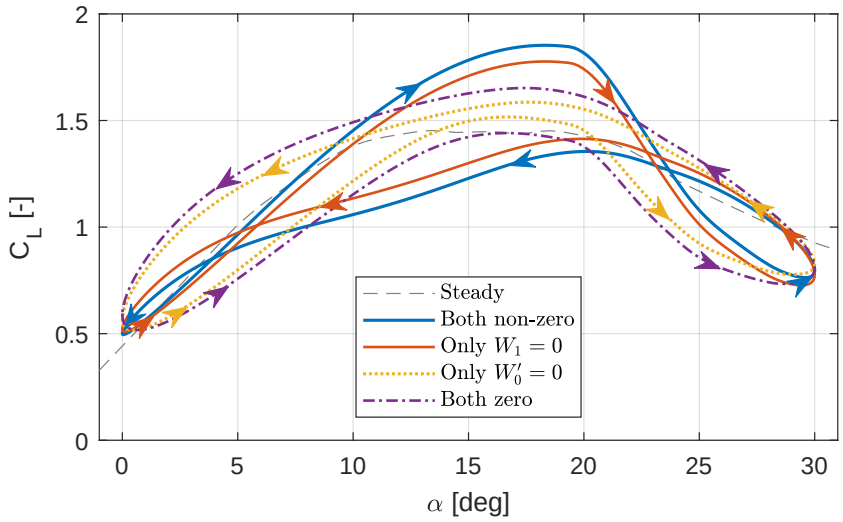

Figure G.1: Comparison of hysterisis loops for the ONERA model with different terms set to zero for the NACA64618 airfoil with $k = 0.05$, $\alpha_m = 15°$ and $\alpha_m = 15°$

This shows that for the correct dynamic stall behaviour the ONERA model leans very heavily on both W_1 and W_0', with W_0' being the most important of the two. When W_0' is set to zero in this example, then the entire hysteresis loop goes in the counter-clockwise direction which is unphysical. This, together with W_0' being the term most affected by the current approximation of $\dot{\alpha}$, explains why the ONERA model shows exceptionally poor behaviour throughout Chapter 5.

For the original curve, so that indicated as 'Both non-zero', a small counter-clockwise part is seen at the highest α's which is also unphysical. This is a general flaw in the ONERA model and can be seen in more detail in Section D.1.

G.2 Risø

The Risø model is also affected by the $\dot{\alpha}$ term, however this is only important for the attached flow and not for the stall properties. If $\dot{\alpha} = 0$ then the attached flow hysteresis loops are exaggerated as for example in Figure G.2. This is due to both the lack of added-mass terms and the distinction between $\alpha_{1/4}$ and $\alpha_{3/4}$.
This distinction between $\alpha_{1/4}$ and $\alpha_{3/4}$ is important as where $\alpha_{3/4}$ is used as the base for the time delayed α_E. Therefore $\dot{\alpha}$ will also have an effect on the circulatory terms.

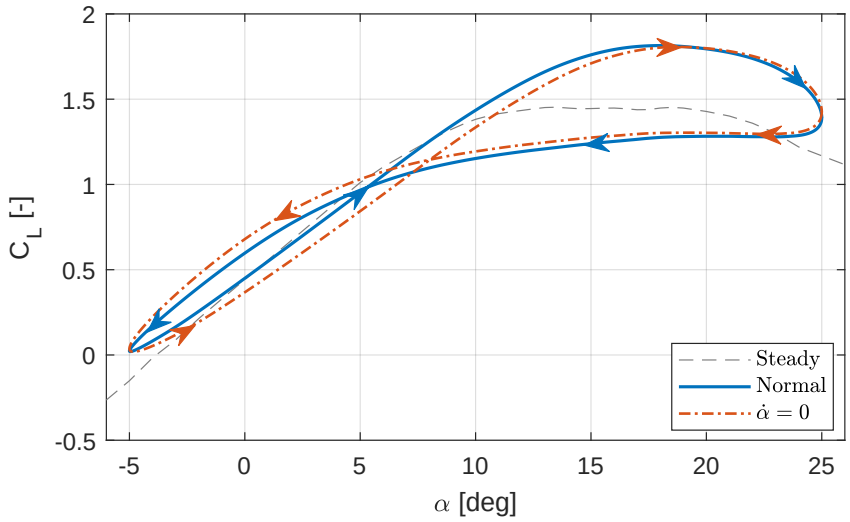

Figure G.2: Comparison of hysterisis loops for the Risø model with $\dot{\alpha}$ set to zero for the NACA64618 airfoil with $k = 0.05$, $\alpha_m = 10°$ and $\alpha_m = 15°$

To visualize the performance of the Risø model in the aeroelastic code Figure G.3 is made for the standstill Case 5. This contains the assumption that the changes in wind direction do not affect $\dot{\alpha}$.

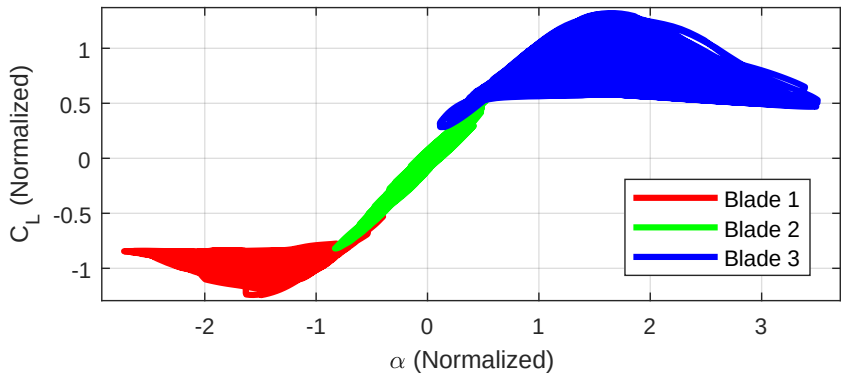

Figure G.3: C_L time traces with the Risø model in Case 5 at the highest Damping factor

The attached flow behaviour is seen to be significant indicating that the behaviour is more like that of the $\dot{\alpha} = 0$ behaviour; however, as it is unknown what the effective k's are, no conclusion can be drawn.

G.3 Snel

Snel's model does not contain any added mass terms or attached flow behaviour so $\dot{\alpha}$ does not directly contribute to the lift coefficient, although it is an important contributor to the spring stiffness of the ODE. Therefore, it still has a significant effect on the dynamic stall loops as shown in Figure G.4.

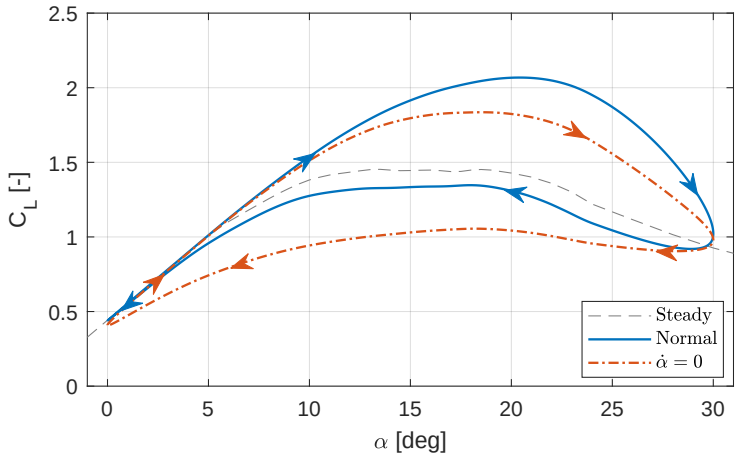

Figure G.4: Comparison of hysterisis loops for Snel's model with $\dot{\alpha}$ set to zero for the NACA64618 airfoil with $k = 0.05$, $\alpha_m = 15°$ and $\alpha_m = 15°$

The whole dynamic stall loop is shifted up which is due to Snel's model in effect having a variable time constant. $\dot{\alpha}$ increases the time lag when going into stall and decreases it on the return part.
As $\dot{\alpha}$ is only in the spring stiffness Snel's model is much more robust in handling quick variations in $\dot{\alpha}$, therefore $\dot{\alpha}$ is obtained from the raw α signal. This is opposed to the ONERA and Risø models, which use an approximation of the pitching velocity only. Snel's model is tuned to pitching motions only so there is a case for using the pitching velocity instead of $\dot{\alpha}$, although that would still neglect the changes in the wind direction.
For Case 5 of the standstill cases, this gives the response in Figure G.5 where no extremely abnormal behaviour is seen. There are still a couple of occurrences for Blade 3 where the normalized C_L is still above 1 at $\alpha > 3$. This means that the dynamic C_L exceeds the static stall value at an α over 3 times the static stall peak angle of attack.

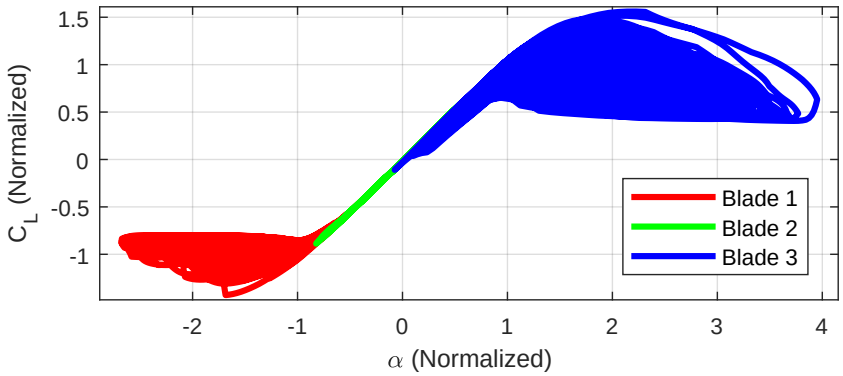

Figure G.5: C_L time traces with Snel's model in Case 5 at the highest Damping factor

Nomenclature

List of Abbreviations

BEM	Blade Element Momentum
DF	Damping Factor
DLC	Design Load Case
HAWT	Horizontal Axis Wind Turbine
IEC	International Electrical Commission
ODE	Ordinary Differential Equation
ONERA	Office National d'Etudes et de Recherches Aérospatiales
OSU	Ohio State University
TI	Turbulence intensity

List of Symbols

α	Angle of attack	$[rad]$
α_0	Zero lift angle of attack	$[rad]$
α_a	Amplitude of the sinusoidal α oscillations	$[rad]$
α_E	Effective angle of attack	$[rad]$
α_m	Mean value of the sinusoidal α oscillations	$[rad]$
$\alpha_{3/4}$	Angle of attack at 3/4 chord	$[rad]$
α_{max}^{sep}	Angle of attack of the peak in the separated lift curve	$[rad]$
α_{sep}	Angle of attack where the flow becomes fully separated in the static case	$[rad]$
α_{shear}	Wind shear exponent	[-]
$\bar{\alpha}$	Amplitude of sinusoidal pitching motion	$[rad]$
$\bar{\bar{h}}$	Amplitude of sinusoidal plunging motion	[-]
$\Delta\tau$	Time delay for stall	[-]
ΔC_L^{pot}	Difference between potential flow lift and the steady lift	[-]
$\Delta C_{L,i}$	Lift coefficient correction for Snel's model	[-]
Δt	Time step	$[s]$
λ	Constant in the ONERA model	[-]
Ω	Rotational speed of the turbine	$[rad/s]$
ω	rotational frequency	[-]

ρ	Air density	$[kg/m^3]$
σ_i	Constant in the ONERA model	[-]
τ	Non-dimensional time constant in the Øye model	[−]
τ_f	Non-dimensional time constant in the Risø model	[−]
τ_p	Non-dimensional time constant in the Risø model	[−]
θ	Angle of attack due to pitch only	[-]
$\tilde{h}$	Plunge normalized by the half chord	[-]
ζ_p	Pitch-damping parameter	[-]
a	Center of rotation with respect to the mid-chord	[-]
a^{st}	Arm between the quarter chord and the equivalent center of pressure	[-]
A_i	Coefficient of time lag for the circulatory terms	[-]
a_i	Constant in the ONERA model	[-]
a_{α_0}	Factor for the derivative of the fully separated lift curve at the zero lift point	[−]
$a_{\alpha_{sep}}$	Factor for the derivative of the fully separated lift curve at the point of fully separated flow	[−]
B	Number of blades	[-]
b_i	Coefficient of time lag for the circulatory terms	[-]
c	Chord	$[m]$
$C(k)$	Theodorsen's function	[-]
$C_{D,0}^{st}$	Steady zero-lift drag coefficient	[-]
$C_{D,1}$	Drag coefficient component in the ONERA model	[-]
C_D	2D dynamic drag coefficient	[-]
C_D^{st}	Steady drag coefficient	[-]
c_i	ODE coefficient in Snel's model	[-]
$C_{L,i}$	Lift coefficient component in the ONERA model	[-]
C_L	2D dynamic lift coefficient	[-]
$C_L^{att,lag}$	Attached flow lift coefficient after time lag	[-]
C_L^{att}	Steady fully attached flow lift coefficient	[-]
C_L^{pot}	Steady potential flow lift coefficient	[-]
C_L^{sep}	Steady fully separated flow lift coefficient	[-]
C_L^{st}	Steady lift coefficient	[-]
$C_{M,0}^{st}$	Steady zero-lift moment coefficient	[-]
$C_{M,1}$	Moment coefficient component in the ONERA model	[-]
C_M	2D dynamic moment coefficient about the quarter chord	[-]
C_M^{lin}	Linear moment coefficient for the ONERA model	[-]
C_M^{st}	Steady moment coefficient about the quarter chord	[-]

C_n	Normal (out-of-plane) force coefficient	[-]
C_P	Power coefficient	[-]
C_T	Thrust coefficient	[-]
C_t	Tangential (in-plane) force coefficient	[-]
dr	Radial length of an annuli	$[m]$
e_i	Constant in the ONERA model	[-]
f^{dyn}	Dynamic separation point	[-]
f^{lag}	Equivalent quasi-steady separation point for $C_L^{att,lag}$	[-]
f^{st}	Steady Separation point	[-]
h	Plunge	$[m]$
j	Imaginary number $\sqrt{-1}$	[-]
k	Reduced frequency	[-]
k_s	Strouhal vortex shedding frequency	[-]
M	Mach number	[-]
M_{edge}	Normalized peak-to-peak root edgewise bending moment	[-]
R	Rotor radius	$[m]$
r	Radial position along blade	$[m]$
r_i	Constant in the ONERA model	[-]
s	Non-dimensional time	[-]
s_0	Constant in the ONERA model	[-]
t	Time	$[s]$
T_f	Time constant in the Risø model	$[s]$
T_f	Time constant in the Øye model	$[s]$
T_p	Time constant in the Risø model	$[s]$
T_u	Time for the relative velocity to travel a half chord	[s]
U	Velocity	$[m/s]$
U_∞	Freestream wind velocity	$[m/s]$
U_{rel}	Inflow velocity relative to airfoil	$[m/s]$
W_0	Non-dimensional downwash at the quarter chord	[-]
W_1	Non-dimensional difference in downwash between the three-quarter chord and quarter chord	[-]
w_i^{lag}	i'th time lagged downwash component	$[m/s]$

Bibliography

[1] M. Kramer. *Increase in the maximum lift of an airfoil due to a sudden increase in its effective angle of attack resulting from a gust*. 1932.

[2] G.J. Leishman. *Principles of helicopter aerodynamics*. Cambridge university press, 2006.

[3] G.J. Leishman and T.S. Beddoes. "A Semi-Empirical Model for Dynamic Stall". In: *Journal of the American Helicopter society* 34.3 (1989), pp. 3–17.

[4] C.T. Tran and D. Petot. *Semi-empirical model for the dynamic stall of airfoils in view of the application to the calculation of responses of a helicopter blade in forward flight*. 1980.

[5] H. Snel. "Heuristic modelling of dynamic stall characteristics". In: *EWEC Conference Dublin Castle, Ireland*. Netherlands energy research foundation. 1997, pp. 429–433.

[6] S. Øye. "Dynamic stall simulated as time lag of separation". In: *Proceedings of the 4th IEA Symposium on the Aerodynamics of Wind Turbines*. Rome, Italy. 1991.

[7] M.H. Hansen, M. Gaunaa, and H.A. Madsen. "A Beddoes-Leishman type dynamic stall model in state-space and indicial formulations". In: *Risø–R–1354(EN)* (2004).

[8] J.W. Larsen, S.R.K. Nielsen, and S. Krenk. "Dynamic stall model for wind turbine airfoils". In: *Journal of Fluids and Structures* 23.7 (2007), pp. 959–982.

[9] M.O.L. Hansen, J.N. Sørensen, S. Voutsinas, N. Sørensen, and H.A. Madsen. "State of the art in wind turbine aerodynamics and aeroelasticity". In: *Progress in aerospace sciences* 42.4 (2006), pp. 285–330.

[10] G. Bir and J. Jonkman. "Aeroelastic instabilities of large offshore and onshore wind turbines". In: *Journal of Physics: Conference Series*. Vol. 75. 1. IOP Publishing. 2007, p. 012069.

[11] J.G. Schepers and H. Snel. "Model experiments in controlled conditions". In: *ECN Report: ECN-E-07-042* (2007).

[12] J.G. Holierhoek, J.B. de Vaal, A.H. van Zuijlen, and H. Bijl. "Comparing different dynamic stall models". In: *Wind Energy* 16.1 (2013), pp. 139–158.

[13] A. Bjorck, S.E. Thor, A.J. Brand, and ECN-Renewable Energy. "DYNAMIC STALL AND 3D EFFECTS". In: *Contributions from the Department of Meteorology and Wind Energy to the EWEC'94 Conference in Thessaloniki, Greece*. 1995, pp. 59–65.

[14] W.A.A.M. Bierbooms. "A comparison between unsteady aerodynamic models". In: *Journal of Wind Engineering and Industrial Aerodynamics* 39.1-3 (1992), pp. 23–33.

[15] J.G. Leishman. "Challenges in modelling the unsteady aerodynamics of wind turbines". In: *Wind energy* 5.2-3 (2002), pp. 85–132.

[16] T.S.R. Reddy and K.R.V. Kaza. "A comparative study of some dynamic stall models". In: *NASA Technical Memorandum 88917* (1987).

[17] W.J. McCroskey. *The phenomenon of dynamic stall*. Tech. rep. National Aeronautics and Space Administration Moffett Field CA. AMES Research Center, 1981.

[18] J. Jonkman, S. Butterfield, W. Musial, and G. Scott. *Definition of a 5-MW reference wind turbine for offshore system development*. Tech. rep. National Renewable Energy Laboratory (NREL), Golden, CO., 2009.

[19] T.J. Larsen and A.M. Hansen. *How 2 HAWC2, the user's manual (ver 4-6)*. Tech. rep. Risø National Laboratory, 2015.

[20] L. Bergami, M. Gaunaa, and J. Heinz. "Indicial lift response function: an empirical relation for finite-thickness airfoils, and effects on aeroelastic simulations". In: *Wind Energy* 16.5 (2013), pp. 681–693.

[21] J.P. Jones. "The influence of the wake on the flutter and vibration of rotor blades". In: *The Aeronautical Quarterly* 9.3 (1958), pp. 258–286.

[22] M.J. Hoffman, R.R. Ramsay, and G.M. Gregorek. "Unsteady aerodynamic performance of wind turbine airfoils". In: *Proceedings of AWEA Wind Power Conference 94, Minneapolis* (1994).

[23] D. Petot. "Differential equation modeling of dynamic stall". In: *La Recherche Aerospatiale (English Edition)* 5 (1989), pp. 59–72.

[24] D.A. Peters. "Toward a unified lift model for use in rotor blade stability analyses". In: *Journal of the American Helicopter Society* 30.3 (1985), pp. 32–42.

[25] J.M. Greenberg. "Airfoil in sinusoidal motion in a pulsating stream". In: *Technical note 1326* (1947).

[26] K.W. McAlister, O. Lambert, and D. Petot. *Application of the ONERA model of dynamic stall*. Tech. rep. National Aeronautics and Space Administration Moffett Field CA AMES Research Center, 1984.

[27] W.J. McCroskey, K.W. McAlister, L.W. Carr, S.L. Pucci, O. Lambert, and R.F. Indergrand. "Dynamic stall on advanced airfoil sections". In: *Journal of the American Helicopter Society* 26.3 (1981), pp. 40–50.

[28] J.C. Tyler and J.G. Leishman. "Analysis of pitch and plunge effects on unsteady airfoil behavior". In: *Journal of the American Helicopter Society* 37.3 (1992), pp. 69–82.

[29] Z. Du and M. Selig. "A 3-D stall-delay model for horizontal axis wind turbine performance prediction". In: *1998 ASME Wind Energy Symposium*. 1998, p. 21.

[30] S. Schreck and M. Robinson. "Blade three-dimensional dynamic stall response to wind turbine operating condition". In: *Journal of Solar Energy Engineering* 127.4 (2005), pp. 488–495.

[31] A.O. St Hilaire and F.O. Carta. *Analysis of Unswept and Swept Wing Chordwise Pressure Data from an Oscillating NACA 0012 Airfoil Experiment. Volume I.* Tech. rep. United Technologies Research Center East Hartford CT., 1983.

[32] T. Theodorsen. "General theory of aerodynamic instability and the mechanism of flutter". In: *NACA report 496* (1935).

[33] R.K. Angell, Musgrove P.J., and R.A.M. Galbraith. "The collected data for tests on a NACA0015 aerofoil". In: *Glasgow University Report 8803* (1988).

[34] H. Wagner. "Über die Entstehung des dynamischen Auftriebes von Tragflügeln". In: *ZAMM-Journal of Applied Mathematics and Mechanics/Zeitschrift für Angewandte Mathematik und Mechanik* 5.1 (1925), pp. 17–35.

[35] R.K. Angell, Musgrove P.J., and R.A.M. Galbraith. "Collected data for tests on a NACA0030 aerofoil". In: *Glasgow University Report 8826* (1988).

[36] M.J. Hoffmann, R. Reuss Ramsay, and G.M. Gregorek. *Effects of grit roughness and pitch oscillations on the NACA 4415 airfoil*. Tech. rep. National Renewable Energy Lab., Golden, CO (United States); Ohio State Univ., Columbus, OH (United States), 1996.

[37] T. Burton, N. Jenkins, D. Sharpe, and E. Bossanyi. *Wind energy handbook*. John Wiley & Sons, 2011.

[38] M.O.L. Hansen. *Aerodynamics of wind turbines*. Routledge, 2015.

[39] M. Gaunaa, J. Heinz, and W. Skrzypiński. "Toward an engineering model for the aerodynamic forces acting on wind turbine blades in quasisteady standstill and blade installation situations". In: *Journal of Physics: Conference Series*. Vol. 753. 2. IOP Publishing. 2016, p. 022007.

[40] IEC. "International Electrotechnical Commission 61400-1 Ed.3". In: *Wind Turbines — Part 1: Design Requirements* (2005).

[41] T.J. Petersen et al. *Prediction of dynamic loads and induced vibrations in stall*. Tech. rep. Risø National Laboratory, 1998.

[42] F. Rasmussen et al. "Present status of aeroelasticity of wind turbines". In: *Wind energy* 6.3 (2003), pp. 213–228.

[43] K. Wang, V.A. Riziotis, and S.G. Voutsinas. "Aeroelastic Stability of Idling Wind Turbines". In: *Journal of Physics: Conference Series*. Vol. 753. 4. IOP Publishing. 2016, p. 042008.

[44] M.H. Hansen. "Aeroelastic instability problems for wind turbines". In: *Wind Energy* 10.6 (2007), pp. 551–577.

[45] W.R. Skrzypiński, M. Gaunaa, N. Sørensen, F. Zahle, and J. Heinz. "Self-induced vibrations of a DU96-W-180 airfoil in stall". In: *Wind Energy* 17.4 (2014), pp. 641–655.

[46] T. Buhl. "Edgewise vibrations in stand still". In: *Risø*. Risø National Laboratory, 2007, pp. 63–71.

[47] D.W. Lobitz. "Aeroelastic stability predictions for a MW-sized blade". In: *Wind Energy* 7.3 (2004), pp. 211–224.